

To the University of Wyoming:

The members of the Committee approve the thesis of Austin M. Carey presented on September 21<sup>st</sup>, 2016

Ginger B. Paige, Chairperson

W. Steven Holbrook, External Department Member

Scott N. Miller

Bradley J. Carr

APPROVED:

Scott N. Miller, Department Chair, Department of Ecosystem Science and Management.

Francis D. Galey, College Dean

Carey, Austin M., Partitioning Surface and Subsurface Flow in a Semi-arid Rangeland Watershed, M.S., Department of Ecosystem Science and Management, University of Wyoming, September, 2016

This thesis couples variable intensity rainfall simulation with surface geophysical measurements to study the partitioning of surface and subsurface flow processes at the ecological site scale. Ecological sites, hillslope scale soil-vegetation complexes, are the basic landscape unit for the management of rangeland ecosystems. Moreover, they provide a useful framework to study complex rangeland ecohydrologic processes. My research used observational hydrogeophysics field experiments to link ecological site characteristics to hydrologic function. I conducted over 20 experiments integrating rainfall simulation with high-resolution time-lapse electrical resistivity tomography on hillslope plots at five different ecological sites within the Upper Crow Creek Watershed in southeastern Wyoming. First order constraints on subsurface structure at these sites were made by jointly interpreting electrical resistivity tomography, seismic refraction surveys and ground penetrating radar datasets. My results show that ecological sites have a characteristic hydrologic response that can be quantified. ANOVA analysis found statistically significant differences in how ecological sites partition rainfall into runoff response. Sites ranged from infiltrating 100% of the applied rainfall to converting over 40% of the rainfall into surface runoff. Multiple linear regressions indicated that a large amount of the variability in surface hydrologic response could be explained by parsimonious models consisting only of ground cover variables. From the time-lapse resistivity datasets I was able to track the movement of the wetting front in the subsurface. ANCOVA results found significant differences in the rate of wetting front migration, which can be attributed to different ecological site characteristics. Joint interpretation of the geophysics results provided information about subsurface features that influenced hydrologic response at these sites. This research directly supports the concept of

mapping the variability in rangeland hydrology at the ecological site scale and represents the first step in the process of coupling these two observational platforms to quantify the partitioning of rainfall into surface and subsurface flow components.

**Partitioning Surface and Subsurface Flow in a Semi-arid Rangeland Watershed**

By

Austin M. Carey

A thesis submitted to the Department of Ecosystem Science and Management

and the University of Wyoming

in partial fulfillment of the requirements

for the degree of

MASTER OF SCIENCE

in

RANGELAND ECOLOGY AND WATERSHED MANAGEMENT

and

WATER RESOURCES

Laramie, Wyoming

September, 2016

COPYRIGHT PAGE

© 2016, Austin M. Carey

## ACKNOWLEDGEMENTS

First and foremost I would like to express my sincere gratitude to my major advisor Dr. Ginger Paige for her fundamental role in my master's work. Ginger has provided me with unwavering support and guidance throughout these three years. She has spent countless hours imparting her knowledge and wisdom in the field of hydrology and has helped me over a number of hurdles outside of the realm of academia. Without her this thesis would not be possible.

I would like to thank Dr. Bradley Carr for his guidance and patience as I learned about the field of Geophysics. Brad has helped me develop an invaluable skill set that I plan to take advantage of as I move forward with my career. Special thanks are also due to Dr. Scott Miller and Dr. Steve Holbrook for their help and guidance as committee members.

I have been lucky enough to established lasting relationships with my fellow graduate students, from which I have grown both academically and emotionally. These relationships have made my stay in Laramie a pleasant one.

I would like to thank my lovely wife Alex. She is my best friend and partner in all aspects of life. I truly am "the luckiest."

My father has instilled in me the work ethic and the sense of pride necessary to complete this degree, and for that I thank him.

Lastly, this thesis is dedicated to the memory of my mother, Deborah Carey. "Mother of three, soul mate to one."

Funding for this research came from the Wyoming Center for Environmental Hydrology and Geophysics (NSF EPS-1208909).

## TABLE OF CONTENTS

<b>List of Tables .....</b>	<b>ix</b>
<b>List of Figures.....</b>	<b>x</b>
<b>Chapter 1: General Thesis Overview.....</b>	<b>1</b>
Study Area .....	3
Thesis Description .....	5
References.....	7
<b>Chapter 2: Ecological Site-scale Hydrologic Response in a Semi-arid Rangeland Watershed .....</b>	<b>9</b>
Abstract.....	9
Introduction.....	10
Methods.....	12
Results.....	22
Discussion.....	33
Conclusion .....	38
Management Implications.....	38
Acknowledgements.....	39
References.....	40
<b>Chapter 3: Forward Modeling to Investigate Inversion Artifacts Resulting from Time-Lapse Electrical Resistivity Tomography during Rainfall Events .....</b>	<b>45</b>
Abstract.....	45
Introduction.....	46
Materials and Methods.....	49
Results and Discussion .....	56
Conclusion .....	69
Acknowledgements.....	70
References.....	71

<b>Chapter 4: Characterizing Hydrological Processes at the Ecological Site Scale: Coupling Rainfall Simulation with Surface Geophysical Measurements .....</b>	<b>76</b>
Abstract .....	76
Introduction .....	77
Study Area .....	79
Methodology .....	83
Results .....	96
Discussion .....	108
Conclusion .....	113
Acknowledgements .....	114
References .....	115
<b>Chapter 5: Conclusions and Recommendations for Future Work .....</b>	<b>120</b>
Primary Findings and Significance .....	120
Limitations of this Research .....	124
Recommendations for Future Work .....	125
References .....	129
<b>Appendix A .....</b>	<b>132</b>
<b>Appendix B .....</b>	<b>135</b>

## LIST OF TABLES

Table 2.1: Site descriptions for the five sites .....	17
Table 2.2: Peak runoff rates ( $Q_{\text{peak}}$ ) and runoff ratios (C) for 16 of the 20 wet simulator runs. The LU site is not shown because there was no runoff for any simulation experiment at this site. Averages, standard errors (SE) and coefficient of variations (CV) are computed for each site....	25
Table 2.3: Maximum spatially averaged infiltration rate ( $\mu_f$ ) values for the five ecological sites. Normal averages and coefficients of variations (CV) are computed using all four plots. Adjusted averages and CVs are computed after removing anomalous plots. ....	27
Table 2.4: Ground and canopy cover characteristics for the 20 runoff plots.....	31
Table 2.5: Forward regression equations for the wet simulator runs using vegetation transect data as the explanatory variables and the five steady state infiltration rates (SS1-SS5), runoff coefficient (C) and peak runoff rate ( $Q_{\text{peak}}$ ), as the dependant variables. All equations are significant at the $p \leq 0.05$ level. Explanatory variables are shown with beta weights and significance codes .....	32
Table 3.1: Resistivity values for the four forward modeling scenarios. ....	55
Table 3.2: Average, median and maximum artifact values presented as percent changes in resistivity ( $\Delta\rho$ ). Any region of the time-lapse profile with a percent change greater than zero was considered to be an artifact. A coefficient of variation (CV) for the artifacts was calculated.....	65
Table 4.1: Site descriptions for the five study sites. Adapted from Carey and Paige (2016).....	82
Table 4.2: Peak runoff rates ( $Q_{\text{peak}}$ ) and the ratio of runoff to rainfall (C) for the wet simulator runs. All LU plots are lumped together because no runoff was measured at this site. The mean and the coefficient of variation (CV) are computed for each variable. Letters within a row indicate statistical significance ( $P \leq 0.05$ ) .....	97
Table 4.3: Infiltration parameters for the lower resistivity lines for 17 of the 20 plots. Letters within a row indicate statistical significance ( $P \leq 0.05$ ). Rows without letters indicate no statistical difference amongst sites.....	100
Table 4.4: Slope and coefficient of determination ( $R^2$ ) values for the redistribution phase for the plots identified in Figure 4.8B .....	102

## LIST OF FIGURES

Figure 1.1: Experimental design. The rainfall simulator is centered over a plot with a trough and flume situated at the plot end to route and measure runoff. Two yellow ERT cables (upper and lower lines) can be seen intersecting the plot and are used to acquire time-lapse resistivity datasets .....	3
Figure 1.2: (A) Location of the UCCW denoted by a blue boundary. The Pole Mountain management unit is outline in red. (B) Nested watershed design with hydrological instrumentation. The five study sites are identified by red squares .....	4
Figure 2.1: Map of the Upper Crow Creek Watershed (UCCW) in southeastern Wyoming. The five study sites are indicated by red squares. Hydrologic instrumentation was installed in a nested watershed design in July 2009 .....	14
Figure 2.2: Hydrographs from the wet simulator runs for the five sites. Applied rainfall rate is indicated by the solid line and measured surface runoff is shown as black circles .....	24
Figure 2.3: (A) Steady state infiltration rate plotted as a function of rainfall intensity for the five sites. The response of the LU site is equal to the 1:1 line. (B) Percentage of the plot area contributing to runoff for a given rainfall intensity. Error bars represent the standard error. ....	26
Figure 2.4: Box and whisker plots for the hydrologic variables of interest: peak runoff rate ( $Q_{peak}$ ), runoff ratio (C) and the five steady state infiltration rates (SS1-SS5). Average values are indicated by an asterisk. Sites with different lower case letters are statistically different ( $p \leq 0.05$ ). The two lines of letters distinguish the different ANOVA tests i.e. including (bottom) and excluding (top) the CU-2 site.....	29
Figure 3.1: (A) Study site location in southeast Wyoming. (B) Typical experiment setup showing the rainfall simulator positioned over the runoff plot with eight CWS655 soil moisture probes and ERT measurements made on two lines of 28 electrodes each, hooked up to a multi-channel resistivity meter.....	50
Figure 3.2: Distribution of apparent resistivity data points for all seven arrays tested in forward modeling scenario 4 (Table 1) and the dipole-dipole array .....	52
Figure 3.3: (A) Resistivity as a function of volumetric water content for both the top and the bottom subsurface layers fitted using power functions. (B) Resistivity-volumetric water content data from the top layer fitted using Eq. 1 .....	57

Figure 3.4: Four resistivity profiles collected during the dry run of one of the four rainfall simulation experiments performed at the site. A background profile was collected prior to rainfall and three additional profiles were sequentially collected under a rainfall application rate of 49 mm hr <sup>-1</sup> . (A) Log of the measured apparent resistivity at different locations in the subsurface. (B) Standard inversion results (in log of resistivity) for the four profiles. A DOI contour (Oldenburg and Li, 1999) of 0.3 is overlain and indicates regions of high credibility. Iteration, RMS and L2 values describe the inversion quality. (C) Resistivity transformed into water content space. (D) Time-lapse inversion results showing percent change in resistivity. The background profile was used as the base dataset for the inversion .....	60
Figure 3.5: Time-lapse inversion results for the three different modeling scenarios outlined in Table 1 using a dipole-dipole array. Time-lapse inversion was done by differencing two profiles with the same resistivity value for the bottom layer and top layer values of 1100 ohm-m and 250 ohm-m .....	64
Figure 3.6: Time-lapse inversion results for scenario 4 outlined in Table 1. The seven different array configurations are shown with dipole-dipole included for comparison. Time-lapse inversion was done by differencing two profiles with the same resistivity value for the bottom layer and top layer values of 1100 ohm-m and 250 ohm-m .....	66
Figure 4.1: Figure 4.1: Upper Crow Creek Watershed (UCCW) and the locations of the five study sites. UCCW is comprised of two main catchments delineated by the Upper North Crow and Granite Springs reservoirs. Sub-catchments are show as part of a nested watershed design established by the University of Wyoming in 2009. Adapted from Carey and Paige (2016) .....	81
Figure 4.2: Example geophysical line bisecting the four hillslope plots. Two 13.5 m resistivity lines for the rainfall simulation experiments are also shown. Grey lines indicate the 0.5 m elevation contours .....	83
Figure 4.3: Example DOI map for the CU site. The 0.4 DOI contour is shown as a cutoff between regions of the profile that are well constrained and regions that are less constrained ....	85
Figure 4.4: (A) An example velocity model derived from the seismic surveys and clipped to match the extent of the resistivity tomograms. (B) Standard deviation among the ten independent inversions. (C) Map of the raypaths. (D) Velocity model clipped based on raypath coverage .....	87
Figure 4.5: Example hydrograph for a wet simulator run. Applied rainfall rate is indicated by the red line, measured runoff is shown by black circles and the blue line represents steady state infiltration rate (infiltration = rainfall - runoff) .....	89
Figure 4.6: An example time-lapse tomogram at the beginning of a rainfall simulation event showing the change in resistivity ( $\Delta\rho$ ) from the background condition .....	92

Figure 4.7: (A) Example  $\rho$ - $\theta$  relationship fitted with a power function. (B) Progression of the infiltration plume at three different time steps during infiltration delimited by the -10%  $\Delta\rho$  iso-contour. Position of the simulator spray area is indicated by the triangle. (C) Comparison of calculated vs. estimated infiltration area. A 1:1 line is shown with the 95% prediction interval.....94

Figure 4.8: (A) Example time-lapse tomograms from the lower resistivity lines at LU plot 4 and CU-2 plot 2. The WF, -20% and -30%  $\Delta\rho$  contours are identified. The infiltration phase is described by tomograms 1 and 2 and the redistribution phase by tomograms 3 and 4. (B) Depth to the WF versus the square root of time for the redistribution and infiltration phases. The slope of the line provides information regarding WF velocity. (C) Relationship between area of the WF derived from the time-lapse tomograms and cumulative infiltration.....99

Figure 4.9: (A) Relationship between depth to the WF and the square root of time for the infiltration phase. Sites are organized into six groups based on ANCOVA analysis. (B) Slopes and coefficient of determinations ( $R^2$ ) for all groups. The slopes of the lines are all statistically significant at the  $P \leq 0.05$  level.....102

Figure 4.10: (A) Resistivity tomograms plotted in log scale with the 0.4 DOI contour delimited by a black line. Individual resistivity scales are used for each tomogram in order to highlight unique features. Line orientation is indicated by the blue letters and root mean square (RMS) error is shown as an indicator of inversion quality. (B) Velocity models derived from seismic surveys. The 500 and 1200  $m s^{-1}$  are shown as rough estimates of the lower velocity soil/grus material and the faster velocity fractured bedrock material, respectively. All models share a common scale. (C) Radar profiles from the GPR surveys.....104

Figure 5.1: A star electrode array being used to acquire 3D time-lapse ERT datasets during a synthetic infiltration experiment (blue blocks) (after Clément *et al.*, 2011) .....126

Figure 5.2: Workflow for the multiple inversions and clustering strategy (MICS) procedure using leachate injection through a pipe as an example. A single apparent resistivity ( $\rho_a$ ) dataset is run through multiple inversions and then a clustering algorithm. Zero areas represent regions that have not been influenced by the infiltration while areas labeled one represent the infiltration plume (after Audebert, *et al.*, 2014).....128

## **Chapter 1: General Thesis Overview**

Rangelands comprise a large portion of the landmass of the western United States (~80%) and provide a multitude of goods and ecosystem services to growing human populations. The majority of our nation's energy and mineral reserves are associated with these landscapes (Kreuter *et al.*, 2016). In addition, they provide water resources, food, fiber, wildlife habitat and recreational spaces. Almost all of these ecosystem services are strongly linked to the amount of available freshwater moving through these rangeland systems and how it is partitioned among different hydrologic processes (Havstad *et al.*, 2007). The goal of rangeland managers is to optimize the amount of available water in these areas while still providing multiple ecosystem services in the face of increasing pressure from a growing population, a changing climate and increasing management expectations.

Rangelands exhibit tremendous heterogeneity in soils and vegetation. Furthermore, the majority of these environments are located in areas with an arid to semi-arid climate; precipitation is infrequent and temporally and spatially variable. These characteristics, along with a lack of observational hydrologic data, make understanding and quantifying hydrologic processes of rangelands challenging (Pilgrim *et al.*, 2003). Moreover, many of the existing tools used to evaluate the effect of management practices on rangeland water resources were not developed for rangeland environments but rather for traditional homogenized agricultural systems (Goodrich *et al.*, 2011). To deal with this landscape complexity, the ecological site (ES) framework has been adopted (Brown, 2010). ESs are recognized as the primary means to partition and classify rangelands for the purpose of developing land management objectives, performing vegetation inventory and evaluating overall ecosystem health (USDA, 2013). These sites typically represent the smallest land unit considered to be homogenous in terms of site

characteristics (e.g. vegetation type and amount, soil properties, climate, topography, etc). It is hypothesized that an ES in a given condition should exhibit a characteristic hydrologic response that can be quantified (Stone and Paige, 2003). ESs can then represent the minimum polygon for mapping the spatial variability in hydrologic response on rangelands.

Managers need robust, scientifically based hydrologic models and decision support tools (Derner *et al.*, 2012; Hanson *et al.*, 1999). Using ESs as the spatial discretization method for these models has the potential to improve their accuracy. Additionally, characterizing hydrologic processes at this scale will enhance the overall utility of the ES framework for the management of water resources. Hydrologic function of an ES is currently inferred using subjective indicators, e.g. percent bare ground and the presence of rills and gullies (Williams *et al.*, 2016). There is a need for quantitative data that relates characteristics of ESs to hydrologic processes.

The aim of this research was to describe and quantify the partitioning of rainfall into surface and subsurface flow at the ES scale. The application of hydrogeophysics to study rangeland hydrology is relatively new. I used a hydrogeophysics approach in which field experiments that used traditional hydrologic observational platforms, in this case variable intensity rainfall simulation, were coupled with well-developed geophysical techniques, primarily time-lapse electrical resistivity tomography (ERT; Figure 1.1). These field experiments were conducted on runoff plots ( $12.2 \text{ m}^2$ ) established on five ESs in the Upper Crow Creek Watershed (UCCW) in southeast Wyoming. Plots were outfitted with instrumentation to measure surface runoff. Time lapse ERT was used to track changes in subsurface resistivity distribution through time as a proxy for the infiltration plume. The five sites are representative of distinct and stable states of a given ES. The sites were sub-sampled four times to determine the site average and characterize the variability in hydrologic response.



**Figure 1.1: Experimental design. The rainfall simulator is centered over a plot with a trough and flume situated at the plot end to route and measure runoff. Two yellow ERT cables (upper and lower lines) can be seen intersecting the plot and are used to acquire time-lapse resistivity datasets.**

## Study Area

The study was located in UCCW, a rangeland watershed approximately 22 km southeast of Laramie, WY (Figure 1.2A). The watershed encompasses an area of 94 km<sup>2</sup>, the majority of which is situated within the Pole Mountain management unit of the Medicine Bow National Forest. UCCW is part of the South Platte River Basin, draining from West to East via two main streams that empty into the Upper North Crow and Granite Springs Reservoirs. Elevations range from 2200-2760 m.a.s.l. and average annual precipitation is 430 mm. Xeric grasses and shrubs

are the dominant form of vegetation (61%) while high elevations are characterized by coniferous forests (primarily lodgepole and ponderosa pine). Riparian areas are comprised of a mixture of willow, aspen and riparian grasses. Bedrock geology is predominately coarse-grained 1.43-Ga Sherman granite batholith and large boulders are exposed throughout the landscape.

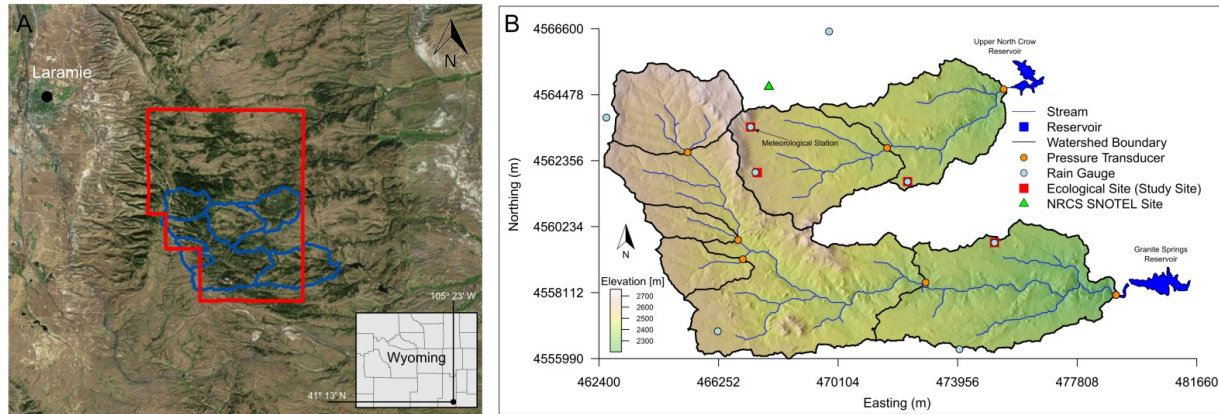


**Figure 1.2: (A) Location of the UCCW denoted by a blue boundary. The Pole Mountain management unit is outlined in red. (B) Nested watershed design with hydrological instrumentation. The five study sites are identified by red squares.**

In 2009 the University of Wyoming established a nested watershed design within the UCCW to study hydrological processes across multiple spatial and temporal scales (Figure 1.2B). In total, eight rain gauges, seven pressure transducers and four soil moisture monitoring networks were installed. A meteorological station was established (467866.9 m east, 4562880.4 m west and 2567 m.a.s.l.) to collect basic climatic data i.e. temperature, relative humidity and wind velocity. An NRCS SNOTEL site just outside the watershed boundary is used to assess snowpack dynamics. Additionally, four study sites were established and each equipped with four 12.2 m<sup>2</sup> hillslope plots to study natural rainfall-runoff processes (Figure 1.2B). These sites are representative of distinct ecological sites that are hypothesized to play a significant role in the overall hydrology of the watershed. These four sites and an additional site established in 2015

were outfitted for rainfall simulation experiments that were conducted in the summers of 2014 and 2015.

## Thesis Description

This thesis is divided into five chapters. I present a chapter with introductory materials (this chapter), three chapters that are presented as stand-alone manuscripts, and a final chapter summarizes the research results and discusses future research needs. The three main chapters are written with a specific journal in mind. As such, the formatting varies slightly between them and information in the introduction and methods sections may be repeated. At the end of each chapter's abstract the publication status of the manuscript is stated.

Chapter two of this thesis presents the results of the surface hydrologic response of these field experiments. I used an approach presented by Hawkins (1982) and revisited by Stone *et al.* (2008), to quantify the partial area runoff response for the hillslope plots. Key hydrologic variables (i.e. runoff ratio, peak runoff rate and steady state infiltration rate) were related to ES characteristics. The results directly support the concept of using ESs to assess hydrologic response on rangelands.

Chapter three is a methods paper that investigates how artifacts develop during the time lapse inversion of resistivity data acquired during rainfall simulation. Large changes in volumetric water content and the electrode configuration used for the resistivity measurements influence the development of inversion artifacts that lead to misinterpretations of subsurface dynamics. Using a single ES as a test case, I forward modeled the infiltration process to represent scenarios similar to what was observed in the field. From this work, I identify an optimal electrode array configuration for our experimental design that reduces unwanted artifacts while

still delineating the infiltration zone. This work documents an approach that is valuable for determining how to obtain proper subsurface images and reliable estimates of subsurface flow processes under these types of time-lapse infiltration experiments.

In chapter four the link was made between surface and subsurface flow processes. Geophysical tools in the form of ERT, seismic refraction and ground penetrating radar (GPR) were used to provide first-order constraints on subsurface structure for the different ESs. Jointly interpreting these results proved successful and allowed for the delineation of important material boundaries like saprolite and fractured bedrock. Using the coupled rainfall simulator-ERT experiments, the progression of the wetting front was mapped through time. The structure of the subsurface indicated by the geophysics was shown to have an influence on the velocity and distribution of the wetting front. While still in the early stages of development, the results of this work suggest that the method of coupling rainfall simulation with near surface geophysics is invaluable for discerning the surface and subsurface characteristics that distinguish the hydrologic response of diverse ESs.

This research was part of the NSF funded Wyoming Center for Environmental Hydrology and Geophysics (WyCEHG). WyCEHG is a multidisciplinary research center, which uses a hydrogeophysics approach to investigate hydrologic processes, reducing the uncertainties associated with understanding water pathways to improve water resource management. One of the principal goals of WyCEHG is to “improve understanding of mountain front hydrology by characterizing the processes that partition water into streams, soils, plants, rivers and aquifers...” at different locations throughout the state of Wyoming. This research addresses and in part satisfies this goal.

## References

- Brown, J.R., 2010. Ecological sites: Their history, status and future. *Rangelands* 32, 5-8.
- Derner, J.D., Augustine, D.J., Ascough II, J.C., Ahuja, L.R., 2012. Opportunities for increasing utility of models for rangeland management. *Rangeland Ecol. Manage.* 65, 623-631.
- Goodrich, D.C., Guertin, D.P., Burns, I.S., Nearing, M.A., Stone, J.J., Wei, H., Heilman, P., Hernandez, M., Spaeth, K., Pierson, F., Paige, G.B., Miller, S.N., Kepner, W.G., Ruyle, G., McClaran, M.P., Weltz, M., Jolley, L., 2011. AGWA: The Automated Geospatial Watershed Assessment Tool to Inform Rangeland Management. *Rangelands*. 33, 41-47.
- Hanson, C.L., Wright, J.R., Slaughter C.W., Pierson F.B., Spaeth, K., 1999. Simulation models and management of rangeland ecosystems; past, present and future. *Rangelands*. 21, 32-38.
- Havstad, K. M., Peters, D.P.C., Skaggs, R., Brown, J., Bestelmeyer, B., Fredrickson, E., Herrick, J., Wright, J., 2007. Ecological services to and from rangelands of the United States. *Ecol. Econ.* 64, 261-268.
- Hawkins, R.H., 1982. Interpretations of source area variability in rainfall-runoff relations, in: Singh V.P., (Ed), Rainfall-runoff relationships. Water Resources Publications, Littleton, CO, pp. 303-324.
- Kreuter, U.P., Iwaasa, A.D., Theodori, G.L., Ansley, R.J., Jackson, R.B., Fraser, L.H., Naeth, M.A., McGillivray, S., Moya, E.G., 2016. State of knowledge about energy development impacts on North American rangelands: An integrative approach. *J. Environ. Manage.* 180, 1-9.
- Pilgrim, D.H., Chapman, T.G., Doran, D.G., 1988. Problems of rainfall-runoff modeling in arid and semiarid regions. *Hydrol. Sci. J.* 33, 379-400.
- Stone, J.J., Paige, G.B., 2003. Variable rainfall intensity rainfall simulator experiments on semiarid rangelands, in: Renard, K.G., McElroy, S., Gburek, W., Canfield, E., Scott, R.L., (Eds.), Proceedings of the 1<sup>st</sup> Interagency Conference on Research in the Watersheds. USDA Agricultural Research Service, Washington, D.C, pp 83-88
- Stone, J.J., Paige, G.B., Hawkins, R.H., 2008. Rainfall intensity-dependent infiltration rates on rangeland rainfall simulator plots. *Trans. ASAE (Am. Soc. Agric. Eng.)* 51, 45-53.
- USDA (US Department of Agriculture). 2013. Interagency ecological site description handbook for rangelands. United States Department of Agriculture, Washington, DC, (109 pp.).
- Wilcox, B.P., Rawls, W.J., Brakensiek, D.L., Wight, J.R., 1990. Predicting runoff from Rangeland Catchments: A comparison of two models. *Water Resour. Res.* 26, 2401-2410.

Williams, C.J., Pierson, F.B., Spaeth, K.E., Brown, J.R., Al-Hamdan, O.Z., Weltz, M.A., Nearing, M.A., Herrick, J.E., Boll, J., Robichaud, P.R., Goodrich, D.C., Heilman, P., Guertin, D.P., Hernandez, M., Wei, H., Hardegree, S.P., Strand, E.K., Bates, J.D., Metz, L.J., Nichols, M.H., 2016. Incorporating hydrologic data and ecohydrologic relationships into ecological site descriptions. *Rangeland Ecol. Manage.* 69, 4-19.

## **Chapter 2: Ecological Site-scale Hydrologic Response in a Semi-arid Rangeland Watershed**

**Abstract:** Rangelands, due to their large expanse, are responsible for processing a significant portion of freshwater in the western US. Rangeland managers are in need of methods to quantify hydrologic processes and scientifically based decision tools to effectively manage water resources under growing populations and a changing climate. The ecological site (ES) concept provides a useful framework to study complex rangeland hydrological processes in order to parameterize these tools. Traditionally, rangeland hydrology has been studied at the plot and watershed scale. ESs are intermediate scale land units considered to have homogeneous site characteristics which allow for mapping the spatial variability of hydrologic processes at a higher resolution compared to a lumped watershed approach. We conducted 20 variable intensity rainfall simulation experimental runs using the Walnut Gulch Rainfall Simulator, to characterize the hydrologic response of four different ESs in the Upper Crow Creek Watershed in southeastern Wyoming. An analysis of variance test with post hoc comparisons showed that sites were significantly different in runoff-infiltration dynamics. Sites ranged from exhibiting a large runoff ratio of 0.44 to infiltrating the entire applied rainfall volume. Multiple linear regressions showed that, on average, 83% of the variability of key hydrologic variables across sites could be explained by significant relationships ( $p$  value  $\leq 0.05$ ) consisting of two or three ground cover variables. Beta weights for the regression variables indicated that percent cover of lesser spikemoss (*Selaginella densa* Rydb.) and bare soil were typically the most influential variables. Additional site-specific characteristics explain the remaining variability. The results from this study directly support the concept of using ESs to assess hydrologic response of rangelands. Incorporating quantitative hydrologic datasets into ecological site descriptions and decision tools should increase their utility for the management of rangeland ecosystems.

**Keywords:** Runoff, infiltration, ecological site, rainfall simulation

Carey, A.M., Paige, G.B., 2016. Ecological site-scale hydrologic response in a semi-arid rangeland watershed. *Rangeland Ecol. Manage.* doi:[10.1016/j.rama.2016.06.007](https://doi.org/10.1016/j.rama.2016.06.007)

*Published online in Rangeland Ecology and Management on 6 August 2016. To be published in Rangeland Ecology and Management, Volume 69, Issue 4 in September.*

## Introduction

Rangelands are estimated to comprise roughly 364 M ha of the western United States (USDA, 2013). A substantial portion of the freshwater resources that fall in the West are processed through rangeland systems. Pressure for rangeland managers to understand hydrologic processes and quantify water yield in western rangelands is increasing in the context of increased population (Havstad et al. 2009) and climate variability (Archer and Predick, 2008; Polley et al. 2013). As demand for water resources exceedingly outweighs supply, managers are in need of robust models and decision support tools that quantify the relationship between the characteristics of these rangeland systems and hydrologic processes. However, hydrologic response on rangelands is highly variable in space and time due to heterogeneities in soil, vegetation and climatic conditions, making quantifying and modeling these processes challenging (Pilgrim et al. 1988; Pierson et al. 2002; Chauvin et al. 2011).

Ecological sites (ES) can provide an effective means to partition rangelands into land units for the purpose of evaluating health, performing vegetation inventory and implementing management strategies. ESs represent distinct associations of physical characteristics such as soil, topography and climate, which produce a specific type and amount of vegetation (USDA, 2013). Characteristics differentiating these sites are outlined in ecological site descriptions (ESD) that also contain conceptual state-and-transition models (STM) to help organize complex information regarding long-term site dynamics. Ecological states are considered recognizable

and relatively stable vegetation complexes, while transitions are the trajectory between states commonly triggered by disturbance or different management strategies (USDA, 2013). Many studies have shown that hydrologic function (e.g., infiltration capacity, runoff generation, erosion) strongly influences the resilience of a given ecological state on rangelands (Wilcox et al. 2003; Newman et al. 2006; Turnbull et al. 2008). Resilience in this context is the ability of an ES to remain in a given state through mutually reinforcing processes (e.g., infiltration capacity) that work to dampen the effects of disturbance (Peterson et al., 1998). ESs therefore provide a useful framework to study the hydrological processes of rangeland systems. It has been hypothesized that an ES in a given condition or state, should exhibit a characteristic hydrologic response that can be measured (Stone and Paige, 2003; Stone et al. 2008). While rangeland hydrology has predominately been studied at plot (Simanton et al. 1991; Pierson et al. 1994) and watershed (Osborn and Lane, 1969; Loague and Gander, 1990; Wilcox et al. 1990; Flerchinger and Cooley, 2000) scales, ESs can be thought of as an intermediate scale that represent the smallest land unit considered to be homogeneous in terms of site characteristics. As such, ESs represent the minimum polygon for mapping the spatial variability of hydrologic processes and have the potential to improve the ability to model rangeland systems compared to traditional lumped watershed models (Sivapalan, 2003; Burns et al. 2010).

Hydrologic function of an ES has generally been inferred using subjective indicators e.g., percent bare ground, water flow patterns and the presence of rills and gullies (Pyke et al. 2002; Hernandez et al. 2013; Williams et al. 2016). Williams et al. (2016) recently outlined the need to incorporate quantitative hydrologic data into ESDs, to enhance their utility for the management of rangeland ecosystems. Quantitative tools such as the Rangeland Hydrology and Erosion Model (RHEM; Nearing et al. 2011), can facilitate this effort by using diverse rangeland datasets

to predict ES-specific hydrologic response (Hernandez et al. 2013; Williams et al. 2016). However, additional high quality field observations relating hydrologic function to ESs are necessary, to improve our ability to discern the characteristics that distinguish hydrologic response of ESs and improve the applicability of a model such as RHEM to a variety of different rangeland systems.

The objective of this study was to quantify the hydrologic response of four ESs in a semi-arid rangeland watershed in southeastern Wyoming. Simulated rainfall was used to relate infiltration-runoff processes to important characteristics of key ESs. Sites that differ in vegetation type and amount, topographic variability and soil properties should partition rainfall into runoff in unique and quantifiable ways. These ecohydrological relationships are important for understanding the role of specific ESs in distributing water resources in rangeland watersheds. Datasets such as these can be used to parameterize rangeland models and decision support tools, to improve the management of water resources under increased stress from population growth and a changing climate.

## Methods

### *Study Area*

This study was conducted in the Upper Crow Creek Watershed (UCCW), a 94-km<sup>2</sup> semi-arid rangeland catchment approximately 22 km southeast of Laramie, WY, USA. It is situated in the South Platte River Basin and is part of the Pole Mountain District of the Medicine Bow National Forest. UCCW drains from northwest to southeast via two main streams: the Middle Crow Creek and the South Branch of the North Crow Creek which empty into the Upper North Crow Reservoir and the Granite Springs Reservoir, respectively (Figure 2.1). Elevations range

from 2200-2760 m and average annual precipitation is approximately 430 mm. (Skinner et al. 1984). Grasses and shrubs are the dominant form of vegetation comprising roughly 61% of the watershed. Lodgepole (*Pinus contorta* Douglas ex Loudon) and ponderosa (*Pinus ponderosa* P & C. Lawson) pine are the dominant vegetation at the upper elevations and the riparian areas are comprised of a mixture of willow, aspen and riparian grasses (USDA Forest Service, 2013; Hayes et al. 2014). Bedrock geology is predominately coarse-grained 1.43-Ga Sherman granite batholith that deeply weathers to form a thick grus (Frost et al. 1999), while small slivers of the Casper Formation as well as Metasedimentary and Metavolcanic rock occur in the very northwest region of the watershed.

The University of Wyoming installed hydrologic instrumentation, rain gauges and stream gauging stations (pressure transducers) in July 2009 as part of a nested watershed design (Figure 2.1). A meteorological station was established (467866.9 m east, 4562880.4 m west and 2567 meters above sea level) to collect basic climatic data i.e. temperature, relative humidity, wind velocity, etc. Five study sites were established and each equipped with four hillslope plots, distributed across the hillslope. The plots are 6.1 m in length and 2 m in width, delimited by borders inserted a few centimeters into the soil surface. The specific location of each plot was determined based on 2 criteria: relatively uniform slope, void of any major concavities, in the soil surface between 5 and 30% and a uniform plane at least 2 m wide. Four of the five sites represent distinct ESs in the major land resource area (MLRA) 49XA and are part of a natural rainfall-runoff study conducted by Perlinski et al. (2016). The ESs represented by these four sites are coarse upland (CU), shallow loamy (SL), shallow upland (SU) and loamy upland (LU). The fifth site represents a different state of the CU STM and is termed CU-2. These sites were chosen based on areal extent and their hypothesized influence on the overall hydrologic response of the

watershed. NRCS soils data, vegetation inventory and detailed soil pits were used to verify the ES (USDA, 2013). Based on information provided in the ESDs we expect these sites to be in the reference state relative to their STMs (with the exception of CU-2). It must be noted however that ESDs are in early development for much of southeast Wyoming and this has not been directly verified.

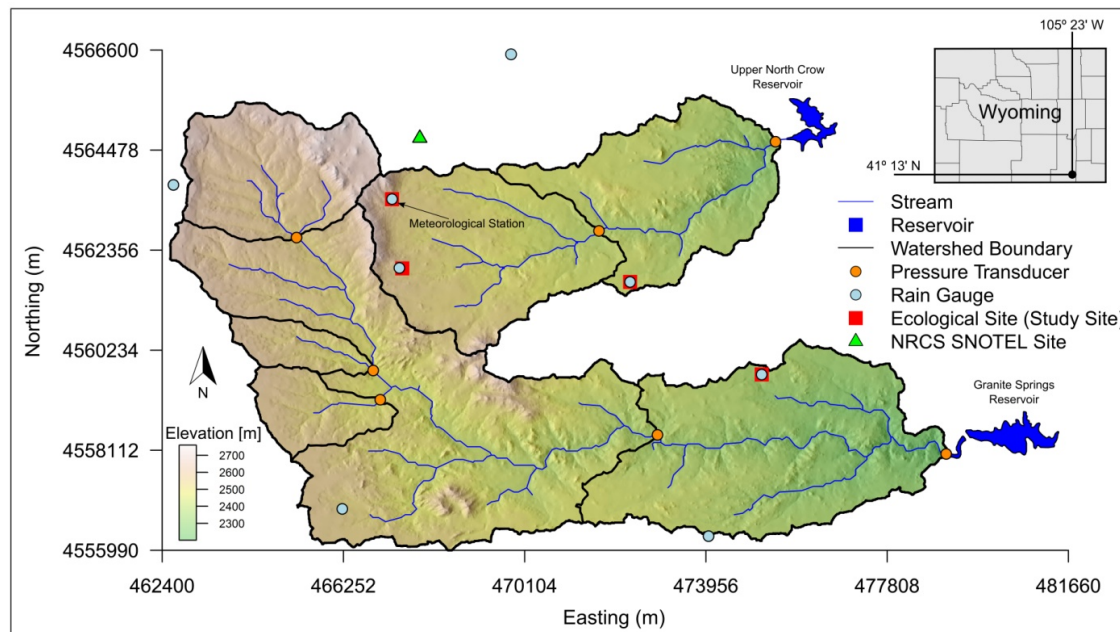


**Figure 2.1: Map of the Upper Crow Creek Watershed (UCCW) in southeastern Wyoming. The five study sites are indicated by red squares. Hydrologic instrumentation was installed in a nested watershed design in July 2009.**

Detailed characteristics of the ESs are presented in Table 2.1. The CU site is located on an alluvial fan overlaying granitic bedrock. A well developed sandy clay loam profile with an average of 34% coarse fragments (>2 mm in diameter) typically extends to a depth of 0.6 m at which point a saprolitic layer of increased coarse fragments is reached. Seismic refraction surveys indicate that fractured bedrock is about 4 m deep and that fresh bedrock is greater than 20 m deep. Grass makes up approximately 2/3 of the vegetation with the dominant species being sandberg bluegrass (*Poa secunda* J. Presl) and bluebunch wheatgrass

(*Pseudoroegneria spicata* (Pursh) Á. Löve). The remaining 1/3 of the vegetation is comprised of subshrubs primarily threetip sagebrush (*Artemisia tripartita* Rydb.) and fringed sagewort (*Artemisia frigida* Willd.). Lesser spikemoss (*Selaginella densa* Rydb.) makes up a large portion of the ground cover at this site (32%).

The SL ecological site has a similar subsurface structure as CU with a slightly deeper saprolite layer. Fresh bedrock is typically reached at about 14.7 m. Exposed granitic boulders are common upslope of this site. There is approximately 73% canopy cover dominated by blue grama (*Bouteloua gracilis* (Willd. ex Kunth) Lag. ex Griffiths), idaho fescue (*Festuca idahoensis* Elmer) and fringed sagewort. Over 40% of the ground cover is litter and Dalmatian toadflax (*Linaria dalmatica* (L.) Mill.) has invaded the site (less than 5% of the total cover).

A shallow sandy loam soil profile with over 40% coarse fragments overlays saprolite at the SU site with many large granite boulders exposed at the soil surface. Geophysical measurements show large rotting corestones at the very near surface and the average depth to bedrock is the shallowest of all the ESs (~ 11 m). The plant community is dominated by bunch grasses and idaho fescue intermixed with fringed sagewort and threetip sagebrush. Over 30% of the site is covered by a mat of lesser spikemoss, resulting in very low bare ground (~14%).

The LU ecological site is characterized by deep, highly organic loamy soils. Average depth of the soil profile at this site is typically around 0.7-0.8 m but it can be as deep as 1.3 m at localized hillslope depressions. The plant community is quite dense resulting in greater than 90% canopy cover. Big sagebrush (*Artemisia tridentata* Nutt.) overwhelmingly dominates the vegetation cover while robust shrubs like antelope bitterbrush (*Purshia tridentata* Pursh) and

western snowberry (*Symphoricarpos occidentalis* Hook.) are also very prominent. This site is also experiencing conifer encroachment, which may alter the site function.

**Table 2.1: Site descriptions for the five sites**

Site Characteristic	Coarse Upland (CU)	Shallow Loamy (SL)	Shallow Upland (SU)	Loamy Upland (LU)	Coarse Upland 2 (CU-2)
Year Established	2009	2009	2009	2009	2015 <sup>5</sup>
Ecological Site ID <sup>1</sup>	049XA108WY	049XA162WY	049XA160WY	049XA122WY	049XA108WY
Average Elevation (m)	2547	2368	2433	2567	2470
Average Slope (%)	11.5	9.6	10.7	18.6	11.9
Aspect of Hillslope Plots	South	Northwest	West	Southeast	North
Parent Material Kind <sup>1</sup>	Glacial Till, Alluvium	Residuum, Alluvium	Residuum, Colluvium	Residuum, Alluvium	Glacial Till, Alluvium
Parent Material Origin <sup>1</sup>	Granite	Granite	Granite	Sandstone	Granite
Plant Community	Wheatgrass, Bluegrass, Subshrub	Fescue, Gramma, Subshrub	Fescue, Bunch Grass, Subshrub	Dense Sagebrush, Bluegrass and Brome Understory	Wheatgrass, Fescue, Subshrub
Depth to Fractured Bedrock (m) <sup>2</sup>	4.0	5.8	3.7	6.1	9.6
Depth to Fresh Bedrock (m) <sup>2</sup>	20+	14.7	11.0	14.5	20+
Soil Map Unit <sup>3</sup>	Hapjack-Rogert- Amesmont complex	Boyle-Rock outcrop complex	Hapjack-Rogert- Amesmont complex	Rogert-Rock outcrop-Amesmont complex	Rogert-Rock outcrop-Amesmont complex
Surface Soil Type	Sandy Clay	Clay Loam	Sandy Clay	Loamy Sand	Sandy Clay
Profile Soil Type <sup>4</sup>	Sandy Clay Loam	Sandy Clay Loam	Sandy Loam	Sandy Loam	Sandy Loam
Sand, Silt, Clay (%) <sup>4</sup>	50, 26, 24	60, 18, 22	53, 29, 18	62, 22, 16	49, 46, 5
Coarse (> 2 mm) Fragments (%) <sup>4</sup>	33.9	40.5	40.5	23.2	40.9
Bulk Density (g cm <sup>-3</sup> ) <sup>4</sup>	1.58	1.56	1.47	1.37	1.58
Porosity (%) <sup>4</sup>	40.3	41.2	44.7	48.4	40.3

<sup>1</sup> Natural Resource Conservation Service (NRCS)-Ecological Site Description (ESD).

<sup>2</sup> Estimated from seismic refraction surveys.

<sup>3</sup> NRCS 2013.

<sup>4</sup> Values are for shallow soil profile

### *Rainfall Simulator Experiments*

Infiltration and runoff processes were measured using variable intensity rainfall simulation. The main advantage of rainfall simulators is the ability to generate a known rainfall pulse of specific magnitude and duration, for a controlled comparison of plots with different soil and vegetation parameters. In arid and semi-arid environments where rainfall is infrequent and spatially variable, simulators can effectively be used to study a variety of hydrologic processes (Simanton et al. 1984; Seyfried, 1991; Pierson et al. 1994, Paige and Stone, 1996; Taucer et al. 2008; Stone et al. 2008).

A total of 20 rainfall simulator experimental runs were conducted (four runs at each of the five sites) during the summers of 2014 and 2015 using the Walnut Gulch Rainfall Simulator (WGRS; Paige et al. 2003). The WGRS is a portable, variable-intensity rainfall simulator developed by the USDA-ARS-Southwest Watershed Research Center, to study the spatial variability of infiltration-runoff processes on rangelands at the hillslope scale (Paige et al. 2003; Stone et al. 2008). It is equipped with four VeeJet 80100 nozzles mounted to a 6 m central oscillating boom that is driven by a computer controlled stepper motor. Water is delivered to the boom via a WT20 Honda trash pump from a nearby 1650 gal tank. An in-line pressure regulator allows for a constant outflow pressure to be set and maintained. The WGRS uses variable delay times between boom oscillations and different oscillation angles to achieve a large range (27-311 mm hr<sup>-1</sup>) of applied rainfall intensities. Screens on three sides of the simulator minimize the effects of wind on the rainfall distribution. Each year the simulator was calibrated prior to deployment in the field to verify the applied rainfall intensities and distribution across the plot.

Field runs consisted of performing two simulator runs on each plot, a dry and a wet run. All plots were equipped with instrumentation specifically designed for simulation experiments.

The WGRS was positioned directly over the plots with nozzles approximately 2.4 m above the soil surface and a constant nozzle outflow pressure of 55 kPa was maintained using a regulator to control dropsize distribution and rainfall intensity. These target values for nozzle height and outflow pressure were determined to achieve the desired rainfall distributions and a rain-drop kinetic energy similar to that of natural rainfall (Paige et al. 2003). The dry runs were performed under antecedent soil moisture conditions. For all sites excluding LU, soil volumetric moisture prior to simulation averaged 15% (SE = 1.5%). Antecedent soil moisture for the LU site was slightly higher at 23% (SE = 5%). For the dry runs rainfall was applied to the plots at the lowest intensity (49 mm hr<sup>-1</sup> for 2014 and 53 mm hr<sup>-1</sup> for 2015) for approximately 45 minutes. This was done to establish a uniform moisture condition. After allowing time for moisture redistribution (hiatus period with no rainfall typically lasting 45 min to 1hr), a wet run was conducted by incrementally increasing the applied rainfall using five calibrated intensities (49, 77, 112, 157 and 180 mm hr<sup>-1</sup> for 2014 runs and 53, 81, 115, 153 and 181 mm hr<sup>-1</sup> for 2015 runs). Surface runoff rates were continuously measured throughout both runs by routing flow from the plots through a pre-calibrated flume. A given rainfall intensity was applied until steady state runoff was reach for a minimum of five minutes, at which point the intensity was increased. A series of eight CWS655- 900 MHz, wireless reflectometer probes (Campbell Scientific, Inc, Logan, UT) were evenly distributed across the plot to monitor near surface soil moisture dynamics.

Simulations for the CU and LU sites were conducted in 2014 (eight plots total) while simulations for SL, SU and CU-2 were conducted in 2015 (twelve plots total). It typically took about a week to complete all four plot simulations for a given site.

A series of hydrologic variables were computed for all wet runs. Steady state infiltration rates (SS) for each of the five applied intensities (SS1-SS5) were calculated by subtracting the

measured steady state runoff rate from the applied rainfall intensity. This represents an integrated plot-scale infiltration rate under a particular rainfall condition. Runoff coefficients (C), a unitless value defined as the fraction of rainfall that results in surface runoff, were computed by dividing the total depth of runoff by the total applied rainfall over the course of the wet run. The peak runoff rate ( $Q_{\text{peak}}$ ) for the entire wet run was also noted.

#### *Site Characteristics*

Ground and vegetative canopy cover were measured for each plot post rainfall simulation using a point-intercept method (Herrick et al. 2005). Characteristics were recorded at 380 points within each plot (30 cm spacing down the length and 10 cm spacing across the plot). Canopy cover was characterized based on life form as well as species and ground cover was classified as: bare soil, rock, litter, moss, plant base or exposed rock. To compute percent canopy cover, the first-hit of the vertically descending rod was used as the frequency measurement, though multiple hits may be recorded. Bulk density and porosity was determined for each site using undisturbed soil cores (Gee and Or, 2002).

Steady state infiltration rates were analyzed using a procedure presented by Hawkins (1982) and revisited by Stone et al. (2008). Assuming an exponential distribution of infiltration capacity across a given area, Hawkins derived the following equation that relates steady state infiltration rate to the applied rainfall rate:

$$f_S(i) = \mu_f \left(1 - e^{-\frac{i}{\mu_f}}\right) \quad [1]$$

where  $f_S(i)$  is the steady state infiltration rate ( $\text{L T}^{-1}$ ),  $i$  is the applied rainfall rate ( $\text{L T}^{-1}$ ) and  $\mu_f$  is the average areal infiltration rate when the entire area under consideration is contributing to runoff ( $\text{L T}^{-1}$ ). The  $\mu_f$  parameter can also be thought of as the maximum spatially averaged infiltration rate for a given area. Eq. 1 suggests that steady state infiltration increases with

increasing application rate until the maximum infiltration rate ( $\mu_f$ ) is asymptotically reached.

The spatial distribution of infiltration capacity across a given area will determine the shape of the response curve. As the applied rainfall rate increases, areas with higher infiltration capacity begin to contribute to runoff resulting in an increase in the steady-state infiltration rate. Eq. 1 has been effectively tested using rainfall simulation data (Stone et al. 2008) as well as natural rainfall-runoff data (Yu et al. 1997). For our analysis the  $\mu_f$  parameter was calculated by fitting a line through the five  $(i, f_S)$  points collected during the wet simulator run, by minimizing the root mean squared error. Using the exponential distribution of infiltration capacity, a cumulative density function can be used to compute the fraction of an area that is contributing to runoff:

$$A_C(i) = 1 - e^{-\frac{i}{\mu_f}} \quad [2]$$

where  $A_C(i)$  is the fraction of the total area for a given rainfall intensity.

### *Statistical Analysis*

Hydrologic variables of interest (i.e. SS1-SS5, C and  $Q_{peak}$ ) were compared among all five sites using a one way analysis of variance (ANOVA) test set in a completely randomized design. Post hoc average separations were conducted using Tukey's HSD (Tukey, 1953) if the F-tests indicated significant differences amongst sites. All data used in the ANOVA were tested for normality. The assumption of equal variances was tested using Hartley's ratio (Hartley, 1950). If the variances were unequal, a weighted analysis was conducted using the inverse of the square root of the variances as weights. All ANOVA computations were performed using the GLM procedure of the Statistical Analysis System (SAS) version 9.4 (SAS Institute, 2013).

Multiple linear regression was used to identify site cover characteristics that may be important in predicting the hydrologic response. Percent slope also was used in this analysis as

an explanatory variable. All regressions were performed using R Statistical Software version 3.1.1 (R Development Core Team, 2014). A forward selection procedure was chosen in which Pearson correlation coefficients were used to identify the starting variable for the model and subsequent variables were added to the model based on partial F-tests (Kleinbaum et al. 1988). Backward procedures were also tested, in general resulting in more complex models not significantly different than forward results with poor variable inflation factors. Therefore, only the results from the forward procedure are presented. Prior to analysis, all data used in the regressions were tested for normality and equal variance. Model selection was performed by minimizing both the Akaike information criterion and the predictive residual sum of squares. All models discussed are significant at the  $p \leq 0.05$  level.

## Results

Hydrographs for the wet runs from the 20 plots illustrate differences in the hydrologic response of the five ES (Figure 2.2). The SU site had the largest runoff response, indicated by the site average  $Q_{\text{peak}}$  and C values (Table 2.2). For all four plots runoff was generated at the lowest applied rainfall intensity ( $53 \text{ mm hr}^{-1}$ ). Steady state runoff was achieved during the dry run for plots 1 and 4 indicating that these plots have an especially low infiltration capacity. Moreover, SU exhibited the lowest amount of within site variability in runoff among all ESs. This is indicated by the similar plot hydrographs and the low standard error (SE) and coefficient of variation (CV) values for  $Q_{\text{peak}}$  and C. On average, the CU site had the second highest runoff response. Plot values for  $Q_{\text{peak}}$  and C were similar for plots 3 and 4, while slightly higher for plot 1. Substantially lower values for plot 2 lead to a high degree of variability in hydrologic response across this site compared to SU. For the SL site, significant runoff did not begin until later in the

experiment when soil moisture was higher and higher rainfall intensities were applied. This site exhibits a higher infiltration capacity than the SU and CU sites. While the other three sites exhibited a similar CV for  $Q_{peak}$  and C, the SL site had a significantly higher CV for C compared to  $Q_{peak}$ . This is due to plots 3 and 4 where runoff rates only began to increase towards the end of the simulation experiment. The site that exhibited the highest degree of variability in runoff generation across the hillslope was the CU-2 site. For a similar pattern in rainfall application, it can be seen that plot 1 had a  $Q_{peak}$  over 12 times greater than plot 3 and a C nearly 36 times larger. Plots 1 and 2 produce small amounts of runoff at the lowest rainfall intensity, while runoff did not begin until an intensity of  $115 \text{ mm hr}^{-1}$  for plot 3. Of all the ESs, LU overwhelmingly has the largest potential to infiltrate water. This is shown by the absence of runoff during all four simulation runs. The site effectively acted as a sponge, infiltrating all rainfall that was applied.

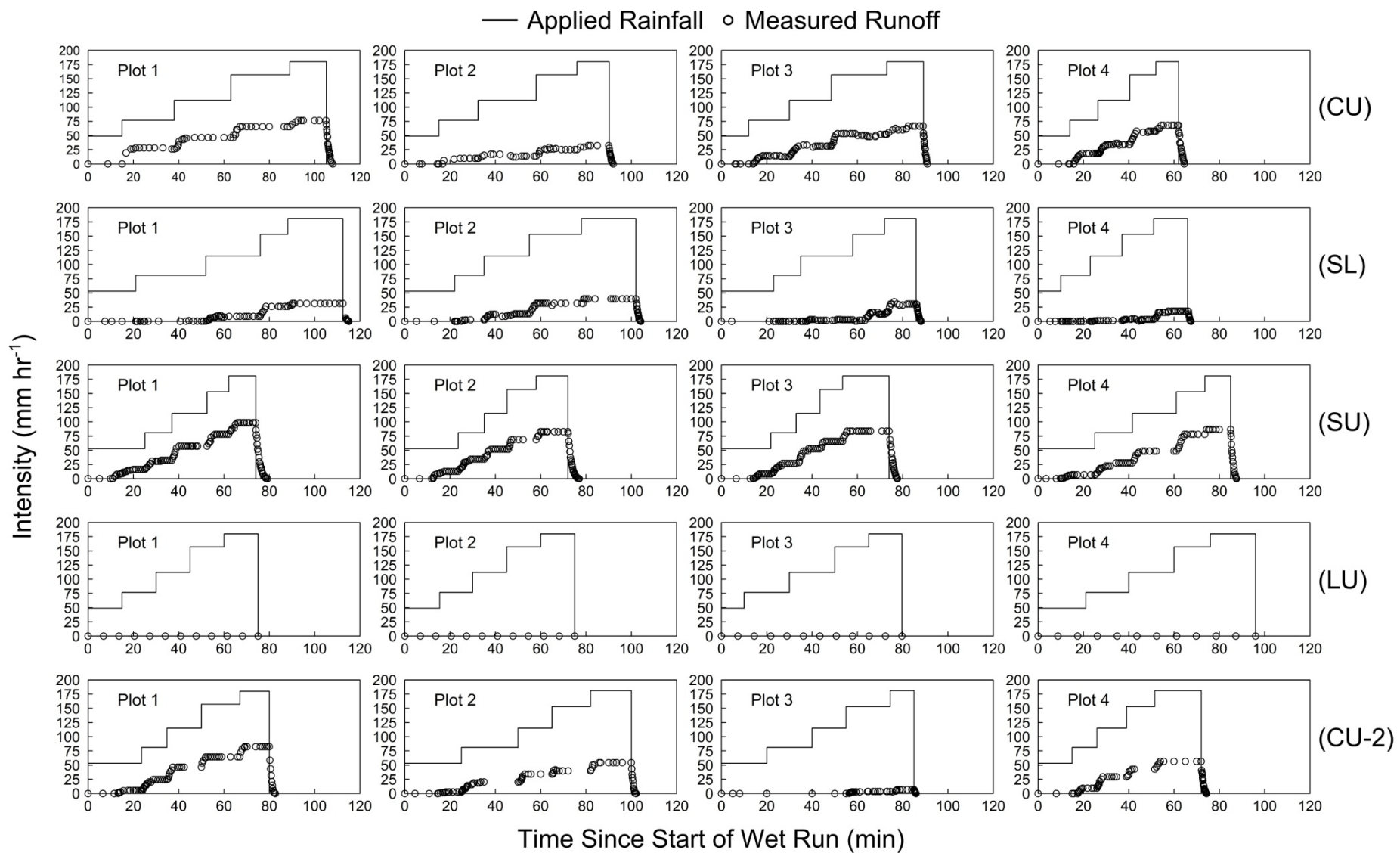


**Figure 2.2: Hydrographs from the wet simulator runs for the five sites. Applied rainfall rate is indicated by the solid line and measured surface runoff is shown as black circles.**

**Table 2.2: Peak runoff rates ( $Q_{\text{peak}}$ ) and runoff ratios (C) for 16 of the 20 wet simulator runs. The LU site is not shown because there was no runoff for any simulation experiment at this site. Averages, standard errors (SE) and coefficient of variations (CV) are computed for each site.**

Ecological Site	Plot	$Q_{\text{peak}}$ (mm hr <sup>-1</sup> )	C	$Q_{\text{peak}}$		C	
				Average (SE)	CV (%)	Average (SE)	CV (%)
CU	1	76.4	0.38	60.9 (9.8)	32.0	0.27 (0.05)	36.3
	2	32.4	0.14				
	3	66.8	0.29				
	4	68.2	0.30				
SL	1	31.5	0.10	29.9 (4.4)	29.5	0.09 (0.03)	56.9
	2	39.5	0.15				
	3	30.6	0.06				
	4	18.1	0.04				
SU	1	98.5	0.44	87.9 (3.6)	8.3	0.40 (0.01)	6.7
	2	82.7	0.39				
	3	83.8	0.38				
	4	86.5	0.38				
CU-2	1	82.5	0.36	50.0 (15.8)	63.2	0.21 (0.07)	67.7
	2	54.3	0.24				
	3	6.7	0.01				
	4	56.4	0.24				

Differences in the infiltration capacity across these sites can be seen in the areal average infiltration curves from Eq. 1 and 2 (Figure 2.3A). Variability in infiltration capacity within a given site, indicated by error bars representing the SE, follows the same trend outlined by the individual plot hydrographs. The thin straight line in Figure 2.3A representing the LU site, also serves as the 1:1 line in which the rainfall intensity is equally matched by the site's ability to infiltration water. From these curves  $\mu_f$  values were calculated for each plot (Table 2.3). A normal site average  $\mu_f$  value was calculated using all four plots and an adjusted average was calculated excluding anomalous plots. For the CU, SL and CU-2 sites, variability in the values of the normal averages are influenced strongly by a single anomalous plot. For example, plot 3 of the CU-2 site has a  $\mu_f$  value approximately 21 times larger than the average of the remaining

three plots. With these plots removed, variability in response is reduced and the adjusted averages follow the previously mentioned trend in infiltration capacity. Adjusted values were not calculated for the SU and the LU sites due to low (and in the case of LU, zero) variability in the normal  $\mu_f$  averages. It is important to note that no plot during the wet simulator run ever reached its  $\mu_f$  value in which 100% of the area was contributing to runoff (Figure 2.3B). The SU plots were the closest to approaching this condition, with an average of 83% of the plot area contributing to runoff at the highest applied rainfall intensity. This is compared to less than a third (28%) of the plot area contributing to runoff for the same rainfall intensity at the SL site. CU and CU-2 fall in the middle of these two sites with 62% and 49% of the area contributing to runoff, respectively. LU had 0% area contributing to runoff at the highest rainfall intensity.

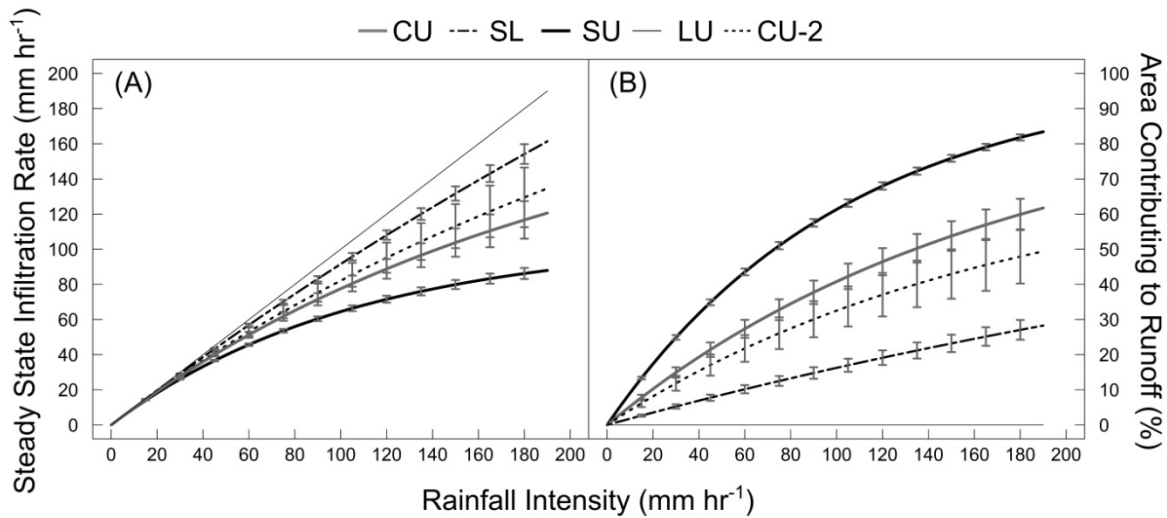


**Figure 2.3:** (A) Steady state infiltration rate plotted as a function of rainfall intensity for the five sites. The response of the LU site is equal to the 1:1 line. (B) Percentage of the plot area contributing to runoff for a given rainfall intensity. Error bars represent the standard error.

**Table 2.3: Maximum spatially averaged infiltration rate ( $\mu_f$ ) values for the five ecological sites. Normal averages and coefficients of variations (CV) are computed using all four plots. Adjusted averages and CVs are computed after removing anomalous plots.**

Ecological Site	$\mu_f$ (mm hr <sup>-1</sup> )				Normal		Adjusted	
	Plot 1	Plot 2	Plot 3	Plot 4	Average (SE)	CV (%)	Average (SE)	CV (%)
CU	130	430	178	163	225 (69.0)	61.2	157.0 (14.2) <sup>1</sup>	15.6 <sup>1</sup>
SL	471	361	645	1312	697 (213.1)	61.1	492.3 (82.7) <sup>2</sup>	29.1 <sup>2</sup>
SU	89	112	116	106	106 (5.9)	11.3	-- <sup>3</sup>	--
LU	Inf <sup>5</sup>	Inf	Inf	Inf	--	--	--	--
CU-2	124	221	4184	224	1188 (998.9)	168.12	189.7 (32.8) <sup>4</sup>	30.0 <sup>3</sup>

<sup>1</sup> Values excluding CU plot 2

<sup>2</sup> Values excluding SL plot 4

<sup>3</sup> Value not calculated

<sup>4</sup> Values excluding CU-2 plot 4

<sup>5</sup>  $\mu_f$  is effectively infinite i.e. steady state infiltration rate is equal to the applied rainfall rate

With the CU-2 site exhibiting a high degree of variability in hydrologic response across the hillslope plots, two separate ANOVA tests were conducted with and without the CU-2 dataset (Figure 2.4).  $Q_{peak}$  was statistically different across all four sites when CU-2 was excluded. These site differences were still preserved with the addition of CU-2, however no statistical difference was found between CU and CU-2. Averages for C show a dichotomy in the sites, where CU and SU on average have a higher fraction of applied rainfall turning in to runoff compared to SL and LU. This pattern also remains with the addition of the CU-2 site but CU and SL become indistinguishable from CU-2. Excluding the CU-2 dataset, the trend for the differences between sites is preserved for all five of the steady state infiltration rates, with a few exceptions. SS2 and SS3 have identical results where SL and LU are grouped together and different from the remaining two sites. When the steady state infiltration rates are higher (SS4 and SS5) the uniqueness of the LU site emerges and all sites become statistically different. It is

important to note that for SS1 some of the observed differences are a result of the applied rainfall rate. For example, the analysis shows that the steady state infiltration rate for SL is statistically higher than that of CU (both with and without the CU-2 dataset). This is due to the fact that the lowest applied rainfall intensity for 2014 was  $49 \text{ mm hr}^{-1}$  and  $53 \text{ mm hr}^{-1}$  for 2015. Both sites are infiltrating water at a rate that equally matches the application rate (i.e. no runoff). It is likely that if an equal intensity was applied to the plots there would be no differences between the two sites. In general, addition of the steady state infiltration rates from CU-2 site results in two main changes: (1) there is no significant difference between CU and CU-2 and (2) there is no significant difference between SL and LU.

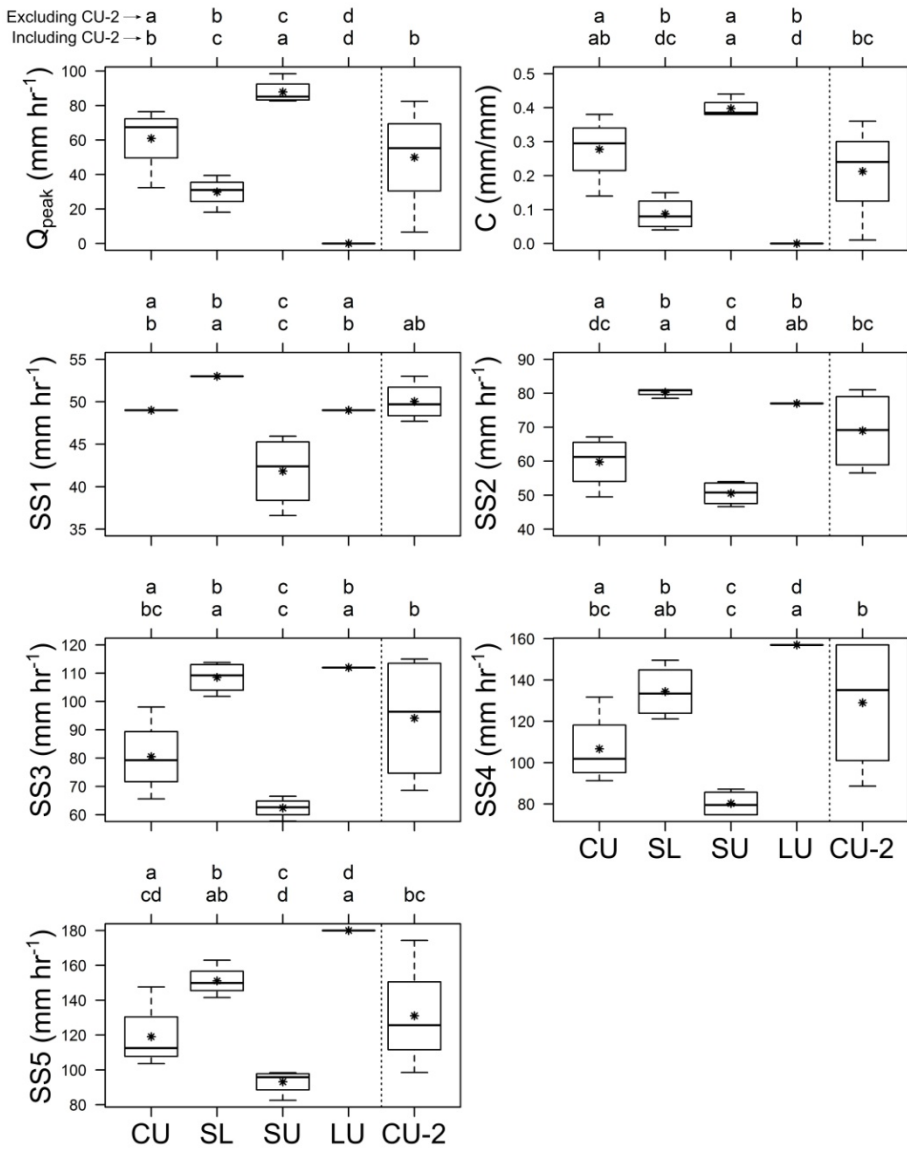


**Figure 2.4: Box and whisker plots for the hydrologic variables of interest: peak runoff rate ( $Q_{\text{peak}}$ ), runoff ratio ( $C$ ) and the five steady state infiltration rates (SS1-SS5). Average values are indicated by an asterisk. Sites with different lower case letters are statistically different ( $p \leq 0.05$ ). The two lines of letters distinguish the different ANOVA tests i.e. including (bottom) and excluding (top) the CU-2 site.**

Vegetation characteristics (Table 2.4) were used as explanatory variables for the regression equations (Table 2.5). These equations explain a large amount of the variation in hydrologic response across sites. Ground cover characteristics were the only variables to emerge

as being significant in the modeling process. Among these variables, moss and bare soil were consistently identified as important cover parameters for describing both runoff and infiltration processes. On average, these simple two and three parameter regression equations explain 82% of the variability in steady state infiltration rates, excluding SS1. A poor fit for SS1 is attributed to the fact that out of the 20 plots tested, 14 infiltrated at a rate equal to the applied rainfall rate. This leads to an insufficient amount of variability among sites to fit through the regression procedure. The fits improve for  $Q_{peak}$  and C with explained variability of 84% and 85%, respectively.

**Table 2.4: Ground and canopy cover characteristics for the 20 runoff plots.**

Site	Plot	Ground Cover (%)					Canopy Cover (%)				No Canopy	
		Bare Soil	Rock <sup>1</sup>	Litter	Moss <sup>2</sup>	Plant Base	Exposed Rock <sup>3</sup>	Grass	Shrub <sup>4</sup>	Forb		
CU	1	11.6	10.8	32.4	38.2	7.1	0.0	17.9	18.9	5.5	0.0	57.6
CU	2	11.6	20.5	45.0	12.1	10.8	0.0	45.3	17.6	1.8	4.5	30.8
CU	3	10.8	12.4	32.1	30.1	13.7	0.0	50.3	17.1	6.6	2.9	23.2
CU	4	4.2	8.7	26.6	46.6	14.0	0.0	30.0	11.3	12.6	0.0	46.1
SL	1	4.7	9.2	30.5	34.7	20.8	0.0	33.7	20.8	15.3	0.0	30.3
SL	2	6.8	10.3	55.3	6.3	21.3	0.0	43.4	26.1	6.8	0.0	23.7
SL	3	8.2	12.9	47.6	13.4	17.9	0.0	35.8	27.4	11.6	0.0	25.3
SL	4	4.2	19.5	41.6	22.9	11.8	0.0	43.7	15.5	13.9	0.0	26.8
SU	1	7.9	0.0	53.7	21.6	16.8	0.0	43.7	11.8	20.8	0.0	23.7
SU	2	10.3	6.8	33.2	38.4	11.3	0.0	57.9	9.2	9.5	0.0	23.4
SU	3	13.7	3.4	30.5	43.7	8.7	0.0	46.1	18.4	6.6	0.0	28.9
SU	4	7.1	6.6	44.2	35.5	5.8	0.8	37.1	16.3	6.1	0.0	40.5
LU	1	17.6	0.5	64.0	0.0	16.1	1.8	18.4	38.9	17.9	8.9	15.8
LU	2	7.4	0.5	81.6	0.0	9.0	1.6	17.9	50.5	5.0	14.7	11.8
LU	3	6.6	1.6	87.6	0.0	4.2	0.0	51.8	29.5	10.3	4.7	3.7
LU	4	4.5	0.0	92.1	0.0	3.4	0.0	54.2	31.1	5.0	1.1	8.7
CU-2	1	4.2	4.0	31.8	52.1	7.9	0.0	40.5	5.8	5.5	0.0	48.2
CU-2	2	2.1	8.2	32.4	47.4	10.0	0.0	34.5	11.6	9.2	0.0	44.7
CU-2	3	3.2	7.6	68.2	7.6	13.4	0.0	89.7	4.5	1.3	0.0	4.5
CU-2	4	7.1	5.0	41.6	26.6	19.7	0.0	88.9	0.5	5.3	0.0	5.3

<sup>1</sup> Rock cover is considered to be rock fragments greater than 2 cm in diameter

<sup>2</sup> Lesser spikemoss (*Selaginella densa* Rydb)

<sup>3</sup> Granitic boulders exposed at the soil surface

<sup>4</sup> Small subshrubs (*Artemisia frigida* Willd and *Artemisia tripartita* Rydb) for CU, SL, SU and CU-2. Big sagebrush (*Artemisia tridentata* Nutt) for LU.

**Table 2.5: Forward regression equations for the wet simulator runs using vegetation transect data as the explanatory variables and the five steady state infiltration rates (SS1-SS5), runoff coefficient (C) and peak runoff rate ( $Q_{peak}$ ), as the dependant variables. All equations are significant at the  $p \leq 0.05$  level. Explanatory variables are shown with beta weights and significance codes.**

Variable	SS1 (mm hr <sup>-1</sup> )	SS2 (mm hr <sup>-1</sup> )	SS3 (mm hr <sup>-1</sup> )	SS4 (mm hr <sup>-1</sup> )	SS5 (mm hr <sup>-1</sup> )	$Q_{peak}$ (mm hr <sup>-1</sup> )	C (mm/mm)
Intercept	50.25***	78.73***	171.52***	168.01***	191.39***	-10.52	-0.57*
Variable 1 (beta weight)	0.34 Plant Base** (0.54)	-0.52 Moss*** (-0.79)	-1.53 Moss*** (-1.39)	-1.40 Moss** (-0.89)	-1.61 Moss*** (-0.91)	1.10 Moss** (0.63)	0.01 Moss*** (1.28)
Variable 2 (beta weight)	-0.41 Bare Soil** (-0.49)	0.87 Plant Base** (0.39)	-2.17 Bare Soil*** (-0.43)	-1.71 Bare Soil <sup>†</sup> (-0.24)	-1.98 Bare Soil* (-0.25)	3.48 Bare Soil** (0.47)	0.02 Bare Soil*** (0.60)
Variable 3 (beta weight)	-0.07 Moss* (-0.39)	-1.12 Bare Soil** (-0.37)	-0.54 Litter* (-0.55)			-1.52 Rock <sup>†</sup> (-0.29)	0.01 Litter* (0.58)
R <sup>2</sup>	0.62	0.84	0.85	0.78	0.82	0.84	0.85

Significance Codes: \*\*\* p ≤ 0.0001 \*\* p ≤ 0.001 \* p ≤ 0.01 † p ≤ 0.05

## Discussion

Our rainfall simulation results demonstrate the variability in hydrologic response as a function of ES characteristics. Site response ranged from consistently producing runoff at each applied rainfall rate (SU) to infiltrating the entire applied rainfall volume, resulting in no runoff (LU). Response curves for steady state infiltration and area contributing to runoff (Figure 2.3) as well as ANOVA results (Figure 2.4), indicate the following sequence of increasing site infiltration capacity: SU, CU, CU-2, SL and LU. This is consistent with work by Perlinski et al. (2016) which monitored natural runoff response from the same ecological sites (excluding CU-2). High  $R^2$  values of 0.78 to 0.85 for the regression equations (Table 2.5), illustrate the effectiveness of using pooled data across all five ESs to explain this variability. As previously mentioned, little confidence can be placed in the regression results for SS1 and it is therefore excluded from this discussion. Site-specific regression equations have been shown to improve the ability to predict hydrological processes compared to lumped equations (Spaeth et al. 1996; Pierson et al. 2002). For our experiments an insufficient number of data points prevented the development of site-specific equations. However, our results suggest that simple more universal equations containing only ground cover characteristics can be used to describe hydrologic process at multiple locations within the UCCW. This can be attributed to the fact that the structure of the plant community is fairly consistent across our study locations, with the exception of the LU site (Table 2.4). Various graminoid species are typically intermixed with two dominant species of small subshrubs: fringed sagewort (*Artemisia frigida* Willd) and threetip sagebrush (*Artemisia tripartita* Rydb). There is no statistical difference in grass cover across sites and only the CU-2 site had a significantly lower amount of shrub cover (Table 2.4).

Therefore, ground cover characteristics emerged as being the only important variables for explaining these differences.

Two ground cover variables were consistently identified as significant: (1) lesser spikemoss and (2) bare soil. Lesser spikemoss was the most influential variable in each of the equations as indicated by the beta weights (Table 2.5). This vascular plant grows as a dense mat with a network of fine roots extending 2 to 5 cm below the soil surface (Coupland and Johnson, 1965). Low water-use requirements make it prevalent in rangeland systems, affecting the structure and composition of plant communities (Colberg and Romo, 2003; Romo, 2011). It has been noted that this cryptogam can act as a sponge during rainfall events, preventing moisture from reaching surrounding vegetation (Majorowicz, 1963). Observations during field experiments suggest that once these plants absorb a small amount of moisture they effectively create impervious patches in which rainfall is directly converted into surface runoff. The amount of lesser spikemoss present at these sites is negatively correlated with SS infiltration rates and positively with C and  $Q_{peak}$  (Table 2.5). Bare soil is also negatively correlated with infiltration. This strong negative relationship has been noted by a number of different authors (Branson and Owen, 1970; Blackburn, 1975; Pierson et al. 2002). Minimal organic matter, lack of root systems, high overland flow velocities and the sealing of the soil surface due to particles dislodged from rainfall impact, are all factors that contribute to the reduced infiltration rates of these areas. For SS4, SS5,  $Q_{peak}$  and C, bare soil was the second most influential variable.

A combination of lesser spikemoss and bare soil cover is the basis for all of the regression relationships. For SS4 and SS5, these two variables alone make up the equations and can explain 78 and 82 % of the variability, respectively. At these steady state infiltration rates the applied rainfall rate is quite large and a parsimonious model that ultimately characterizes the

fraction of the plot with low infiltration areas (i.e. percent cover of lesser spikemoss and bare soil), is sufficient for explaining a large degree of the variability in infiltration. For the lower intensities the regression relationships for SS2, SS3 and  $Q_{peak}$  (Figure 2.4) require slightly more complex three-parameter models and variables like litter, plant base and rock become significant. In our experiments plant base and rock cover were positively correlated with infiltration. Plant base is a proxy for standing biomass and therefore root systems that aid in the infiltration of water and the increased roughness of the soil surface due to rock fragments favors greater and more rapid infiltration (Cerdá, 2001). While others have shown that litter cover increases infiltration (Wilcox et al. 1988; Meeuwig, 1970) our results suggest a negative relationship.

In addition to describing the difference in hydrologic response across ES, these relationships prove useful for explaining within-site variability. Fitted  $\mu_f$  values (Table 2.3) show that the maximum spatially averaged infiltration rate at some sites can vary substantially from plot to plot. While adjusting the average  $\mu_f$  value by removing anomalous plots provides a more representative estimate of site-specific infiltration capacity, these anomalous plots are well predicted by the regression equations. For example, CU plot 2 and CU-2 plot 3 have  $\mu_f$  values 1.7 and 21 times greater than the average  $\mu_f$  value for the remaining three plots at the sites, respectively. These plots therefore have higher steady state infiltration rates and lower  $Q_{peak}$  and C values. In each case, the lack of lesser spikemoss coverage can explain this increase in infiltration. The CU site on average has 38.6% moss coverage while CU-2 has 42.0%. In contrast, CU plot 2 had 12% moss coverage and CU-2 plot 3 had 7.6% (Table 2.4).

As aforementioned, the CU-2 site is unique in this study in that it is not a distinct ES but rather a different state of the CU STM. CU can be considered a mixed shrub/grass plant community with approximately 36% of the vegetation being grasses and 16% being shrubs.

Sandberg bluegrass is the dominant vegetation species. While the ESD indicates a big sagebrush component, vegetation transects showed that fringed sagewort and threetip sagebrush are the dominate shrub species (Table 2.4). The CU-2 site represents a more historic climax plant community that evolved with grazing (NRCS, 2014). Grasses on average make up approximately 63% of the vegetation with bluebunch wheatgrass being the most prominent species. Shrubs are not as significant to the plant community as in the CU state. CU and CU-2 are the same ES, however shifts in the state can alter the plant community and in return influence the hydrologic response of this landscape unit. Including CU-2 in the ANOVA analysis (Figure 2.4) results in no statistical difference between CU and CU-2 for any of the hydrological parameters, however the variability in response increases. It may also be possible that CU-2 is transitioning either towards or away from the CU site. For example, vegetation characteristics and consequently the hydrologic response for plots 1 and 2 closely resemble that of the CU site. Quantifying this range in response is important for effectively using the ES concept to model hydrologic processes.

Site-specific hydrologic interactions must also be addressed as a source of variability not explained by the regression equations. The LU site for instance is unique compared to the other four sites in its parent material, structure of the plant community and soil properties (Table 2.1). The site has 90% canopy cover of which 42% is big sagebrush (*Artemisia tridentata* Nutt), creating a sagebrush shrub-interspace complex consisting of different surface microsites (Pierson et al. 1994). There is no evidence of lesser spikemoss at the site due to the fact that the soils were derived from Metasedimentary rock instead of granite (Beetle, 1956). Differences in runoff and infiltration were observed for these different microsites. During simulation runs, water ponded on the soil surface of the interspaces quicker than any of the other four sites. As water migrated from these interspaces to the shrub areas, infiltration occurred rapidly. Additional rainfall

simulation runs (not presented in this paper) were conducted at this site in the fall of 2015, in which the applied rainfall intensity was as high as  $311 \text{ mm hr}^{-1}$ . Again, no runoff was observed on any of the four plots tested. This suggests that this site effectively never exhibits Hortonian overland flow under natural conditions and is instead dominated by subsurface processes driven by the high infiltration capacity of the big sagebrush areas (Ryel et al. 2003; Eldridge and Rosentreter, 2004).

The shallow ESs (SU and SL) also exhibit distinct site characteristics that are important for understanding the hydrologic response. Geophysical measurements suggest that SU has the smallest average depth to fractured bedrock of all the sites (Table 2.1). Moreover, large granite boulders are intermixed within the soil profile and are often exposed at the soil surface. Localized regions of saturation due to these impervious zones in the subsurface were evident during simulation runs. SU plot 1 for example has a large granite boulder approximately 1.2 m below the soil surface that spans the length of the runoff plot. Reflectometer probes showed that prior to simulator runs the region above this granite layer was at 34% water content and during the wet runs water content increased by only 1.4%. Furthermore, this plot yielded significant steady state runoff ( $16.4 \text{ mm hr}^{-1}$ ) during the dry run. Therefore, saturation excess due to impervious regions of the subsurface may help explain why SU plot 1 had the highest C (0.44) and  $Q_{\text{peak}}$  ( $98.5 \text{ mm hr}^{-1}$ ) of the 20 plots tested. At the SL site the infiltration capacity is large (Figure 2.3), second only to LU. Plot 4 however has a C of just 0.04 compared to an average C of 0.11 for the remaining three plots. The density of pocket gopher burrows on this plot may help to explain this trend. The average density of these burrows was  $0.25 \text{ m}^{-2}$  for plots 1 – 3 while  $1.7 \text{ m}^{-2}$  for plot 4. Tagging the surface runoff using dye tabs showed water preferentially infiltrating into these burrows.

## **Conclusion**

In this study, a dataset of extensive field observations was developed using variable intensity rainfall simulation runs that directly relates hydrologic response to rangeland ES characteristics. We show that characteristics of ESs in a given state can be used to quantify the variability in hydrologic response across a semi-arid rangeland watershed in southeastern Wyoming. While some sites exhibit spatially variable  $\mu_f$  values at the plot scale, we are able to compute meaningful site average values that outline the differences in the maximum infiltration capacity at the ES scale. Moreover, we derived parsimonious equations consisting only of ground cover variables (e.g. moss cover, bare soil and litter) capable of explaining on average, 83% of the variability in response across sites. Additional site-specific characteristics explain the remaining variability. A large runoff response was measured at the SU site due to a high percentage of moss cover and localized saturation areas from impervious granite corestones buried at the near surface. In contrasts, the dense big sagebrush of the LU site easily infiltrated any ponded water that formed during simulation runs, resulting in no measurable runoff at this site. Runoff-infiltration processes were not statistically different for two different states of an ES (i.e. CU and CU-2), however the degree of variability in response increased for CU-2 comparatively. Quantifying this range in ES hydrologic response is critical to understand rangeland watersheds and their potential for being impacted by climate and management practices.

## **Management Implications**

The ES concept is a well-established framework for partitioning rangelands into homogeneous land units based on soil, vegetation and climatic similarities for the purpose of monitoring and

assessment (Brown, 2010). Detailed quantitative datasets are needed to predict functional feedbacks among ecological site characteristics, hydrologic processes and the resilience of states and community phases and functional thresholds (Briske et al. 2008; Petersen et al. 2009; Perlinski et al. 2016; Williams et al. 2016). Rainfall simulation provides a controlled environment in which these datasets can be acquired. Integrating these datasets into evolving tools like ESDs, STMs and rangeland assessment models, such as RHEM, will improve our ability to understand and manage the complex ecohydrologic processes on rangelands.

It is important to acknowledge that improved ES mapping and detailed development of ESDs is needed, particularly in southeastern Wyoming, in order to assess these functional feedbacks on a large scale. While we have used UCCW as a test site for this study, we propose that this method can be used to characterize the hydrologic response for a range of ESs within a broader MLRA, provided that detailed mapping is available. We also stress the need for replication at the ES scale. While our plots represent subsamples of a given ES, measuring the hydrologic response of the same ES at different locations within a given MLRA would improve our ability to ascertain the characteristic hydrologic response of a given ES. With more robust tools, the management of water resources for a variety of rangeland settings while accommodating for the dynamics and uncertainty associated with stressors such as climate change and population growth can be improved.

## Acknowledgements

This research was funded by NSF (EPS-1208909), the Wyoming EPSCoR Office and the Wyoming Center for Environmental Hydrology and Geophysics (WyCEHG). We thank David Legg for helpful conversations and Andrew Annear for help with field work.

## References

- Archer, S.R., Predick, K.I., 2008. Climate change and ecosystems of the southwestern United States. *Rangelands* 30, 23-28.
- Beetle, A.A., 1956. Range survey in Wyoming's Big Horn mountains. *Wyoming Agr. Exp. Sta. Bull.* 341 (40 pp.).
- Blackburn, W.H., 1975. Factors influencing infiltration and sediment production of semiarid rangelands in Nevada. *Water Resour. Res.* 11, 929-937.
- Briske, DD, Fuhlendorf, SD, Smeins, FE, 2008. State-and-transition models, thresholds, and rangeland health: A synthesis of ecological concepts and perspectives. *Rangel. Ecol. Manag.* 58, 1–10.
- Branson, F.A., Owen, J.B., 1970. Plant cover, runoff, and sediment yield relationships on Mancos Shale in western Colorado. *Water Resour. Res.* 6, 783-790.
- Brown, J., 2010. Ecological sites: Their history, status and future. *Rangelands*. 32, 5-8.
- Burns, I.S., Guertin, D.P., Goodrich, D.C., 2010. Multi-scale calibration of KINEROS-DWEPP, a combined physically-based hydrologic model and process-based soil erosion model. 2<sup>nd</sup> Joint Federal Interagency Conference, Las Vegas. NV.
- Campbell Scientific Inc. 2011. Instruction manual: Wireless sensor network. Available at: <https://s.campbellsci.com/documents/us/manuals/wireless-sensor-network.pdf>. Accessed May, 1, 2014.
- Cerdà, A., 2001. Effects of rock fragment cover on soil infiltration, interrill runoff and erosion. *Eur. J. Soil Sci.* 52, 59-68.
- Chauvin, G.M., Flerchinger, G.N., Link, T.E., Marks, D., Winstral, A.H., Seyfried, M.S., 2011. Long-term water balance and conceptual model of a semi-arid mountainous catchment. *J. Hydrol.* 400, 133-143.
- Colberg, T.J., Romo, J.T., 2003. Clubmoss effects on plant water status and standing crop. *J. Range Manage.* 56, 489-495.
- Coupland, R.T., Johnson, R.E., 1965. Rooting characteristics of native grassland species in Saskatchewan. *J. Ecol.* 53, 475-507.
- Eldridge, D.J., Rosentreter, R., 2004. Shrub mounds enhance water flow in a shrub-steppe community in southwestern Idaho, U.S.A, in: Proceedings RMRS-P-31. USDA Forest Service, Ogden, UT, pp. 77-83.

- Flerchinger, G.N., Cooley, K.R., 2000. A ten-year water balance of a mountainous semi-arid Watershed. *J. Hydrol.* 237, 86-99.
- Frost, C.D., Frost, B.R., Chamberlain, K.R., Edwards, B.R., 1999. Petrogenesis of the 1.43 Ga Sherman batholith, SE Wyoming, USA : A reduced, rapakivi-type anorogenic granite. *J. Petrol.* 40, 1771-1802.
- Gee, G.W., Or, D., 2002. Porosity, in: Dane, J., Topp, C. (Eds.), *Methods of soil analysis: Part 4-physical methods*. Soil Science Society of America, Madison, WI, pp. 241-254.
- Hartley, H.O., 1950. The use of range in analysis of variance. *Biometrika*, 37, 271-280.
- Havstad, K., Peters, D., Allen-diaz, B., Bartolome, J., Bestelmeyer, B., Briske, D., Brown, J., Brunson, M., Herrick, J., Huntsinger, L., Johnson, P., Joyce, L., 2009. The western United States rangelands: A major resource, in: Wedin, W.F., Fales, S.L. (Eds.), *Grassland: quietness and strength for a new American agriculture*. Soil Science Society of America, Madison, WI, pp. 75-93.
- Hawkins, R.H., 1982. Interpretations of source area variability in rainfall-runoff relations, in: Singh V.P., (Ed), *Rainfall-runoff relationships*. Water Resources Publications, Littleton, CO, pp. 303-324.
- Hayes, M.M., Miller, S.N., Murphy, M.A., 2014. High-resolution landcover classification using Random Forest. *Remote Sens. Lett.* 5, 112-121.
- Hernandez, M., Nearing, M.A., Stone, J.J., Pierson, F.B., Wei, H., Spaeth, K.E., Heilman, P., Weltz, M.A., Goodrich, D.C., 2013. Application of a rangeland soil erosion model using National Resources Inventory data in southeastern Arizona. *J. Soil Water Conserv.* 68, 512-525.
- Herrick, JE, Van Zee, JW, Havstad, KM, Burkett, LM, Whitford, WG, 2005. Monitoring manual for grassland, shrubland and savanna ecosystems Vol II: Design, supplementary methods and interpretation. USDA-ARS Jornada Experimental Range, Las Cruces, New Mexico. The University of Arizona Press, Tucson, AZ.
- Kleinbaum, D.G., Kupper, L.L., Muller, K.E., 1988. *Applied regression analysis and other multivariable methods*, second ed. PWS-KENT, Boston, MA.
- Loague, K., Gander, G.A., 1990. Spatial variability of infiltration on a small rangeland catchment. *Water Resour. Res.* 26, 957-971.
- Majorowicz, A.K., 1963. Clubmoss infestation on northeastern Montana rangeland. *Proceedings of the Annual Meeting of the American Society of Range Management*. 16, 72.
- Meeuwig, R.O., 1970. Infiltration and soil erosion as influenced by vegetation and soil in northern Utah. *J. Range Manage.* 23, 185-188.

- Nearing, M.A., Wei, H., Stone, J.J., Pierson, F.B., Spaeth, K.E., Weltz, M.A., Flanagan, D.C., Hernandez, M., 2011. A rangeland hydrology and erosion model. *Trans. ASABE (Am. Soc. Agric. Bio. Eng.)* 54, 901-908.
- Newman, B.D., Wilcox, B.P., Archer, S.R., Breshears, D.D., Dahm, C.N., Duffy, C.J., McDowell, N.G., Phillips, F.M., Scanlon, B.R., Vivoni, E.R., 2006. Ecohydrology of water-limited environments: A scientific vision. *Water Resour. Res.* 42, 1-15.
- NRCS (Natural Resources Conservation Service), 2013. Ecological Site Description (ESD) System for rangeland and forestland. Available at: <https://esis.sc.egov.usda.gov/Welcome/pgESDWelcome.aspx>.
- NRCS (Natural Resources Conservation Service), 2014. Ecological Site Description System. Available at: <https://esis.sc.egov.usda.gov/Welcome/pgReportLocation.aspx?type=ESD>. Accessed March, 15, 2015.
- Osborn, H.B., Lane, L., 1969. Precipitation-runoff relations for very small semiarid rangeland watersheds. *Water Resour. Res.* 5, 419-425.
- Paige, G.B., Stone, J.J., Smith, J.R., Kennedy, J.R., 2003. The walnut gulch rainfall simulator: A computer-controlled variable intensity rainfall simulator. *Appl. Eng. Agric.* 20, 25-31.
- Paige, G.B., Stone, J.J., 1996. Measurement methods to identify and quantify the spatial variability of infiltration on rangelands, in: Proceedings of ARS Workshop, Real World Infiltration, Pingree Park, CO, July 22-25. Colorado Water Resources Research Institute, Information Series 86. pp. 109-122.
- Perlinski, A.T., Paige, G.B., Miller, S.N., Hild, A.L., 2016. Hydrologic response of four ecological sites to natural rainfall events within a semi-arid watershed. Unpublished results.
- Peterson, G., Allen, C.R., Holling, C.S., 1998. Ecological resilience, biodiversity and scale. *Ecosystems.* 1, 6-18.
- Pierson, F.B., Van Vactor, S.S., Blackburn, W.H., Wood, J.C., 1994. Incorporating small scale spatial variability into predictions of hydrologic response on sagebrush rangelands, in: Blackburn, W.H., Schuman, G.E., Pierson, F.B. (Eds.), *Variability in rangeland water erosion processes*. Soil Science Society of America, Madison, WI, pp. 23-34.
- Pierson, F.B., Spaeth, K.E., Weltz, M.A., Carlson, D.H., 2002. Hydrologic response of diverse western rangelands. *J. Range Manage.* 55, 558-570.
- Pilgrim, D.H., Chapman, T.G., Doran, D.G., 1988. Problems of rainfall-runoff modeling in arid and semiarid regions. *Hydrol. Sci. J.* 33, 379-400.

- Polley, H.W., Briske, D.D., Morgan, J. a., Wolter, K., Bailey, D.W., Brown, J.R., 2013. Climate change and North American rangelands: Trends, Projections, and Implications. *Rangeland Ecol. Manage.* 66, 493-511.
- Pyke, D.A., Herrick, J.E., Shaver, P., Pellatt, M., 2002. Rangeland health attributes and indicators for qualitative assessment. *J. Range. Manage.* 55, 584-597.
- R Development Core Team, 2014. R: a language and environment for statistical computing. Vienna, Austria: R Foundation for Statistical Computing.
- Romo, J.T., 2011. Clubmoss, precipitation, and microsite effects on emergence of graminoid and forb seedlings in the semiarid Northern Mixed Prairie of North America. *J. Arid Environ.* 75, 98-105.
- Ryel, RJ, Caldwell, MM, Leffler, AJ, Yoder, CK, 2003. Rapid soil moisture recharge to depth by roots in a stand of *Artemisia Tridentata*. *Ecology* 84, 757-764.
- SAS Institute (computer program), 2013. SAS Software version 9.4. Cary, NC, USA: SAS Institute.
- Seyfried, M.S., 1991. Infiltration patterns from simulated rainfall on a semiarid rangeland soil. *Soil Sci. Soc. Am. J.* 55, 1726-1734.
- Simanton, J.R., Rawitz, E, Shirley, E.D., 1984. Effects of rock fragments on erosion of semiarid rangeland soils, in: Kral, D.M., Hawkins, S.L. (Eds.), *Erosion and productivity of soils containing rock fragments*. Soil Science Society of America, Madison, WI, pp. 65-72.
- Simanton, J.R., Weltz, M.A., Larsen, H.D., 1991. Rangeland experiments to parameterize the water erosion prediction project model : Vegetation canopy cover effects. *J. Range Manage.* 44, 276-282.
- Sivapalan, M., 2003. Process complexity at hillslope scale, process simplicity at the watershed scale: Is there a connection? *Hydrol. Process.* 17, 1037-1041.
- Skinner, Q.D., Speck Jr, J.E., Smith, M., Adams, J.C., 1984. Stream water quality as influenced by beaver within grazing systems in Wyoming. *J. Range Manage.* 37, 142-146.
- Spaeth, K.E., Pierson, F.B., Weltz, M.A., Awang, J.B., 1996. Gradient analysis of infiltration and environmental variables as related to rangeland vegetation. *Trans. ASAE (Am. Soc. Agric. Eng.)* 39, 67-77.
- Stone, J.J., Paige, G.B., 2003. Variable rainfall intensity rainfall simulator experiments on semiarid rangelands, in: Renard, K.G., McElroy, S., Gburek, W., Canfield, E., Scott, R.L., (Eds.), *Proceedings of the 1<sup>st</sup> Interagency Conference on Research in the Watersheds*. USDA Agricultural Research Service, Washington, D.C, pp 83-88.

- Stone, J.J., Paige, G.B., Hawkins, R.H., 2008. Rainfall intensity-dependent infiltration rates on rangeland rainfall simulator plots. *Trans. ASAE (Am. Soc. Agric. Eng.)* 51, 45-53.
- Taucer, P.I., Munster, C.L., Wilcox, B.P., Owens, M.K., Mohanty, B.P., 2008. Large-scale rainfall simulation experiments on juniper rangelands. *Trans. ASABE (Am. Soc. Agric. Bio. Eng.)* 51, 1951-1961.
- Tukey, J.W., 1953 Some selected quick and easy methods of statistical analysis. *Trans. N.Y Acad. Sci.* 16, 88-97.
- Turnbull, L., Wainwright, J., Brazier, R.E., 2008. A conceptual framework for understanding semi-arid land degradation: Ecohydrological interactions across multiple-space and time scales. *Ecohydrology*. 1, 23-34.
- USDA (US Department of Agriculture). 2013. Interagency ecological site description handbook for rangelands. United States Department of Agriculture, Washington, DC, (109 pp.).
- USDA (US Department of Agriculture), Forest Service. 2013 Pole Mountain vegetation project notice of proposed action. Medicine Bow-Routt National Forests, Laramie WY Available at [http://www.fs.fed.us/nepa/nepa\\_project\\_exp.php?project=41662](http://www.fs.fed.us/nepa/nepa_project_exp.php?project=41662). Accessed January 16, 2014.
- Wilcox, B.P., Wood, M.K., Tromble, J.M., 1988. Factors influencing infiltrability of semiarid mountain slopes. *J. Range Manage.* 41, 197–206.
- Wilcox, B.P., Rawls, W.J., Brakensiek, D.L., Wight, J.R., 1990. Predicting runoff from Rangeland Catchments: A comparison of two models. *Water Resour. Res.* 26, 2401-2410.
- Wilcox, B.P., Breshears, D.D., Allen, C.D., 2003. Ecohydrology of a resource-conserving semiarid woodland: Effects of scaling and disturbance. *Ecol. Monogr.* 73, 223-239.
- Williams, C.J., Pierson, F.B., Spaeth, K.E., Brown, J.R., Al-Hamdan, O.Z., Weltz, M.A., Nearing, M.A., Herrick, J.E., Boll, J., Robichaud, P.R., Goodrich, D.C., Heilman, P., Guertin, D.P., Hernandez, M., Wei, H., Hardegree, S.P., Strand, E.K., Bates, J.D., Metz, L.J., Nichols, M.H., 2016. Incorporating hydrologic data and ecohydrologic relationships into ecological site descriptions. *Rangeland Ecol. Manage.* 69, 4-19.
- Yu, B., Rose, C.W., Coughlan, K.J., Fentie, B., 1997. Plot-scale-runoff characteristics and modeling at six sites in Australia and Southeast Asia. *Trans. ASAE (Am. Soc. Agric. Eng.)* 40, 1295-1303.

## **Chapter 3: Forward Modeling to Investigate Inversion Artifacts Resulting from Time-Lapse Electrical Resistivity Tomography during Rainfall Events**

**Abstract:** Time-lapse electrical resistivity tomography (ERT) is commonly used as a minimally invasive tool to study infiltration. Artifacts not representative of real subsurface moisture dynamics may arise during the inversion of ERT data and may be subject to misinterpretation. In 2014, we conducted field studies coupling variable intensity rainfall simulation with high-resolution electrical resistivity tomography to study the real-time partitioning of rainfall into surface and subsurface response. The significant contrast in resistivity in the subsurface from large changes in subsurface moisture resulted in artifacts during the inversion process of the time-lapse ERT data collected using a dipole-dipole electrode array. Forward modeling of the infiltration process using a two-layer system (saprolite overlain by a soil layer) was used to investigate the influence of both changes in volumetric moisture content and electrode configuration on the development of these artifacts. For the dipole-dipole array, we found that a decrease in the resistivity of the bottom layer by 67% resulted in a 50% reduction in artifact development. The seven additional array configurations tested resulted in increases in artifact development of 19% and decreases of as much as 96% compared to that of the dipole-dipole array. Moreover, these arrays varied in their ability to accurately delineate the infiltration front. Model results showed that the modified pole-dipole array was able to accurately image the infiltration zone and presented fewer artifacts for our experiments. Our study highlights the effectiveness of using forward modeling to identify the appropriate array type to collect resistivity data and obtain reliable estimates of vadose zone flow processes during rainfall-infiltration events.

**Keywords:** Electrical resistivity tomography, rainfall simulation, artifacts, infiltration, vadose zone

Carey, A.M., Paige, G.B., Carr, B.J., Dogan, M., 2016. Forward modeling to investigate inversion artifacts resulting from time-lapse electrical resistivity tomography during rainfall events. *J. Appl. Geophys.*

*Submitted to Journal of Applied Geophysics on 14 May 2016. Manuscript is currently under review.*

## Introduction

Vadose zone (VZ) characteristics are responsible for partitioning rainfall into runoff and infiltration response. Within the VZ, water movement is driven by a gradient of energy potentials controlled primarily by pore structure (Heinse and Link, 2013). Understanding the mechanisms by which the VZ partitions and controls the movement of water is critical for accurately predicting groundwater recharge dynamics, evapotranspiration, streamflow and soil water storage.

In semi-arid rangeland environments the VZ can be quite heterogeneous, due to the high spatial variability of soil, vegetation and climatic conditions. This makes quantifying VZ flow processes in these environments particularly challenging. Traditional observational platforms in VZ hydrology such as tensiometers, soil moisture probes and piezometers, are conducted at the point scale (Robinson et al., 2008; Koch et al., 2009), making it a monumental task to accurately and reliably sample the variability of these rangeland systems. Moreover, these techniques can be quite invasive and may lead to severe modification of the soil structure.

The lack of spatially dense observations of VZ processes can be addressed through the use of hydrogeophysics. Minimally invasive geophysical methods can improve the characterization and monitoring of the hydrogeology of the subsurface (Vereecken et al., 2004;

Parsekian et al., 2015); these methods provide information about the subsurface at a spatial scale much greater than traditional point scale measurements. Electrical resistivity tomography (ERT) has been widely used for decades to address hydrologic problems ranging from regional to local scales (Loke et al., 2013). ERT involves injecting an electrical current into the ground using electrodes as point sources, to establish an artificial electric potential field. The electric potential difference between two additional electrodes resulting from this field is measured and the magnitude of the injected current, in conjunction with the electrode geometry, can be used to determine the spatial distribution of the bulk resistivity averaged over a volume of the subsurface (Herman, 2001; Seidel and Lange, 2007). An inversion algorithm may then be employed to convert this apparent resistivity distribution to a “true” distribution of resistivity.

While electrical resistivity is a function of multiple parameters (mineralogy, pore structure, chemical composition of pore fluid, temperature, etc) the general tendency of decreasing resistivity with increasing water saturation makes this method appealing for measuring a variety of different hydrologic processes. ERT has been used to monitor seasonal changes in moisture content in the VZ (French and Binley, 2004; Descloitres et al., 2008; Jayawickreme et al., 2008; Pellicer et al., 2012; Mojica et al., 2013), map tracers to identify preferential flow paths (French et al., 2002; Slater et al., 2002; Koestel et al., 2008; Oberdörster et al., 2010, Robert et al., 2012) and characterize fresh water-salt water interactions (de Franco et al., 2009; Dimova et al., 2012).

In June of 2014, we conducted field studies to measure the partitioning of surface runoff and infiltration on the uplands of a semi-arid rangeland watershed in southeastern Wyoming. We used variable intensity rainfall simulation paired with high resolution time-lapse ERT on hillslope plots. Rainfall simulation provides a controlled environment in which information about

specific hydrologic processes can be isolated (Bowyer-Bower and Burth, 1989; Paige et al., 2003; Iserloh et al., 2012). Similarly, time-lapse ERT, which involves imaging changes in resistivity distributions over time, can show the dynamic effect of a particular parameter on subsurface resistivity distribution. Coupling these two techniques allows for quantification of surface runoff and detailed imaging of soil moisture movement through the VZ. Time-lapse ERT has been used frequently to monitor infiltration processes (Descloites et al., 2003; Ferré et al., 2006; Batlle-Aguilar et al., 2009; Nimmo et al., 2009; Travelletti et al., 2012; Mojica et al., 2013), but to our knowledge coupling this technique with variable intensity rainfall simulation is a novel application. While the controlled nature of this approach is appealing for studying these types of dynamics, our results show that artifacts may arise in the resistivity data during these experiments. These artifacts can lead to misinterpretation of infiltration processes.

The primary objective of this paper is to examine resistivity artifacts resulting from the inversion of time-lapse ERT data in the context of rainfall simulation and infiltration. Time-lapse ERT applications have been less studied than more traditional “one-time” applications and a number of studies have identified artifacts arising from the time-lapse inversion of resistivity data collected during the infiltration process (Batlle-Aguilar et al., 2009; Clément et al., 2009a, 2009b; Rings and Hauck, 2009). Clément et al. (2009a) used a simulated leachate injection to show that standard inversion of time-lapse data using symmetrical electrode arrays, can lead to strong artifacts showing areas of increased resistivity. Additional work by Clément et al. (2009b) suggested employing an advanced form of time-lapse inversion involving decoupling the shallow infiltration region from the rest of the profile, in order to reduce these artifacts. This method requires *a priori* information about the progression of the infiltration front which is often not available. We used a forward modeling approach informed by field observations and geologic

samples with depth, to investigate the effects of subsurface moisture condition and electrode array type on the development of artifacts during time-lapse inversion of ERT data during rainfall simulation events.

## Materials and Methods

### Study Area

Four long-term runoff plots are located in the uplands of a small ( $27 \text{ km}^2$ ), semi-arid rangeland watershed, part of the larger Upper Crow Creek watershed, southeast of Laramie, Wyoming, USA (Figure 3.1A). The  $12.2 \text{ m}^2$  plots are situated on a southern facing hillslope at an average elevation of 2547 m and slope of 11.5%. The site is characterized by deep, well-drained, coarse textured soils derived from 1.43-Ga Sherman granite batholith (Frost et al., 1999). A patchy A-horizon is present and is approximately 1 cm thick with a sandy clay texture. The B horizon is a sandy clay loam (50% sand, 26% silt and 24% clay) with an average porosity of 40%. Roughly 34% of the soil is composed of coarse fragments greater than 2 mm in diameter. This soil type is consistent across the site to depths of about 30-50 cm, at which point a weathered, saprolitic material with increased coarse fragments is reached. This subsurface structure has been confirmed using ground penetrating radar, soil pits and seismic refraction surveys. The study site is located on an alluvial fan part of the Hapjack-Rogert-Amesemont complex (Soil Survey Staff, 2013). The plant community is dominated by sandberg bluegrass (*Poa secunda* J.Presl), bluebunch wheatgrass (*Pseudoroegneria spicata* (Pursh) Á.Löve) and threetip sagebrush (*Artemisia tripartita* Rydb). In addition to bunch grasses and subshrubs, more than 30% of the soil surface is covered by a mat of lesser spikemoss (*Selaginella densa* Rydb).

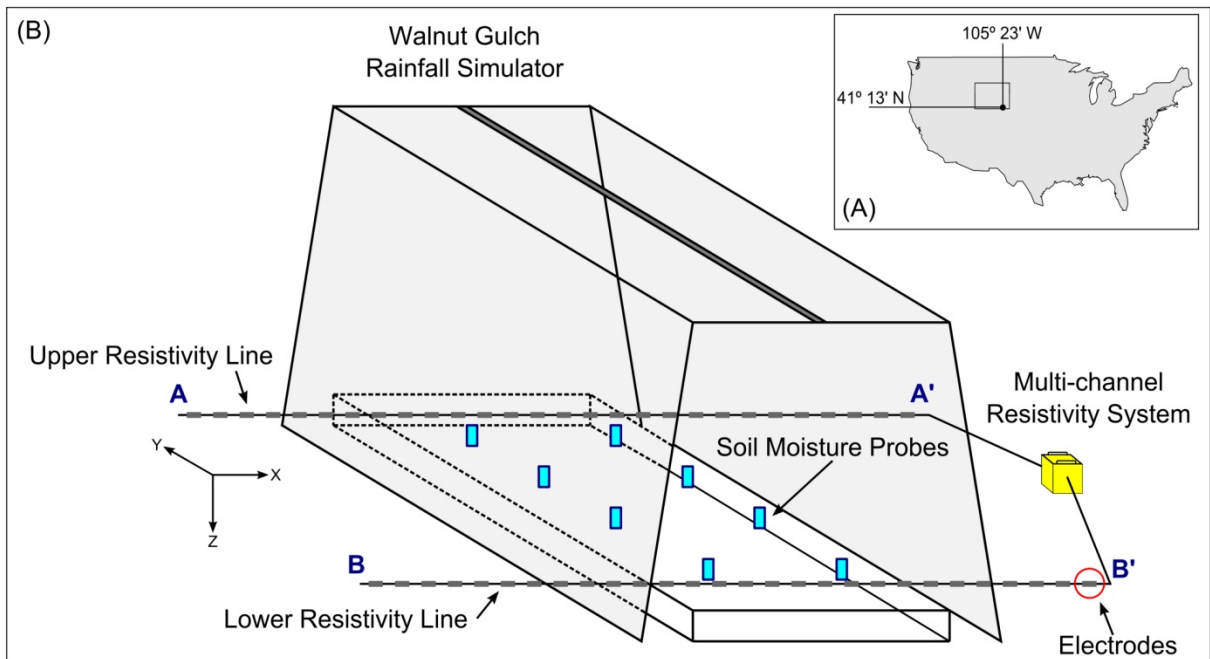


**Figure 3.1: (A) Study site location in southeast Wyoming. (B) Typical experiment setup showing the rainfall simulator positioned over the runoff plot with eight CWS655 soil moisture probes and ERT measurements made on two lines of 28 electrodes each, hooked up to a multi-channel resistivity meter.**

### *Experimental Design*

The Walnut Gulch Rainfall Simulator (Paige et al., 2003), a variable intensity computer controlled simulator, was centered directly over each plot (Fig 1B) with the four VeeJet 80100 nozzles positioned approximately 2.4 m above the soil surface and an outflow pressure of 55 kPa was maintained via an in-line pressure regulator. These target values for simulator height and outflow pressure were found by Paige et al. (2003) to achieve the desired range of rainfall intensities and distribution and a raindrop kinetic energy similar to that of natural rainfall. ERT data were collected along two profiles of 28 electrodes at 0.5 m spacing (total 13.5 m) that were placed perpendicular to the plot one meter above (lower line) and below (upper line) the plot ends (Figure 3.1B). In addition, eight CWS655 soil moisture probes (Campbell Scientific Inc., 2011) were evenly distributed across the plot to monitor near surface soil moisture response. We

performed a “dry” run in which a rainfall intensity of  $49 \text{ mm hr}^{-1}$  was applied to the plot for 45 minutes, to establish a uniform moisture condition. After allowing time for moisture redistribution, a “wet” run was performed where applied rainfall intensities were increased incrementally from 49 to  $180 \text{ mm hr}^{-1}$ . Runoff rates were measured by routing flow from the plots through a pre-calibrated flume. Resistivity datasets were collected continuously throughout the dry and wet simulations using the AGI SuperSting® R8/IP resistivity meter with a dipole-dipole (DD) array and alternating between the upper and lower lines. Average acquisition time for a dataset was seven and a half minutes in which 237 points of apparent resistivity were measured.

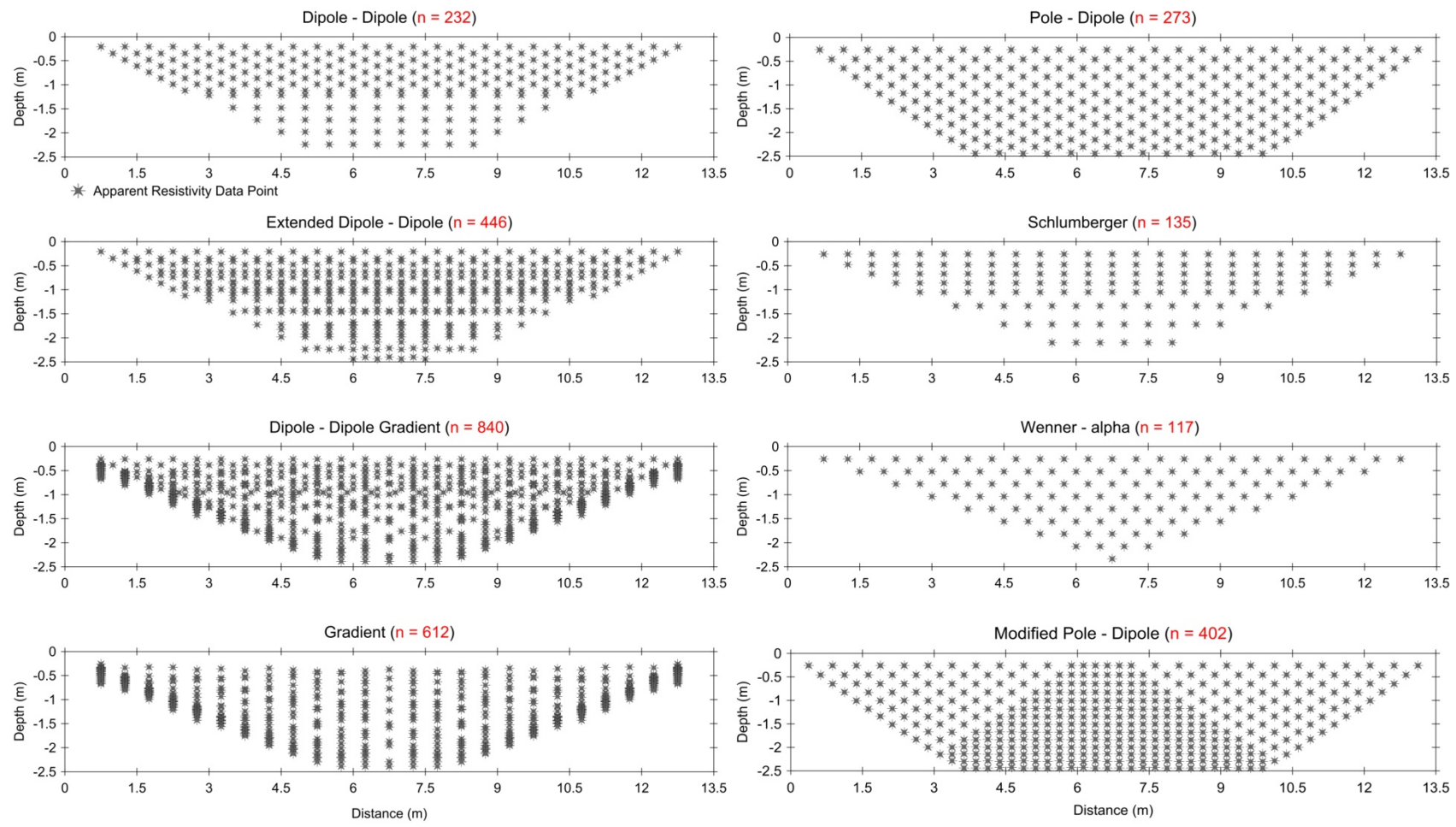


**Figure 3.2: Distribution of apparent resistivity data points for all seven arrays tested in forward modeling scenario 4 (Table 3.1) and the dipole-dipole array.**

### *Resistivity of Geologic Samples*

Geologic samples were collected from the site at approximately 10 cm intervals to a depth of 2 m by drilling boreholes using a Shaw backpack drill in conjunction with a hand auger. Retrieval of intact and undisturbed soil cores to retain *in situ* soil properties was not possible due to the cohesionless nature of the coarse material. A site-specific relationship between resistivity ( $\rho$ ) and volumetric water content ( $\theta$ ) was developed for both the sandy clay loam soil profile and the saprolite layer using an ASTM G57-06 specified soil test box (ASTM Standard G57, 2006). After oven drying the samples for 24 hours, each sample was wetted incrementally by mixing in known volumes of the same water used during rainfall simulations. Care was taken to remove excess soil to achieve a consistent volume and bulk density while packing the samples in to the test box. Resistivity values were measured for each incremental wetting. Volumetric water content and dry bulk density were calculated by weighing the box and determining the gravimetric water content from a small (20-40 g) grab sample (Kelleners et al., 2009). Covariate analysis in log scale was conducted to determine if the slopes and the y-intercepts of the curves for the two layers were statistically different (Weisberg, 2005).

Archie (1942) proposed the following equation that relates resistivity of the unsaturated zone to pore water resistivity, porosity and degree of saturation:

$$1. \frac{\theta}{\phi} = \left(\frac{\rho_s}{\rho}\right)^m$$

where  $\theta$  is the volumetric water content (%),  $\phi$  is the porosity (%),  $\rho_s$  is the bulk resistivity of a completely saturated soil sample (ohm-m) and  $m$  is a constant reflecting the material properties. This relationship is valid for medium to coarse grained soils (Frohlich and Parke, 1989). We fit

Eq. 1 for our top layer to investigate if our data allows us to use this relationship. We were not able to fit the bottom layer due to our inability to reach a saturated resistivity value.

#### *Forward Modeling and Time-Lapse Inversions*

A two layer synthetic model of the subsurface was developed for the forward modeling exercise. Using the field site profile characteristics for the model, the top layer was defined as 0-0.5 m and the bottom layer from 0.5-2 m. Four theoretical forward modeling scenarios were tested in which the resistivity of the top layer was decreased incrementally, while keeping the resistivity of the bottom layer fixed (Table 3.1). Resistivity values for both the top and the bottom layers were chosen based on the  $\rho$ - $\theta$  relationships, such that decreasing resistivity values correspond to incremental increases in volumetric water content. These scenarios represent a simplified version of the infiltration process during our rainfall simulation experiments.

Scenarios 1-3 provide insight into how time-lapse inversion results of datasets collected using a DD array vary as a function of vadose zone moisture condition. We used a DD array as it was used during the rainfall simulator experiments and DD is one of the most commonly used arrays for ERT surveys (Ward, 1990). For scenario 4, we used a series of electrode arrays to examine the role of the spatial arrangement of electrodes on the inversion results. The seven arrays tested were Extended Dipole-Dipole (E-DD), Dipole-Dipole Gradient (DD-GD), Pole-Dipole (PD), Gradient (GD), Modified Pole-Dipole (M-PD), Schlumberger (SC) and Wenner-alpha (WN). To produce the most reliable and high-resolution characterization of subsurface resistivity distribution, electrode configurations should produce a dataset with high data density and a high signal to noise ratio (Loke, 2001; Dahlin and Zhou, 2004). While the DD, PD, GD, SC and WN arrays are frequently used for resistivity imaging applications, the E-DD, DD-GD and the M-PD arrays are less common. E-DD is a modified DD array with nearly 2x the amount of apparent

resistivity data points, DD-GD is a hybrid between the GD and the DD arrays and M-PD is a variation of the PD. For the M-PD, data density is increased in the middle of the profile by maximizing the length of the current dipole and reversing the direction of data acquisition half way through the sequence to optimize the number of potential measurements for a given current injection.

**Table 3.1: Resistivity values for the four forward modeling scenarios.**

Scenario	Array Type	Resistivity Value (ohm-m)	
		Top Layer	Bottom Layer
1	Dipole-Dipole	Range <sup>†</sup>	3000
2	Dipole-Dipole	Range	2000
3	Dipole-Dipole	Range	1000
4	Multiple <sup>‡</sup>	Range	3000

<sup>†</sup> 1100, 890, 680, 460 and 250 ohm – m

<sup>‡</sup> Extended Dipole-Dipole, Dipole-Dipole Gradient, Pole-Dipole, Gradient, Modified Pole-Dipole, Schlumberger and Wenner-alpha

In each scenario, the two layer representation of the subsurface was forward modeled using a finite element method with grid cells equal to  $\frac{1}{4}$  the electrode spacing, Dirichlet boundary conditions and a Cholesky decomposition forward equation solver, to produce an apparent resistivity dataset. The density of this data set varied for the seven arrays (Figure 3.2). Datasets were created with 0% noise to represent an ideal condition and were run through a time-lapse inversion scheme using a pseudosection starting model and the normalized L2-Norm statistic for the iteration stop criteria. All forward modeling as well as the standard and time-lapse inversions were performed using EarthImager 2D® Version 2.4.0 (Advanced Geosciences, 2009). This software has been successfully applied to study hydrologic processes by a number of authors (Nyquist, 2008; Schwartz, 2008; Dimova et al., 2012; Dietrich et al., 2014). EarthImager

2D employs a time-lapse inversion algorithm that uses a base resistivity dataset as an *a priori* model and then inverts the difference between the base dataset and the monitoring datasets collected later in time (Advanced Geosciences, 2009). We used a smooth model method, also known as Occam's inversion (Constable et al., 1987) for both time-lapse and standard inversions. Occam's inversion assumes a Gaussian distribution of data errors and seeks to find the smoothest possible model that fits the data to an *a priori* Chi-squared statistic (Advanced Geosciences, 2009). While a robust inversion method is likely advantageous for delineating sharp resistivity boundaries (Loke et al., 2003), and thus the simulated infiltration occurring in the top layer under these modeling scenarios, actual infiltration processes in the field are far less symmetrical and more diffuse. It is therefore advantageous to use the same method that would be used for the inversion of real field data. All inversions presented in this paper have been clipped using an edge blanking aspect ratio of 1.0, to prevent the interpretation of areas where there is insufficient data to constrain the inversion.

## Results and Discussion

### $\rho$ - $\theta$ Relationship

The  $\rho$ - $\theta$  relationships for both layers were fit using power functions (Figure 3.3A). Standard error of the estimate for the top and bottom layer is 101 and 107 ohm-m respectively. There is a good fit for the top layer with a coefficient of determination ( $R^2$ ) of 0.94, while the fit for the bottom layer is less accurate,  $R^2$  of 0.78. Greater variability in points around the fit for the bottom layer can be attributed to increased heterogeneity of the pore space within this layer and the fact that a greater number of measurements are averaged to characterize this zone. Samples taken from this saprolitic layer are likely characterized by a more complex and variable pore size

distribution. This is in contrast to the fairly homogeneous sandy clay loam top layer. Pore size distribution plays a critical role in water movement in the subsurface. The flow of electrical current in soils is controlled by ions present in the pore water and exchangeable ions on the surface of the soil particles (Lovell et al., 1998). Resistivity (the inverse of electrical flow) is therefore expected to be more variable in a material with more complex pore size distributions. Covariate analysis in log scale shows that both the slopes and y-intercepts are statistically different ( $\alpha = 0.01$ ) (Figure 3.3B). 1

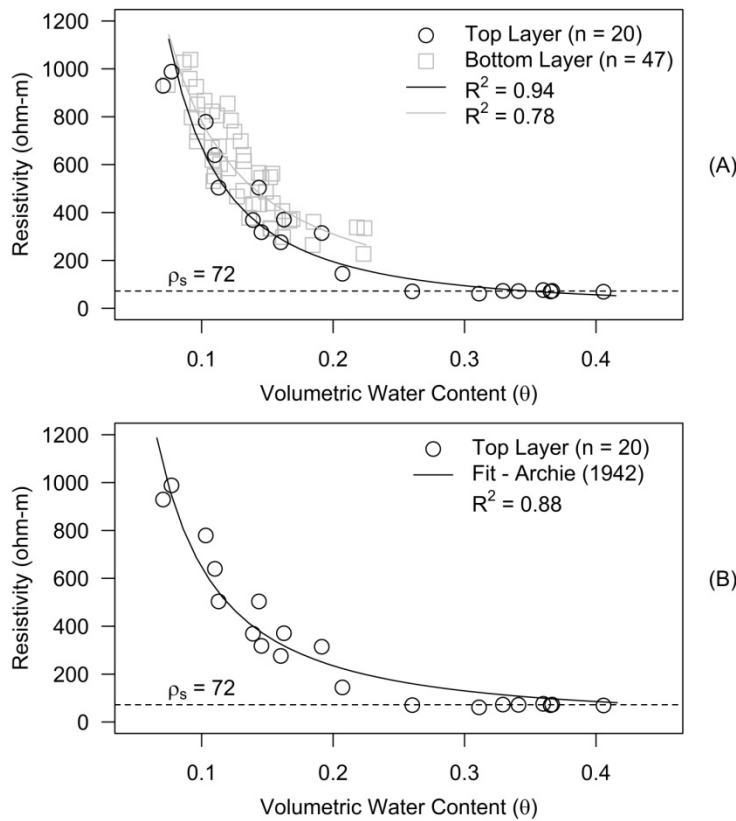


**Figure 3.3: (A) Resistivity as a function of volumetric water content for both the top and the bottom subsurface layers fitted using power functions. (B) Resistivity-volumetric water content data from the top layer fitted using Eq. 1.**

For the top layer, a saturated resistivity value ( $\rho_s$ ) of 72 ohm-m was reached at approximately 32% volumetric water content (Figure 3.3A and 3.3C). This is quite a bit lower than the 40% total porosity measured for this layer using the undisturbed soil core method. The technique of packing soil material into a soil test box for resistivity measurements, unavoidably results in an artificial pore size distribution, which may lead to an underestimated saturation level. However, soil moisture probes distributed across the plots during rainfall simulation experiments suggest that complete saturation does not occur and that field saturated water content is approximately 33.6 % (standard error = 0.3%). It is therefore reasonable to assume that this value more closely represents field saturation conditions. Eq. 1 did well in predicting our observed data for the top layer ( $R^2 = 0.88$ ) and the material constant was found to be 1.46.

#### *Field Data Examples*

For our rainfall simulator datasets, resistivity artifacts in the time-lapse inversions commonly formed under three different conditions: (1) at the very beginning of a dry simulator run, (2) differencing profiles that exhibit different applied rainfall intensities during a wet run and (3) time-lapse inversions of non-sequential profiles (i.e. greater than two times the average profile acquisition time has elapsed). Each of these conditions is characterized by large changes (increases) in moisture content and therefore resistivity, between the top and bottom layers of the profile. This proves to be problematic and plays an important role in the development of inversion artifacts.

Four resistivity profiles collected over the course of 35 minutes during a dry simulator run are shown in Figure 3.4. A background profile was collected prior to the start of rainfall and three profiles were collected during a 60 minute rainfall application at  $49 \text{ mm hr}^{-1}$ . These datasets are from the lower resistivity profile (B-B' in Figure 3.1B) of one of the four plots at the site. A

total of 28.6 mm of water infiltrated over this time period. As the simulation progresses, apparent resistivity values (Figure 3.4A) directly beneath the rainfall simulator decrease in reference to the background profile. This is due to water infiltrating into the vadose zone. At the same location deeper in the profile, apparent resistivity increases through time. This phenomenon is counter intuitive considering the only change is the addition of moisture into the profile. Values near the peripheral of the profile remain consistent through time suggesting that these regions are not influenced by the dynamics occurring in the middle. As previously mentioned, datasets of apparent resistivity must be inverted in to produce a distribution of true resistivity in the subsurface. Figure 3.4B shows the inversion results for each profile. The same general trend can be seen over time, resistivity in the middle of the profile is decreasing at the near surface and increasing deeper in the profile. Changes in resistivity can be converted into a more meaningful parameter such as water content, through the use of the relationship in Figure 3.3A (Figure 3.4C).

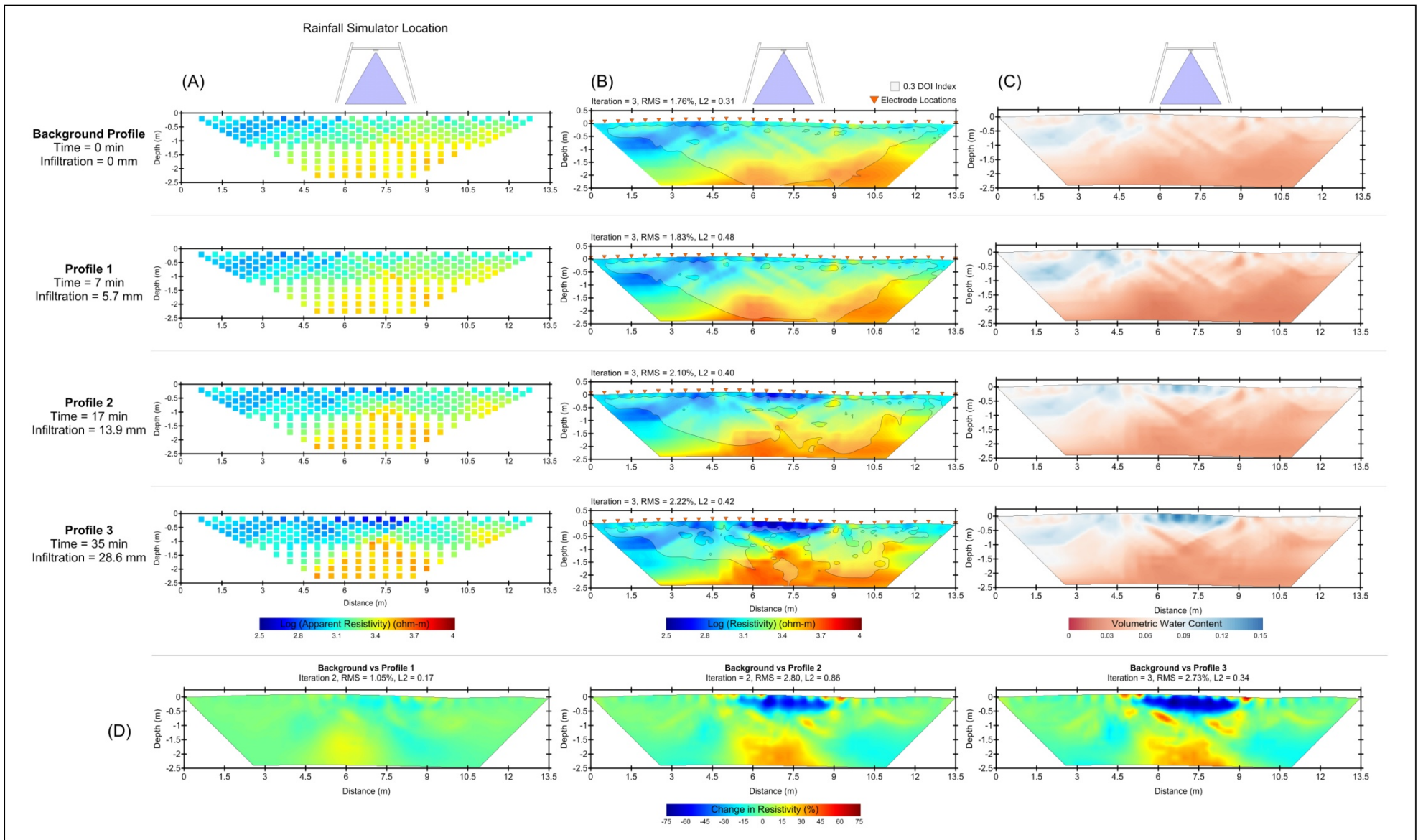


**Figure 3.4:** Four resistivity profiles collected during the dry run of one of the four rainfall simulation experiments performed at the site. A background profile was collected prior to rainfall and three additional profiles were sequentially collected under a rainfall application rate of  $49 \text{ mm hr}^{-1}$ . (A) Log of the measured apparent resistivity at different locations in the subsurface. (B) Standard inversion results (in log of resistivity) for the four profiles. A DOI contour (Oldenburg and Li, 1999) of 0.3 is overlaid and indicates regions of high credibility. Iteration, RMS and L2 values describe the inversion quality. (C) Resistivity transformed into water content space. (D) Time-lapse inversion results showing percent change in resistivity. The background profile was used as the base dataset for the inversion.

A shaded region is overlain on each inverted profile representing the depth of investigation (DOI) contour as outlined by Oldenburg and Li (1999). Oldenburg and Li (1999) developed a method using synthetic datasets that involved varying the value of the half space starting model during the inversion process and monitoring the change in the inversion result. A DOI value close to zero represents regions that converge to the same answer regardless of the value of the starting half space model. High credibility should be assigned to these areas. Higher values represent areas in which the data do not constrain the inversion and as a result should be assigned less credibility. It was suggested by Oldenburg and Li (1999) that “a reasonably cautious value might be 0.1 or 0.2.” Here we chose to show the 0.3 DOI contour due to the fact that we are working with field data susceptible to noise. We assign greater credibility to the portions of the inverted profile that are within this shaded region.

For all inverted profiles, the DOI contour does not include the very near surface (approximately the first 0.2 m) due to the poor data resolution of this region. In practice however, we use the apparent resistivity pseudosection as the starting model for our inversions. This solves the near surface resolution problem because at this depth the apparent resistivity is closest to matching the actual resistivity (Nyquist et al., 2007). The DOI contour also omits the sides and the very bottom of the profiles. As the rainfall simulation progresses the extent of this contour decreases and becomes quite patchy. By the fourth profile, collected 35 min after the beginning of rainfall, the region directly beneath the infiltration zone is no longer encapsulated by the contour. Credibility assigned to this area is severely diminished. This is likely due to the fact that the assumption in which all measurements are being made with a constant current density is being violated and current is preferentially moving through the infiltrated zone during the ERT measurements. As the infiltrated region grows throughout the simulation, less current

makes its way deeper through the profile resulting in our inability to resolve the true resistivity distribution at these depths.

The effect of increasing apparent resistivity values and decreasing credibility of the inversion underneath the infiltrated zone can be seen in the time-lapse inversions (Figure 3.4D). These images are created by differencing each of the three profiles collected during rainfall simulation from the background image. A negative percent change from background condition (shown as a blue region) represents real infiltration processes while a positive percent change (shown as a yellow-red region) is interpreted as an inversion artifact. These artifacts can be quite substantial indicating as much as a 72 % increase in resistivity from the background condition. Under this controlled experiment, we are able to identify these as true artifacts, however in other contexts these can be wrongly interpreted as areas of drainage or evaporation processes. It is important to note that additional inversions (not presented in this paper) were conducted using R2 version 3.0 inversion software (Binley and Kemna, 2005), in which these artifacts persisted and the trend of poorly constrained data beneath the infiltrated zone was also observed. This suggests that artifact development is likely inherent to the raw resistivity data as opposed to a product of the inversion software.

#### *Forward Modeling-Dipole-Dipole*

Forward modeling results of the simplified infiltration process using the DD array (scenarios 1-3, Table 3.1) demonstrate the influence of moisture condition on the development of these time-lapse inversion artifacts (Figure 3.5). All forward modeling results are presented as images created from the time-lapse inversion of two profiles with the same (i.e. constant) bottom layer resistivity value and top layer values of 1100 ohm-m and 250 ohm-m (representing a large infiltration flux in the top layer). In scenario 1, a resistivity of 3000 ohm-m was assigned to the

bottom layer. This represents infiltration occurring over a fairly dry zone, similar to the dynamics of the field data in Figure 3.4D. Just like the field data example, we would expect to see negative percent change in the top layer due to infiltration processes and a zero percent change in the bottom layer where the resistivity is being held constant through time. Instead, our results show significant inversion artifacts in which resistivity is increasing with a maximum resistivity change ( $\Delta\rho_{\max}$ ) of +185%. If the assigned resistivity value of the bottom layer is decreased from 3000 to 1000 ohm-m, the contrast in moisture condition between the infiltrated region and the bottom layer dissipates. When a more uniformly wetted condition is reached, the magnitude and extent of the inversion artifacts decrease. For scenarios 2 and 3  $\Delta\rho_{\max}$  decreases to +124% and +80%, respectively. When the resistivity of the bottom layer is reduced by 67% (scenario 3), inversion artifacts are preferentially formed on the edges of the profile, with significant reduction in the artifacts in the center. It can also be seen that the delineation of the infiltration zone more accurately represents the true delineation defined in the synthetic model (i.e. 0.5 m depth) (Figure 3.5).

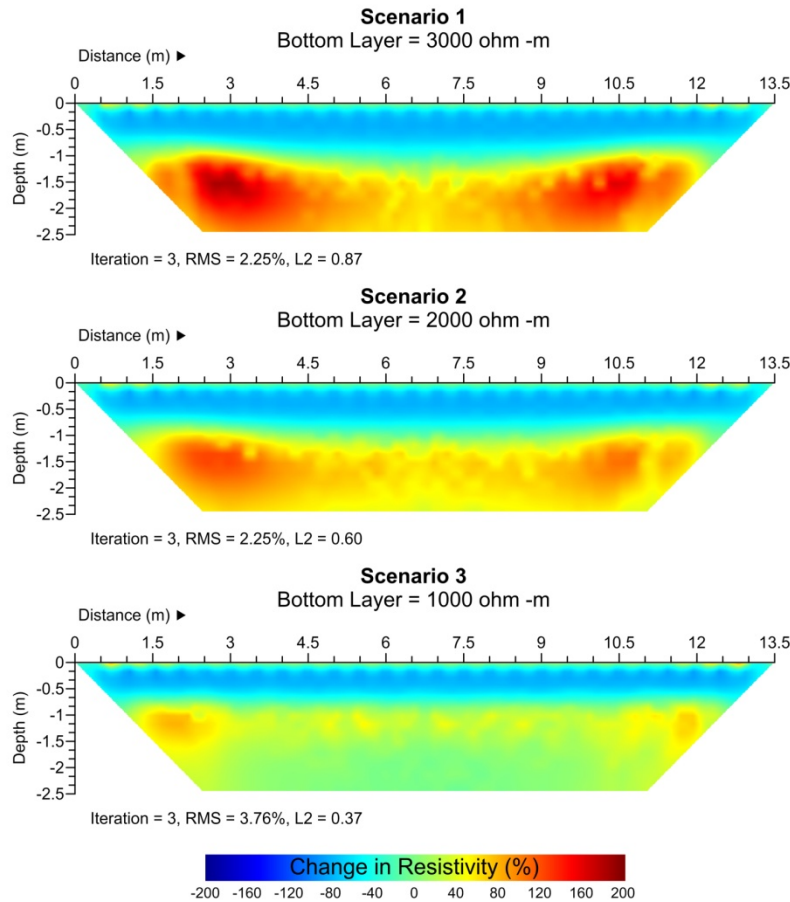


**Figure 3.5:** Time-lapse inversion results for the three different modeling scenarios outlined in Table 3.1 using a dipole-dipole array. Time-lapse inversion was done by differencing two profiles with the same resistivity value for the bottom layer and top layer values of 1100 ohm-m and 250 ohm-m.

#### *Forward Modeling-Multiple Arrays*

Time-lapse inversion images produced under scenario 4 demonstrate the effect of the seven different array types on the inversion product under an infiltration scenario (Figure 3.6). Results using the DD array (scenario 1, Figure 3.5) are shown for comparison. For these images the resistivity of the bottom layer was fixed at 3000 ohm-m. Due to the fact that moisture contrast between the layers exacerbates the inversion artifacts, only the forward modeling results

under this dry condition are presented. As in Figure 3.5, the infiltrated zone is indicated by the light blue negative percent change region while the yellow-red regions represent inversion artifacts. Statistics related to the artifact development were calculated for each array (Table 3.2). It is important to note that all of the arrays tested resulted in an over estimation of the infiltrated zone, extending beyond the assigned depth of 0.5 m. This is likely due to the fact that the inversion algorithm employs a smoothing constraint as part of the regularization method to ensure that a solution is reached (Binley and Kemna, 2005).

**Table 3.2: Average, median and maximum artifact values presented as percent changes in resistivity ( $\Delta\varrho$ ). Any region of the time-lapse profile with a percent change greater than zero was considered to be an artifact. A coefficient of variation (CV) for the artifacts was calculated.**

Array Type	$\Delta\varrho_{\text{avg}} (\%)$	$\Delta\varrho_{\text{med}} (\%)$	$\Delta\varrho_{\text{max}} (\%)$	CV (%)
Dipole - Dipole	64.5	64.8	185.0	66.6
Extended Dipole - Dipole	71.8	72.3	220.6	70.9
Dipole – Dipole Gradient	40.3	34.3	141.8	67.8
Pole- Dipole	35.5	23.1	104.0	86.8
Gradient	16.8	14.5	47.0	69.3
Modified Pole - Dipole	10.0	9.9	24.7	57.6
Schlumberger	5.8	4.4	15.3	76.7
Wenner	2.8	2.5	7.6	73.2

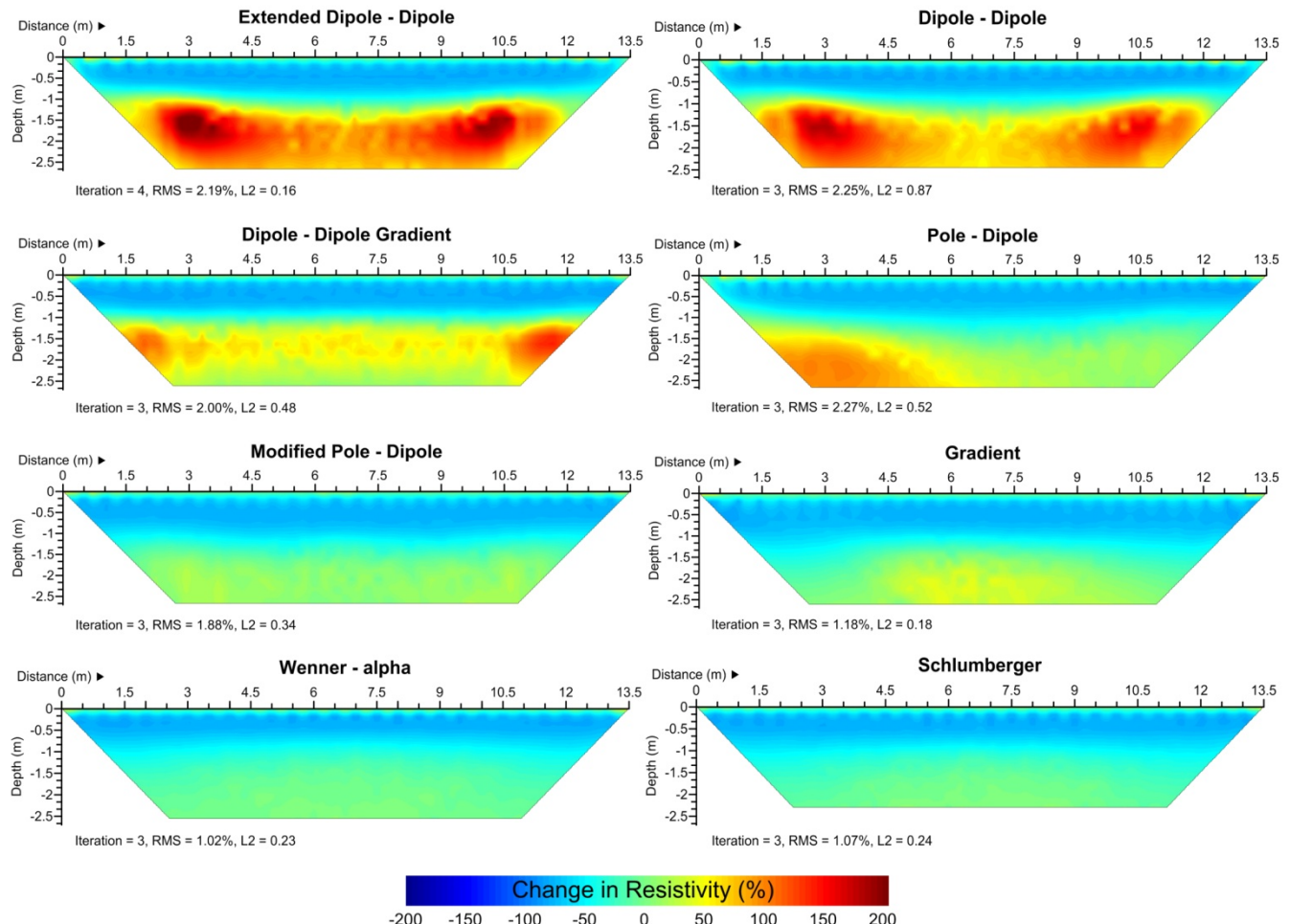


**Figure 3.6: Time-lapse inversion results for scenario 4 outlined in Table 3.1. The seven different array configurations are shown with dipole-dipole included for comparison. Time-lapse inversion was done by differencing two profiles with the same resistivity value for the bottom layer and top layer values of 1100 ohm-m and 250 ohm-m.**

In general, the E-DD, DD and the DD-GD arrays do well in delineating the infiltration zone. Horizontal variability in the boundary of the zone for DD and E-DD can be attributed to the fact that these arrays are more sensitive to lateral variations in resistivity (i.e. identifying vertical structures) than vertical contrasts (horizontal layering). The maximum and average artifact values were the greatest for these two arrays (Table 3.2). These large artifact values could be a result of using the dipole-dipole measurement scheme, in which the potential dipoles are situated outside of the in-line current dipole. This electrode configuration inherently leads to smaller generated electric potential field gradients during ERT measurements. In addition,

increased spacing between the current and the potential dipoles must be achieved in order to sample deeper into the subsurface, causing the magnitude of the potential measurements to decrease with depth. For this modeling exercise measured potentials near the surface of the profile were over 40 times larger than those near the bottom. This large contrast is difficult for the inversion software to resolve, resulting in the large artifact at the bottom of the profile. These regions also appear to preferentially form towards the bottom edges of the profile where data density is quite low. It can be seen that the E-DD results are an intensified version of the DD array. More intense artifacts at the bottom edges results in a higher coefficient of variation (CV) for E-DD compared to DD (Table 3.2). E-DD has 446 data points while the DD has 232, meaning that the E-DD has a greater number of low potential data points to fit during the inversion process. The DD-GD array uses both dipole-dipole and gradient measurements. Gradient measurements place a series of potential dipoles inside the in-line current dipole. This configuration leads to stronger generated electric potential fields and therefore larger potential values. The average and maximum artifact values are reduced to 40.3 % and 141.8%, respectively, however they are still quite large. Extent of the artifacts is reduced compared to E-DD and DD.

WN, SC and GD arrays show substantial reductions in the presence of inversion artifacts. WN and SC are single channel arrays that make only one potential measurement at the midpoint of the current dipole for each current injection. This results in consistently high measured potential values throughout the profile. For example, the potentials near the surface of the WN array are only about twice as large as those at the bottom. The lack of a high gradient in measured potentials with depth leads to virtually no artifact development in the results. WN has a  $\Delta\rho_{\max}$  of +7.6% and SC a  $\Delta\rho_{\max}$  of +15.3%. Using multiple potential dipoles within the current

dipole gives the GD array increased data density while at the same time more potential measurements of lower magnitude, resulting in a  $\Delta\rho_{\max}$  of +47%. For all three arrays the delineation of the infiltrated zone, particularly at the edges of the image is quite poor. These arrays suffer from poor spatial resolution and tend to produce a more diffuse image. PD and M-PD represent a compromise between accurately delineating the infiltrated zone and reducing inversion artifacts. These arrays use a current dipole with one of the poles typically placed a distance of five times the length of the array (termed the “infinity electrode”) from the potential dipoles. For this exercise, the infinity electrode was placed to the left of the image. The PD array progresses in a reverse fashion, meaning that the current dipole is slightly smaller for data collected at the left of the profile compared to that of the right. The resulting artifact is biased towards the infinity electrode with a  $\Delta\rho_{\max}$  of +104%. The artifact CV for PD is the largest of all the arrays due to this bias (Table 3.2). For the M-PD, the array switches from forward to reverse halfway across the array and provides greater data density in the middle of the profile (Figure 3.2). This minimizes the artifact seen for the PD and reduces the  $\Delta\rho_{\max}$  to +25%. This also results in the lowest artifact CV of all the arrays.

In addition to assessing these arrays based on delineation of the infiltrated zone and ability to minimize inversion artifacts, factors such as data density and acquisition time must be considered when assessing their merits/shortcomings for imaging the evolution of infiltration plumes through time. To monitor transient hydrologic processes, the optimal approach will include arrays that result in dense distributions of data measured at the finest temporal scale possible (Furman et al., 2003). In general, an increased number of data points will result in improved spatial resolution and a more accurate representation of the subsurface resistivity distribution. WN and SC are not suitable for measuring in more than one channel and make only

one potential measurement for every current injection. This limits the data density that can be achieved with these arrays and increases the data acquisition time. For example under our modeling scenario the WN array measures 117 data points in approximately 18.3 minutes. The DD array, which can use multiple channels, measures 232 points in approximately 7 minutes. At a site such as ours, characterized by well-drained coarse textured soils, infiltration processes occur at a very rapid rate and the difference between 7 and 18.3 minutes is substantial. It is important to note that these times are based on estimates using the AGI SuperSting® R8/IP resistivity meter. Data acquisition time will vary based on input parameters and the hardware capacity of specific meters.

Our results indicate that the M-PD array provides the best overall trade-off of these factors. Acquisition time is approximately 12.2 minutes in which 402 data points are collected. It has minimal inversion artifacts and does a fair job at delineating the infiltration zone. This array has the potential to provide quality inversion results and has been noted by others as a good compromise between resolution and signal strength (Dahlin and Zhou, 2004; Okpoli, 2013). The main disadvantage of this array configuration is that the infinity electrode must be placed far from the electrode array (usually a distance five times the length of the array) limiting these surveys to accessible sites or a small electrode spacing.

## Conclusion

This study used a forward modeling approach to examine the role of moisture content and electrode array geometry on the development of resistivity artifacts resulting from the algorithm used for time-lapse inversion of ERT data. Time-lapse ERT is advantageous for monitoring vadose zone flow processes because when combined with  $\rho-\theta$  relationships, it allows for the dynamic effect of a particular parameter, such as water content, on resistivity distribution to be

monitored. In our subsurface system, the high contrast in resistivity between the top soil layer under infiltration processes and the dry saprolitic region beneath, leads to areas of increased resistivity when performing time-lapse inversions. Our rainfall simulation experiment provides a controlled system in which we can appropriately identify these areas artifacts, not representative of true infiltration processes. Under natural conditions these regions may be subject to misinterpretation. Identifying the appropriate array type to image these processes is therefore critical in order to make the most accurate assessment.

Our results show that as the contrast in moisture content between the top and bottom layer decreases (as indicated by decreasing resistivity) these anomalous regions dissipate. Furthermore, we show that certain array geometries are better suited for imaging these vadose zone dynamics. For instance the DD array is prone to producing artifacts while the WN array fails to accurately delineate the infiltration zone. A different array should be used at least during initial infiltration when moisture contrast is significant. We suggest the M-PD due to its ability to accurately image the infiltration zone, present fewer artifacts and provide more data in a short amount of time. Factors specific to field conditions not discussed in this paper such as contact resistance of the electrodes, temperature variations and noise contamination, will also play a role in the ability to effectively image these processes and must also be considered. These forward modeling results are critical for identifying the appropriate method to collect resistivity datasets during large infiltration experiments, to obtain proper subsurface images and ultimately reliable estimates of subsurface flow processes during these events.

### **Acknowledgements**

This work was supported by the National Science Foundation [EPS-1208909, 2012]. We thank A. Parsekian and D. Legg for helpful conversations and K. Hyde for field work support.

## References

- Advanced Geosciences. 2009. EarthImager 2D, resistivity and IP inversion software, version 2.4.0. Instruction manual. Advanced Geosciences, Austin, TX. 139 p.
- Archie, G.E. 1942. The electrical resistivity log as an aid in determining some reservoir characteristics. *Trans. Am. Inst. Min. Metal. Pet. Eng.* 146:54-62.
- Batlle-Aguilar, J., S. Schneider, M. Pessel, P. Tucholka, Y. Coquet, and P. Vachier. 2009. Axisymmetrical infiltration in soil imaged by noninvasive electrical resistivimetry. *Soil Sci. Soc. Am. J.* 73:510-520, doi:10.2136/sssaj2007.0278.
- Bowyer-Bower, T.A.S., and T.P. Burt. 1989. Rainfall simulators for investigating soil response to rainfall. *Soil Technol.* 2:1-16.
- Binley A. and Kemna A. 2005. DC resistivity and induced polarization methods. p. 192-156. In Y. Rubin and S.S. Hubbard (eds.) *Hydrogeophysics*. Water Sci. Technol. Libr., vol. 50. Springer, New York.
- Clément, R., M. Descoïtres, T. Günther, and L. Oxarango. 2009a. Comparison of three arrays in time-lapse ERT: Simulation of a leachate injection experiment. *ArchéoSciences*. 33:275-278.
- Clément, R., M. Descloitres, T. Günther, O. Ribolzi, and A. Legchenko. 2009b. Influence of shallow infiltration on time-lapse ERT: Experience of advanced interpretation. *C.R. Geosciences*. 341:886-898, doi:10.1016/j.crte.2009.07.005.
- Constable, S.C., R.L. Parker, and C.G. Constable. 1987. Occam's inversion: A practical algorithm for generating smooth models from electromagnetic sounding data. *Geophysics*. 52:289-300.
- Dahlin, T., and B. Zhou. 2004. A numerical comparison of 2D resistivity imaging with 10 electrode arrays. *Geophys. Prospect.* 52:379-398.
- de Franco, R., G. Biella, L. Tosi, P. Teatini, A. Lozej, B. Chiozzotto, M. Giada, F. Rizzetto, C. Claude, A. Mayer, V. Bassan, and G. Gasparetto-Stori. 2009. Monitoring the saltwater intrusion by time lapse electrical resistivity tomography. *J. Appl. Geophys.* 69: 117-130, doi:10.1016/j.jappgeo.2009.08.004.
- Descloitres, M., O. Ribolzi, and Y. Le Troguer. 2003. Study of infiltration in a Sahelian gully erosion area using time-lapse resistivity mapping. *CATENA*. 53:229-253, doi:10.1016/S0341-8162(03)00038-9.

Descloites, M., R. Laurent, M. Sekhar, A. Legchenko, J.J. Braun, M.S. Mohan Kumar, and S. Subramanian. 2008. Characterization of seasonal local recharge using electrical resistivity tomography and magnetic resonance sounding. *Hydrol. Process.* 22:384-394, doi:10.1002/hyp.6608.

Dietrich, S., P.A. Weinzettel, and M. Varni. 2014. Infiltration and drainage analysis in a heterogeneous soil by electrical resistivity tomography. *Soil Sci. Soc. Am. J.* 78:1153-1167, doi:10.2136/sssaj2014.02.0062.

Dimova, N.T., P.W. Swarzenski, H. Dulaiova, and C.R. Glenn. 2012. Utilizing multichannel electrical resistivity methods to examine the dynamics of the fresh water-seawater interface in two Hawaiian groundwater systems. *J. Geophys. Res.* 117:C02012, doi:10.1029/2011JC007509.

Ferré, T.P., A.C. Hinnell, and J.B. Blainey. 2006. Inferring hydraulic properties using surface-based electrical resistivity during infiltration. *Leading Edge*. 25:720-723, doi:10.1190/1.2210055.

French, H. K., C. Hardbattle, A. Binley, P. Winship, and L. Jakobsen. 2002. Monitoring snowmelt induced unsaturated flow and transport using electrical resistivity tomography. *J. Hydrol.* 267:273-284.

French, H., and A. Binley. 2004. Snowmelt infiltration: monitoring temporal and spatial variability using time-lapse electrical resistivity. *J. Hydrol.* 297:174-186, doi:10.1016/j.jhydrol.2004.04.005.

Frohlich, R.K., and C.D. Parke. 1989. The electrical resistivity of the vadose zone – field survey. *Ground Water*. 27:524-530.

Frost, C.D., B.R. Frost, K.R. Chamberlain, and B.R. Edwards. 1999. Petrogenesis of the 1.43 Ga Sherman batholith, SE Wyoming, USA: A reduced rapakivi-type anorogenic granite. *J. Petrology*. 40:1771-1802.

Furman, A., T.P.A. Ferré, A.W. Warrick. 2003. A sensitivity analysis of electrical resistivity tomography array types using analytical element modeling. *Vadose Zone J.* 2:416-423, doi:10.2113/2.3.416.

Heinse, R., and T.E. Link. 2013. Vadose zone processes: A compendium for teaching interdisciplinary modeling. *J. Contemp. Water Res. and Educ.* 152: 22 – 31.

Herman, R. 2001. An introduction to electrical resistivity in geophysics. *Am. J. Phys.* 69:943-952, doi:10.1119/1.1378013.

Husman, J.A., W. Bouten, and T.P. Ferré. 2004. Bridging the gap between geophysical measurements and hydrological modeling. American Geophysical Union, Fall Meeting 2004, abstract #H14C-01.

- Iserloh, T., W. Fister, M. Seeger, H. Willger, and J.B. Riles. 2012. A small portable rainfall simulator for reproducible experiments on soil erosion. *Soil Till. Res.* 124:131-137, doi:10.1016/j.still.2012.05.016.
- Jayawickreme, D.H., R.L. Van Dam, and D.W. Hyndman. 2008. Subsurface imaging of vegetation, climate, and root zone moisture interactions. *Geophys. Res. Lett.* 35:L18404, doi:10.1029/2008GL034690.
- Kelleners, T.J., G.B. Paige, and S.T. Gray. 2009. Measurement of the dielectric properties of Wyoming soils using electromagnetic sensors. *Soil Sci. Soc. Am. J.* 73:1626-1637, doi:10.2136/sssaj2008.0361.
- Koestel, J., A. Kemna, M. Javaux, A. Binley, and H. Vereecken. 2008. Quantitative imaging of solute transport in an unsaturated and undisturbed soil monolith with 3-D ERT and TDR. *Water Resour. Res.*, 44:W12411, doi:10.1029/2007WR006755.
- Koch, K., J. Wenninger, S. Uhlenbrook, and M. Bonell. 2009. Joint interpretation of hydrological and geophysical data: electrical resistivity tomography results from a process hydrological research site in the Black Forest Mountains, Germany. *Hydrol. Process.* 23:1501-1513, doi:10.1002/hyp.7275.
- Loke, M.H. 2001. Electrical imaging surveys for environmental and engineering studies: a practical guide to 2-D and 3-D surveys. p. 62. Available at [www.geoelectrical.com](http://www.geoelectrical.com).
- Loke, M.H., I. Acworth, T. Dahlin. 2003. A comparison of smooth and blocky inversion methods in 2D electrical imaging surveys. *Explor. Geophys.* 34:182-187.
- Loke, M.H., J.E. Chambers, D.F. Rucker, O. Kuras, and P.B. Wilkinson. 2013. Recent developments in the direct-current geoelectrical imaging method. *J. Appl. Geophys.* 93:135-156, doi:10.1016/j.jappgeo.2013.02.017.
- Lovell, M.A., P. D. Jackson, P. K. Harvey, C.G. Williams, R.C. Flint, G. Williamson, and D.A. Gunn. 1998. Electrical resistivity measurements on unconsolidated core. p. 10. In Society of Core Analysts (SCA 98). The Hague, Netherlands.
- Mojica, A., I. Díaz, C.A. Ho, F. Ogden, R. Pinzón, J. Fábrega, D. Vega, and J. Hendrickx. 2013. Study of seasonal rainfall infiltration via time-lapse surface electrical resistivity tomography: Case study of Gamboa Area, Panama Canal Watershed. *Air, Soil and Water Res.* 6:131-139, doi:10.4137/ASWR.S12306.
- Nyquist, J.E., J.S. Peake, and M.J.S. Roth. 2007. Comparison of an optimized resistivity array with dipole-dipole soundings in karst terrain. *Geophysics*. 72:139-144, doi:10.1190/1.2732994.

- Nyquist, J.E., P.A. Freyer, and L. Toran. 2008. Stream bottom resistivity tomography to map ground water discharge. *Ground Water*. 46:561-569, doi:10.1111/j.1745-6584.2008.00432.x.
- Nimmo, J.R., K.S. Perkins, K.M. Schmidt, D.M. Miller, J.D. Stock, and K. Singha. 2009. Hydrologic characterization of desert soils with varying degrees of pedogenesis: 1. field experiments evaluating plant-relevant soil water behavior. *Vadose Zone J.* 8:840-845, doi:10.2136/vzj2008.0052.
- Oberdörster, C., J. Vanderborght, A. Kemna, and H. Vereecken. 2010. Investigating preferential flow processes in a forest soil using time domain reflectometry and electrical resistivity tomography. *Vadose Zone J.* 9:350-361, doi:10.2136/vzj2009.0073.
- Okpoli, C.C. 2013. Sensitivity and resolution capacity of electrode configurations. 2013:1-12. doi:[10.1155/2013/608037](https://doi.org/10.1155/2013/608037).
- Oldenburg, D.W., and Y. Li. 1999. Estimating depth of investigation in dc resistivity and IP surveys. *Geophysics*. 64:403-416, doi: 10.1190/1.1444545.
- Parsekian, A.D., K. Singha, B.J. Minsley, W.S. Holbrook, and L. Slater. 2014. Multiscale geophysical imaging of the critical zone. *Rev. Geophys.* 53:1-26, doi:10.1002/2014RG000465.
- Paige, G.B., J.J. Stone, J.R. Smith, and J.R. Kennedy. 2003. The walnut gulch rainfall simulator: a computer-controlled variable intensity rainfall simulator. *Appl. Eng. Agric.* 20:25-31.
- Pellicer, X.M., M. Zarroca, and P. Gibson. 2012. Time-lapse resistivity analysis of quaternary sediments in the midlands of Ireland. *J. Appl. Geophys.* 82:46-58, doi:10.1016/j.jappgeo.2012.02.009.
- Pierson, F.B., K.E. Spaeth, M.A. Weltz, and D.H. Carlson. 2002. Hydrologic response of diverse western rangelands. *J. Range. Manage.* 55:558-570, doi:10.2307/4003999.
- Rings, J., C. Hauck. 2009. Reliability of resistivity quantification for shallow subsurface water processes. *J. Appl. Geophys.* 68:404-416, doi:10.1016/j.jappgeo.2009.03.008.
- Robert, T., D. Caterina, J. Deceuster, O. Kaufmann, and F. Nguyen. 2012. A salt tracer test monitored with surface ERT to detect preferential flow and transport paths in fractured/karstified limestones. *Geophysics*. 77:B55-B67, doi:10.1190/geo2011-0313.1.
- Robinson, D.A., A. Binley, N. Cook, F.D. Day-Lewis, T. P.A. Ferré, V.J.S. Grauch, R. Knight, M. Knoll, V. Lakshmi, R. Miller, J. Nyquist, L. Pellerin, K. Singha, and L. Slater. 2008. Advancing process-based watershed hydrological research using near-surface geophysics: A vision for, and review of, electrical and magnetic geophysical methods. *Hydrol. Process.* 22:3604-3635, doi:10.1002/hyp.6963.

- Schwartz, B.F., M.E. Schreiber, and T. Yan. 2008. Quantifying field-scale soil moisture using electrical resistivity imaging. *J. Hydrol.* 362:234-246, doi:10.1016/j.jhydrol.2008.08.027.
- Seidel, K., and G. Lange. 2007. Direct current resistivity methods. p. 205-237. *In* K. Knödel et al. (eds.) *Environmental geology: Handbook of field methods and case studies*. Springer, Berlin, Germany, doi:10.1007/978-3-540-74671-3.
- Slater, L., A. Binley, R. Versteeg, G. Cassiani, R. Birken, and S. Sandbery. 2002. A 3D ERT study of solute transport in a large experimental tank. *J. Appl. Geophys.* 49:211-229, doi:10.1016/S0926-9851(02)00124-6.
- Soil Survey Staff, Natural Resources Conservation Service, United States Department of Agriculture. 2013. Web Soil Survey. Available online at <http://websoilsurvey.nrcs.usda.gov/>. Accessed [03/11/2015].
- Travelletti, J., P. Saihac, J.P. Malet, G. Grandjean, and J. Ponton. 2012. Hydrological response of weathered clay-shale slopes: water infiltration monitoring with time-lapse electrical resistivity tomography. *Hydrol. Process.* 26:2106-2119, doi:10.1002/hyp.7983.
- Ward, S.H. 1990. Resistivity and induced polarization methods. p.147-189. *In* S.H. Ward (ed.) *Geotechnical and Environmental Geophysics*. Society of Exploration Geophysicist, Tulsa, Oklahoma.
- Weisberg, S. 2005. Polynomials and Factors. p. 115-147. *In* S. Weisberg (ed.) *Applied linear regression*. John Wiley & Sons, Inc., Hoboken, NJ.

## **Chapter 4: Characterizing Hydrological Processes at the Ecological Site Scale: Coupling Rainfall Simulation with Surface Geophysical Measurements**

### **Abstract**

Ecological sites (ES), hillslope scale soil-vegetation complexes, provide a useful framework for studying complex rangeland ecohydrologic processes. High-quality hydrologic field investigations are needed to quantitatively link ES characteristics to hydrologic function. Geophysical tools are useful in this context because they provide valuable information about the subsurface at large spatial extents. We conducted 20 field experiments integrating time-lapse electrical resistivity tomography (ERT) and variable intensity rainfall simulation on hillslope plots at five different ESs within the Upper Crow Creek Watershed in southeastern Wyoming. Surface runoff was measured using a pre-calibrated flume. Infiltration information from the rainfall simulator and site specific resistivity-water content relationships coupled with the ERT datasets were used to track the wetting front through time. First order constraints on subsurface structure were made at each site using ERT, seismic refraction and ground penetrating radar. Sites ranged from infiltrating 100% of the applied rainfall to converting over 40% of the rainfall into surface runoff. ANCOVA results indicated significant differences in the rate of the wetting front progression, ranging from  $0.346 \text{ m min}^{-1/2}$  for sites with a subsurface dominated by saprolitic material to  $0.156 \text{ m min}^{-1/2}$  for sites with a well-developed soil profile. There was broad agreement in subsurface structure between the geophysical methods with GPR typically providing the most detail. Joint interpretation of the geophysics showed that subsurface features such as granite corestones and layers with high clay content had a large effect on the infiltration process. Linking surface information from the rainfall simulator with subsurface information provided by the geophysics, we are able to discern the characteristics that distinguish the hydrologic response of diverse ESs.

**Keywords:** Infiltration, hydrogeophysics, electrical resistivity tomography, rainfall simulation, wetting front, ecological sites

Carey, A.M., Paige, G.B., Carr, B.J., Holbrook, W.S., Miller, S.N., 2016. Characterizing hydrological processes at the ecological site scale: Coupling rainfall simulation with surface geophysical measurements. *Hydrol. Process.*

***In preparation for submission to Hydrological Processes. Anticipated Submission Date: October, 2016***

## **Introduction**

Rangelands account for approximately 31% of the land area in the US (Havstad *et al.*, 2009) and process a substantial portion of freshwater resources. These landscapes are concentrated in arid and semi-arid regions of the western US where water is a limited resource (Branson *et al.* 1981). Understanding hydrologic processes and the factors influencing water yield in these environments is critical for rangeland managers to meet current and future water demands in the face of increasing population (Havstad *et al.*, 2009) and a changing climate Polley *et al.*, 2013). However, extreme spatial variability in rangeland soils, vegetation and climate makes quantifying and modeling these processes challenging (Pilgrim *et al.*, 1988; Pierson *et al.*, 2002).

Ecological sites (ESs), defined as distinct associations of physical characteristics (e.g. soil, topography and climate) capable of producing vegetation of specific type and amount, have been established as the basic landscape unit for managing complex rangeland systems (USDA, 2013). Long-term dynamics of an ES are organized into state-and-transition models (STM), with states representative of stable vegetation complexes and transitions the trajectory between states. Rangeland hydrologic response has been shown to be strongly influenced by an ES in a given state (Stone *et al.*, 2008; Carey and Paige, 2016). To improve the applicability of the ES

framework for managing rangeland water resources, additional quantitative information relating hydrologic function to ESs and their associated characteristics is needed (Williams *et al.*, 2016).

Subsurface flow dynamics are especially difficult to characterize and have been poorly represented in rangeland hydrology studies (Salve and Tokunaga, 2000). Studies that rigorously investigate these processes typically use traditional *in situ* observational platforms such as tensiometers and piezometers. These methods can be invasive leading to modification of subsurface structure and are limited to sampling at the point scale (Robinson *et al.*, 2008). In contrast, geophysical techniques provide minimally invasive ways to characterize and monitor the hydrogeology of the subsurface over large spatial extents (Binley *et al.*, 2015). Electrical resistivity tomography (ERT) has emerged as a useful geophysical tool to study the subsurface. ERT measures the spatial distribution of resistivity, influenced by the degree of water saturation, clay content and mineralogy. Due to the general tendency of decreasing resistivity with increasing water content, ERT has commonly been used in a time-lapse capacity to monitor infiltration processes at the event scale (Michot *et al.*, 2003; Batlle-Aguilar *et al.*, 2009; Dietrich *et al.*, 2014) and seasonal moisture fluctuations (French and Binley, 2004; Jayawickreme *et al.*, 2008; Schwartz *et al.*, 2008). Other geophysical tools such as seismic refraction and ground penetrating radar (GPR) can provide valuable information regarding subsurface structure (Mills 1990; Neal, 2004; McClymont *et al.*, 2012, Holbrook *et al.*, 2014).

Coupling rainfall simulation with time-lapse ERT is advantageous in that it provides a controlled environment in which to study surface and subsurface flow dynamics. This is important for arid and semi-arid rangeland environments where rainfall is infrequent and spatially variable (Mitchell, 2000). Travelletti *et al.* (2012) showed that this methodology can successfully be used to approximate wetting front (WF) progression and identify regions of

steady state flow under constant rainfall application. Forward modeling of a leachate injection by Clément *et al.* (2011) provided additional information on delineating and mapping the WF using time-lapse ERT. In this study, we use time-lapse ERT coupled with variable intensity rainfall simulation. This methodology allows us to study flow dynamics at multiple rainfall intensities in order to characterize the spatial variability of infiltration capacity and provide additional constraints on mapping the WF progression.

The objectives of this study were: 1) to quantify the partitioning of surface and subsurface flow on rangeland ESs with an emphasis on characterizing the spatial and temporal development of the infiltration plume and 2) provide a first-order, site-specific constraint on the subsurface structure using geophysics. Combining information of the subsurface with results from the rainfall simulation experiments provides a unique insight into hydrologic function at the ES scale. Datasets generated from this study provide quantitative information that can improve the ES framework for the management of rangeland water resources. To our knowledge the application of surface based geophysical methods such as these to the study of rangeland hydrology has been very limited.

## **Study Area**

The study was conducted in the Upper Crow Creek Watershed (UCCW) in southeast Wyoming (Figure 4.1). UCCW is a 94 km<sup>2</sup> semi-arid rangeland watershed that ranges in elevation from 2200 to 2760 m. Upland areas are dominated by xeric grasses and shrubs typically occurring in low densities with large intermixed areas of bare ground. High elevations are characterized by coniferous forests and low elevations by riparian areas comprised of willows, aspens and riparian grasses. Large granitic outcrops can be observed throughout the

landscape. The majority of the watershed is underlain by 1.43-Ga Sherman granite batholith that weathers to form a thick grus (Frost *et al.*, 1999).

Five study sites were chosen (Figure 4.1); four of the sites represent distinct ES in the Natural Resource Conservation Service (NRCS) major land resource area 49XA (<https://esis.sc.egov.usda.gov/Welcome/pgApprovedSelect.aspx>). These sites were selected based on their areal extent and their hypothesized influence on the hydrology of the watershed. The representative ESs are coarse upland (CU), shallow loamy (SL), shallow upland (SU) and loamy upland (LU) (NRCS, 2013). The fifth site is representative of a different state of the CU STM and is referred to as CU-2. Detailed characteristics for these study sites are discussed in Carey and Paige (2016) and Perlinski *et al.*, (2016). Here we present a summary of the site characteristics (Table 4.1). At each site four 2 x 6.1 m hillslope plots were installed. Specific plot locations were selected based on relatively uniform slope between 5 and 30% and devoid of any major concavities.

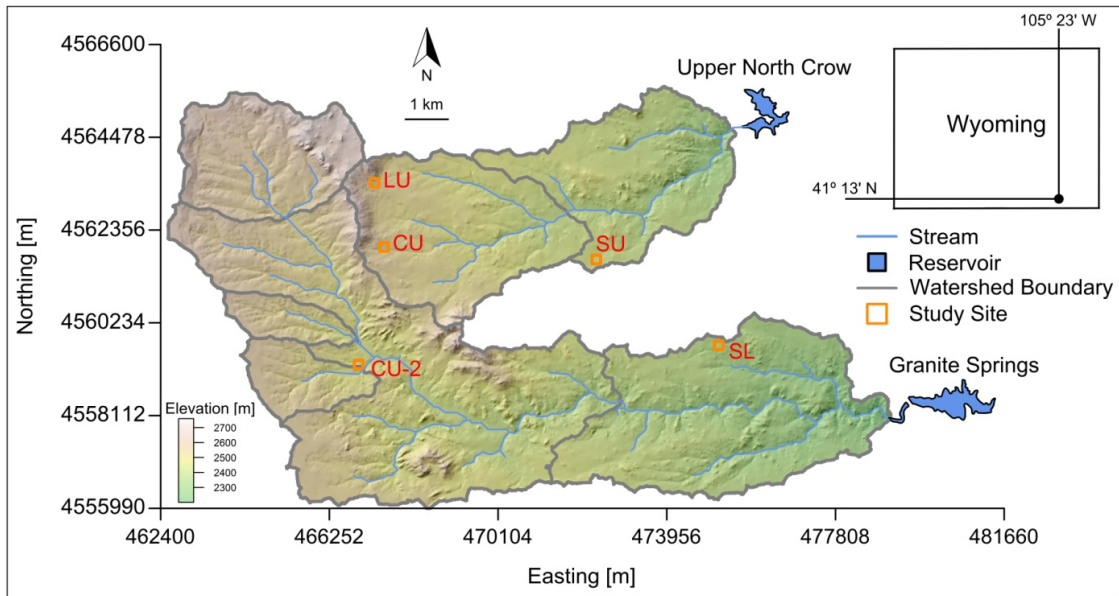


**Figure 4.1: Upper Crow Creek Watershed (UCCW) and the locations of the five study sites. UCCW is comprised of two main catchments delineated by the Upper North Crow and Granite Springs reservoirs. Sub-catchments are shown as part of a nested watershed design established by the University of Wyoming in 2009. Adapted from Carey and Paige (2016).**

**Table 4.1: Site descriptions for the five study sites. Adapted from Carey and Paige (2016).**

Site Characteristic	Coarse Upland (CU)	Shallow Loamy (SL)	Shallow Upland (SU)	Loamy Upland (LU)	Coarse Upland 2 (CU-2)
Year Established	2009	2009	2009	2009	2015 <sup>5</sup>
Ecological Site ID <sup>1</sup>	049XA108WY	049XA162WY	049XA160WY	049XA122WY	049XA108WY
Average Elevation (m)	2547	2368	2433	2567	2470
Average Slope (%)	11.5	9.6	10.7	18.6	11.9
Aspect of Hillslope Plots	South	Northwest	West	Southeast	North
Parent Material Kind <sup>1</sup>	Glacial Till, Alluvium	Residuum, Alluvium	Residuum, Colluvium	Residuum, Alluvium	Glacial Till, Alluvium
Parent Material Origin <sup>1</sup>	Granite	Granite	Granite	Sandstone	Granite
Plant Community	Wheatgrass, Bluegrass, Subshrub	Fescue, Gramma, Subshrub	Fescue, Bunch Grass, Subshrub	Dense Sagebrush, Bluegrass and Brome Understory	Wheatgrass, Fescue, Subshrub
Soil Map Unit <sup>2</sup>	Hapjack-Rogert- Amesmont complex	Boyle-Rock outcrop complex	Hapjack-Rogert- Amesmont complex	Rogert-Rock outcrop- Amesmont complex	Rogert-Rock outcrop- Amesmont complex
Surface Soil Type	Sandy Clay	Clay Loam	Sandy Clay	Loamy Sand	Sandy Clay
Profile Soil Type <sup>3</sup>	Sandy Clay Loam	Sandy Clay Loam	Sandy Loam	Sandy Loam	Sandy Loam
Sand, Silt, Clay (%) <sup>3</sup>	50, 26, 24	60, 18, 22	53, 29, 18	62, 22, 16	49, 46, 5
Coarse (> 2 mm) Fragments (%) <sup>3</sup>	33.9	40.5	40.5	23.2	40.9
Bulk Density (g cm <sup>-3</sup> ) <sup>3</sup>	1.58	1.56	1.47	1.37	1.58
Porosity (%) <sup>3</sup>	40.3	41.2	44.7	48.4	40.3

<sup>1</sup>Natural Resource Conservation Service (NRCS)-Ecological Site Description (ESD).

<sup>2</sup>NRCS 2013.

<sup>3</sup>Values are for the shallow soil profile.

## Methodology

### *Background Geophysics*

At each site, a 55 m line bisecting the runoff plots, referred to as a geophysical line, was established at each site (Figure 4.2). GPR, ERT and seismic refraction datasets were acquired along these lines. Topography was surveyed using a GPS with a 95% precision of  $\pm 0.1$  m and  $\pm 0.15$  m for the horizontal and vertical positions, respectively.

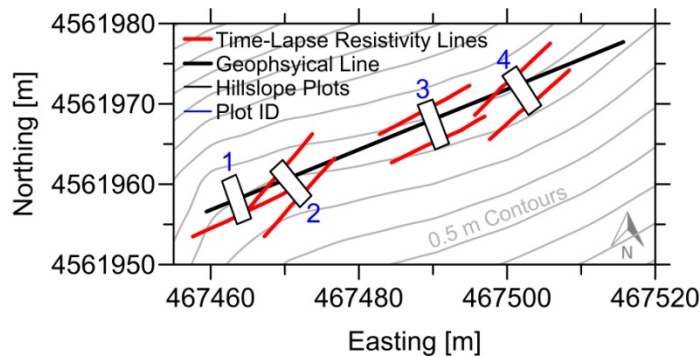


**Figure 4.2: Example geophysical line bisecting the four hillslope plots. Two 13.5 m resistivity lines for the rainfall simulation experiments are also shown. Grey lines indicate the 0.5 m elevation contours.**

### *ERT*

ERT is used to estimate the spatial distribution of resistivity in the subsurface. Direct current is injected into the ground through two current electrodes, establishing an artificial electric potential field. Current flow lines are influenced by the physical properties of the medium under investigation and the properties of the interstitial fluids (Seidel and Lange, 2007). Two additional electrodes measure the electrical potential difference resulting from this field. The electric potential difference, the magnitude of the current and the geometric factor (which describes the arrangement of the current and potential dipoles) are used to compute an apparent resistivity. True resistivity is calculated from the apparent resistivity using an inversion

algorithm (Samouëlian *et al.*, 2005). A comprehensive assessment of electrode arrays and their associated geometric factors is provided by Loke (2001).

Resistivity datasets were collected along the geophysical line at each site using an AGI SuperSting® R8/IP resistivity meter and a cable of 56 electrodes spaced at 1 m. A dipole-dipole array was used with two stacks for each measurement. Time constraints in the field prohibited reciprocal measurements. Inversions were performed using EarthImager 2D® Version 2.4.0 (Advanced Geosciences, 2009). The inversion process is inherently non-unique (Snieder and Trampert, 1999) requiring additional regularization to isolate an optimal solution. We used a smooth model method known as Occam's inversion (Constable *et al.*, 1987). This technique seeks to find the smoothest possible model that fits the data to an *a priori* Chi-squared statistic and assumes a Gaussian distribution of data errors (Advanced Geosciences, 2009). The apparent resistivity pseudosection was used as the starting model and filtering was applied to remove data points with stacking errors greater than 1%. EarthImager allows for additional filtering of poorly-fit data through the use of a cutoff value for the data misfit histogram. On average, 95% of the original dataset was used for the inversion post filtering. The normalized L2-Norm statistic and the root mean squared error (RMS) were used as indicators of inversion quality. Tomograms were clipped using an edge blanking aspect ratio of 1, to prevent interpretation of areas with insufficient data constraining the inversion.

Model sensitivity was addressed using the depth-of-investigation (DOI) method (Oldenburg and Li, 1999). The starting model for the inversion was varied and a normalized difference calculated between the resulting resistivities. Regions well constrained by the data converge to the same value and have a DOI close to zero, while areas less constrained are sensitive to the starting model resulting in higher DOI values. Figure 4.3 shows an example DOI

map for the CU site. High DOI values near the surface are due to the poor near-surface resolution of ERT. This problem is solved by using the apparent resistivity pseudosection as the starting model because the apparent resistivity values at shallower depths are a good approximation of the true resistivity at these locations. A few high ( $> 0.5$ ) DOI areas are intermixed within the profile as a result of sharp transitions between conductive and resistive regions. Low data density in the peripheral of the image also produces high values. We identify the 0.4 DOI contour as a general indicator of the area of the tomogram that is well constrained by the data, with the acknowledgement that a few isolated areas of high DOI values may exist within this region.

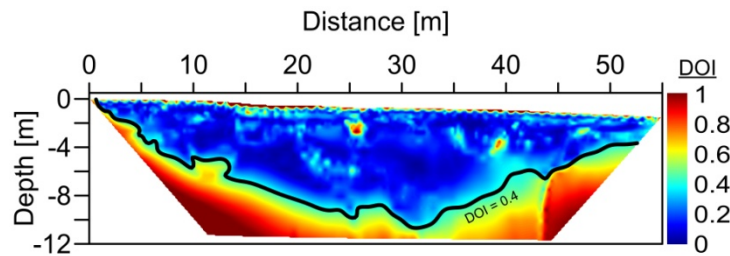


**Figure 4.3: Example DOI map for the CU site. The 0.4 DOI contour is shown as a cutoff between regions of the profile that are well constrained and regions that are less constrained.**

### *Seismic Refraction*

Seismic refraction is used to create primary wave (P-wave) velocity models. Energy from a surface seismic source travels through the subsurface and is refracted when it reaches a material boundary. The speed at which the energy travels back to the surface is a function of both the material composition and compaction. Information obtained from the velocity models includes thickness of weathering layers, depth to fractured bedrock and maps of the water table (Knödel et al., 2007).

Seismic refraction data were acquired using 24-channel Geometrics Geode systems and 10 Hz vertical-component geophones spaced 0.5 m. A sledgehammer striking a stainless steel

plate generated the seismic source. Traces with sufficiently high signal-to-noise ratio were used to manually pick the first arrival travel times. Travel times were inverted using the Seismic Pro 8.0 DW Tomo software module (Geogiga Inc., 2012) to produce velocity models. Inversion starts with a starting velocity model that increases linearly with depth, predicts travel times for the given model and then finds an appropriate smooth update to the model reducing the difference between observed and predicted travel times. This is iteratively solved until a satisfactory fit to the data (indicated by the RMS) is achieved.

We used a starting model with velocity increasing linearly with depth from  $300 \text{ m s}^{-1}$  at the surface to  $5000 \text{ m s}^{-1}$  at a depth of 20 m and performed ten iterations. Sensitivity was addressed by performing ten independent inversions with varying starting models. Areas of the model that were highly sensitive to the value of the starting model typically occurred in regions where raypath density was low. Final velocity models were clipped to match the extent of the resistivity profiles and subsequently clipped to remove areas with low raypath density (Figure 4.4).

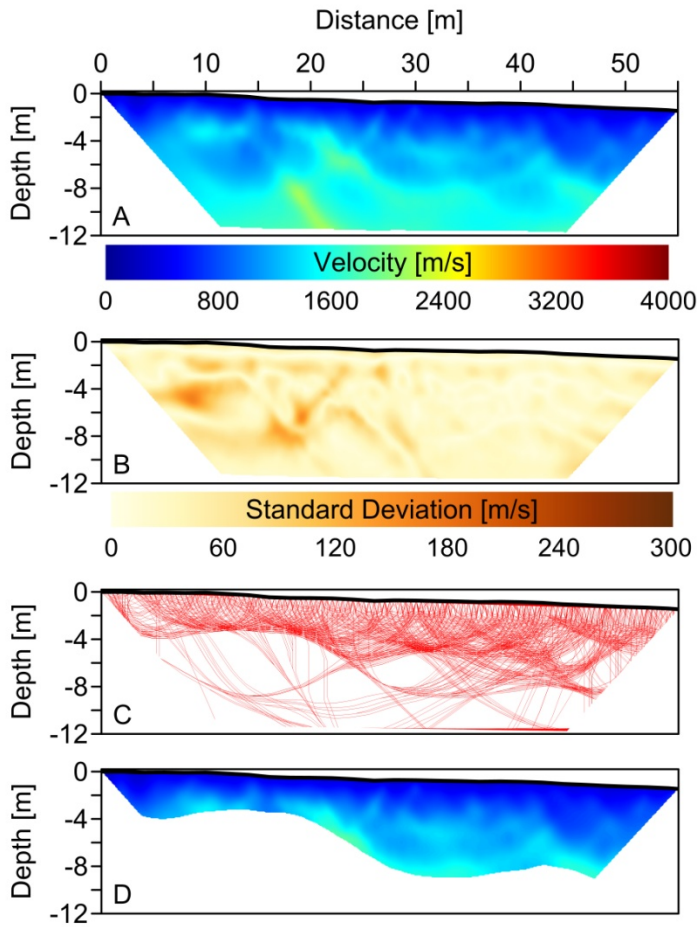


**Figure 4.4: (A)** An example velocity model derived from the seismic surveys and clipped to match the extent of the resistivity tomograms. **(B)** Standard deviation among the ten independent inversions. **(C)** Map of the raypaths. **(D)** Velocity model clipped based on raypath coverage.

Previous seismic refraction surveys in UCCW have shown that a velocity of  $1200 \text{ m s}^{-1}$  is a good estimate for the boundary between saprolite and fractured bedrock (Flinchum *et al.*, 2014). Velocity tends to increase with increasing depth as effective stress increases the bulk and shear moduli. Surveys performed directly over granite outcrops in this watershed and work by a number of authors in similar crystalline bedrock settings (Befus *et al.*, 2011; Holbrook *et al.*, 2014), have identified  $4000 \text{ m s}^{-1}$  as a reasonable cutoff for “pristine” bedrock with little to no fractures. We overlay the  $1200 \text{ m s}^{-1}$  contour on all of the final velocity models to outline the transition between saprolite and fractured bedrock. The  $500 \text{ m s}^{-1}$  contour is also identified to

represent the transition between slower, highly porous medium such as soil and grus material (Bourbié *et al.*, 1987) and the underlying saprolite. Only isolated regions of velocities  $\geq 4000$  m s $^{-1}$ <sup>1</sup> were observed in our final models and therefore the contour is not explicitly identified.

### *GPR*

GPR emits pulses of electromagnetic waves that are radiated from a transmitter antenna into the ground, propagating through the subsurface until they reach a material with a different dielectric permittivity from the surrounding medium. The wave is scattered and is detected by a receiving antenna where the travel time and amplitude are recorded. The relationship between the rate at which the wave propagates and the properties of the material is the fundamental basis for using GPR to provide information about the subsurface (Daniels, 2000).

GPR datasets were acquired by dragging a 100-MHz MALA shielded antenna along the geophysical lines. Processing was done using the matGPR processing package (Tzanis, 2013) using the following steps: (1) time zero adjustment to pick the ground surface, (2) global background removal, (3) gain correction to amplify the deep signal, (4) bandpass filter to remove frequencies outside the target range, (5) apply a wave number filter to reduce ringing effect, (6) estimate average velocity by fitting diffraction hyperbola, (7) *f-k* migration and (8) convert from travel time to depth. Additionally, topography of the line was accounted for by applying a static shift to the radar traces.

### *Rainfall Simulation and Time-Lapse ERT*

Rainfall simulations were conducted on the four plots at each site using the Walnut Gulch Rainfall Simulator (WGRS), a variable intensity computer controlled rainfall simulator equipped with four Veejet 80100 nozzles (Paige *et al.*, 2003). The WGRS was centered directly over the plots with nozzle height and outflow pressure consistent with values suggested by Paige *et al.*

(2003). Simulations were conducted in 2014 and 2015. Dry runs were performed under antecedent moisture conditions with rainfall applied at the lowest intensity for 45 min. Wet runs were conducted after allowing 45 min for moisture redistribution. Surface runoff was measured continuously using a pre-calibrated flume. For the wet runs, applied rainfall was increased incrementally after a period of steady state runoff (Carey and Paige, 2016) (Figure 4.5). Applied intensities were 49, 77, 112, 157 and 180 mm hr<sup>-1</sup> for 2014 and 53, 81, 115, 153 and 181 mm hr<sup>-1</sup> for 2015. Two key hydrologic variables were computed for the wet runs: peak runoff ( $Q_{peak}$ ) and the ratio of runoff to applied rainfall defined as the runoff coefficient (C).

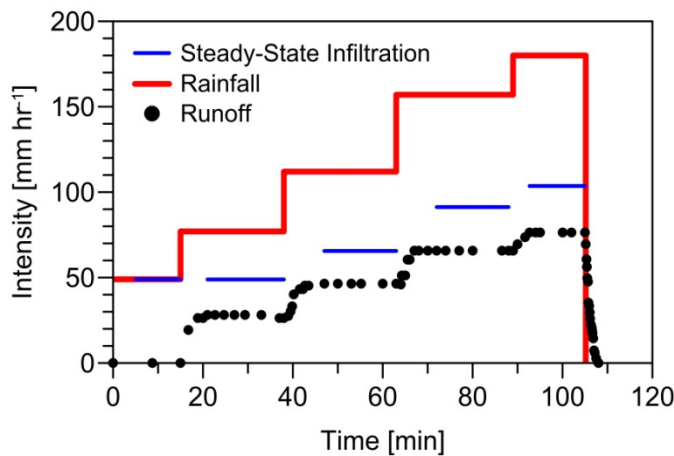


**Figure 4.5: Example hydrograph for a wet simulator run. Applied rainfall rate is indicated by the red line, measured runoff is shown by black circles and the blue line represents steady state infiltration rate (infiltration = rainfall - runoff).**

For the CU, SU, SL and LU sites, two ERT profiles of 28 electrodes at 0.5 m spacing were established perpendicular to the plot one meter above (lower line) and below (upper line) the plot ends (Figure 4.2). The CU-2 site was equipped only with a lower line. Resistivity datasets were continuously collected before, during and after the dry and the wet runs using the SuperSting, alternating between the lines. Datasets were typically collected for 80 min post

simulation to capture redistribution dynamics. Dipole-dipole and pole-dipole arrays were used. Forward modeling by Carey *et al.* (2016) showed that the pole-dipole array accurately images infiltration dynamics while reducing unwanted artifacts that arise during time-lapse inversions of resistivity datasets collected during rainfall events. 2D arrays were chosen over 3D due to the need to characterize subsurface hydrodynamics at a high spatial resolution relative to our 12.2 m<sup>2</sup> plots, as quickly as possible. Reciprocal measurements were again omitted due to time constraints.

Time-lapse inversions of the datasets acquired at various times during simulation were used to map the changes in subsurface resistivity. Changes are typically expressed as a percent change in resistivity ( $\Delta\rho$ ) from an initial or base dataset and are more accurate than assessing absolute resistivity values through time (Samouëlian *et al.*, 2005).

$$\Delta\rho = 100 \left[ \frac{\rho_t - \rho_0}{\rho_0} \right] \quad (1)$$

where  $\rho_t$  and  $\rho_0$  are the resistivities at the initial stage (0) and at some time (t) during monitoring, respectively. Equation 1 is written such that a decrease in resistivity from the background condition results in a negative  $\Delta\rho$ . In these experiments increasing water content from infiltration is assumed to be the only variable causing resistivity changes.

EarthImager 2D employs a time-lapse inversion algorithm that uses a base resistivity dataset as an *a priori* model and inverts the difference between the base dataset and the monitoring datasets collected later (Advanced Geosciences, 2009). Datasets collected prior to the rainfall simulation were not used as the base due to their tendency to generate inversion artifacts (Carey *et al.*, 2016). Instead, the first dataset collected during the wet run was used as the base. Therefore, all results presented in this paper relate specifically to the wet run. On average, 97% of the data was used for the inversion of each dataset following the same filtering procedure

discussed in section 3.1. Average RMS for the inversions was 2.4%. DOI analysis was performed on datasets collected before, during and after simulation to ensure good sensitivity in the infiltration areas.

#### *Resistivity-Water Content ( $\rho$ - $\theta$ ) Relationships and Delimiting the WF*

A main challenge in time-lapse ERT measurements is selecting the  $\Delta\rho$  iso-contour to make meaningful hydrodynamic interpretations (Clément *et al.*, 2011, Audebert *et al.*, 2014). Most inversion algorithms employ smoothing constraints to ensure that a solution is reached (Binley and Kemna, 2005) making delimiting the WF challenging. Ground truthing of tomograms using independent measurements has been successful (Wilkinson *et al.*, 2010; Robert *et al.*, 2011); however this negates the minimally invasive advantage of the ERT measurement. We chose the -10% iso-contour as the best estimate to delimit the WF based on a fitted calibration and multiple lines of reasoning. First, inspecting the first time-lapse tomogram for a given simulation (Figure 4.6) when total elapsed time and total infiltration are relatively small, it can be seen that the shape of the -10% iso-contour is consistent with that we would expect the WF to look like. This holds for all plots. Moreover, the minimum  $\Delta\rho$  observed during this time step is -18% and this contour is biased to the left of the plot. Second, we can confidently rule out the potential of small  $\Delta\rho$  iso-contours as the infiltration boundary. Errors in the final inversion product and in field measurements make accurately targeting small  $\Delta\rho$  challenging. Clément *et al.* (2010) and Travelletti *et al.* (2012) suggested a -5% cutoff for the WF but did not provide reasoning for this decision. To be conservative, accounting for different subsurface materials and noisier datasets due to large resistivity contrasts, we extended this cutoff to -10%. In addition, we used infiltration information from the simulator and site-specific  $\rho$ - $\theta$  relationships to verify the use of the -10% iso-contour to define the WF using the following approach:

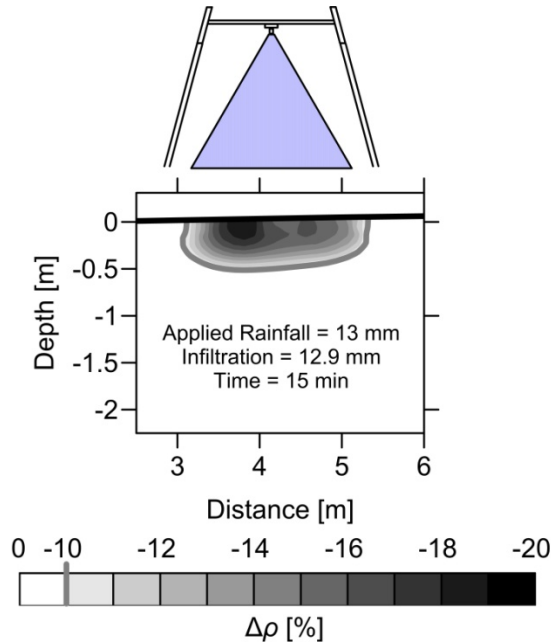


**Figure 4.6: An example time-lapse tomogram at the beginning of a rainfall simulation event showing the change in resistivity ( $\Delta\rho$ ) from the background condition.**

- Boreholes were dug at all sites (except SU), to collect geologic samples at approximately 10 cm intervals to depths of 2.5 m. Subsurface obstructions at the SU site prevented the digging of deep boreholes. Retrieval of undisturbed soil cores to retain *in situ* properties was not possible due to the cohesionless nature of the coarse material.
- An ASTM G57-06 soil test box (ASTM Standard G57, 2006) was used to develop site-specific  $\rho$ - $\theta$  relationships (Figure 4.7A). Samples were oven dried for 24 hours, wetted incrementally and placed in the box to obtain bulk resistivity values. Grab samples were taken to determine the volumetric water content and dry bulk density.
- For any given time-lapse tomogram obtained during simulation, the -10%  $\Delta\rho$  contour was identified and its representative area calculated (Figure 4.7B). An average resistivity value was computed for the area and a bulk  $\theta$  obtained by the relationship in Figure 4.7A.

Adjusting for the average measured porosity, a bulk estimate of the volumetric water content of this area was calculated.

- Infiltration area from the rainfall simulator was determined using the known time-varying infiltration depth (determined as depth of rainfall minus depth of runoff) that occurred over the 2 m width of the simulator plot (i.e. using a 2D view of the infiltration plume).

Comparing the estimated infiltration area with the infiltration area calculated through the use of the rainfall simulator yielded good results across sites (Figure 4.7C). Spread about the 1:1 line can be attributed to a variety of different factors. First, applying locally derived  $\rho$ - $\theta$  relationships to transform tomograms from resistivity to water content space may lead to errors due to poorly represented subsurface heterogeneities (Binley *et al.*, 2002). Second, packing samples into a test box results in artificial pore size distributions changing the  $\rho$ - $\theta$  relationship. Lastly, this technique assumes that the negative  $\Delta\rho$  is due solely to vertically infiltrating water. While this assumption is valid for most of our sites, significant contributions of lateral flow may violate this assumption. Acknowledging these points, we use the -10% contour as the best estimate to delimit the WF.

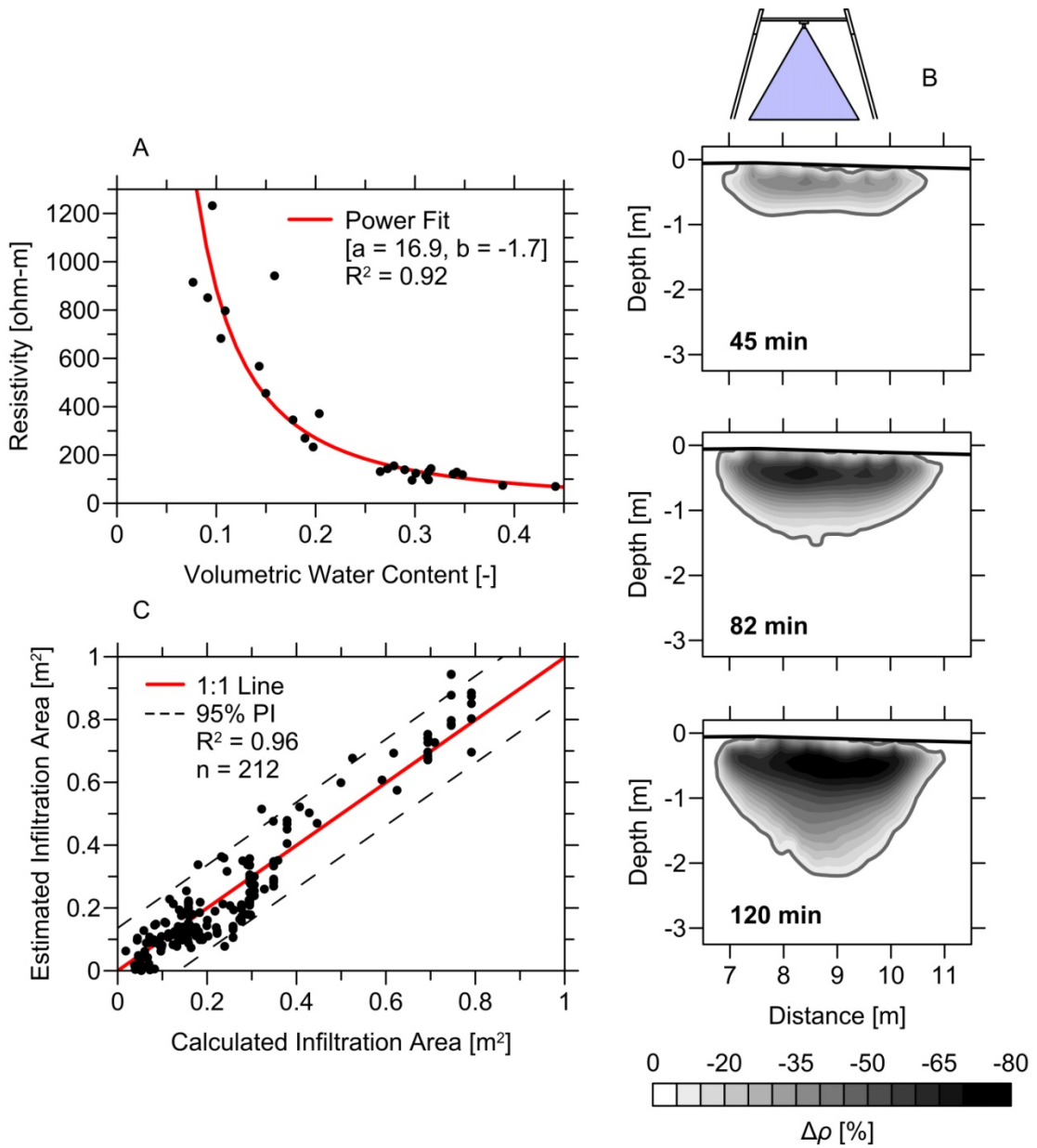


**Figure 4.7:** (A) Example  $\rho$ - $\theta$  relationship fitted with a power function. (B) Progression of the infiltration plume at three different time steps during infiltration delimited by the  $-10\%$   $\Delta\rho$  iso-contour. Position of the simulator spray area is indicated by the triangle. (C) Comparison of calculated vs. estimated infiltration area. A 1:1 line is shown with the 95% prediction interval.

### *Infiltration Parameters*

Linear regressions and calculated infiltration parameters were used to compare subsurface dynamics across individual plots and ESs. Depth to the WF was plotted as a function of the square root of time as a proxy for WF velocity. The square root of time was used obtain a linear fit to describe the relationship. When applicable, separate regressions were developed for the infiltration and redistribution phases. Additional information regarding the redistribution processes was obtained by computing a WF redistribution factor (WFRF; Equation 2).

$$WFRF = \frac{A_t - A_e}{\Delta t} \quad (2)$$

where  $A_e$  is the WF area computed from the time-lapse tomogram collected at the end of rainfall simulation ( $L^2$ ),  $A_t$  is the WF area computed from the last tomogram acquired during the experiment at some time (T) during the redistribution phase ( $L^2$ ) and  $\Delta t$  is the difference in time between the tomograms. Using the tomograms collected closest to the end of rainfall, we computed an anisotropy ratio (AR) i.e. the ratio of lateral to vertical spreading, as well as the minimum and the average  $\Delta\rho$  within the WF. To compare depths and areas of the WF at the end of simulation across sites, these values were normalized by total infiltration depth resulting in normalized WF area (NWFA) and normalized WF depth (NFWD).  $\Delta$ NWFA and  $\Delta$ WRFR values were computed by subtracting the values of the WFRF and the NWFA at the end of simulation of the upper lines from the lower lines. These values provide insight into relative difference between infiltration upslope and downslope. A negative value indicates that the upper line exhibits either a higher WRFR or NWFA than the lower line.

All statistical analyses discussed in this paper were performed using the Statistical Analysis System (SAS) version 9.4 (SAS Institute, 2013).

## Results

### *Surface Runoff*

Runoff results showed clear differences in the surface hydrologic response across ESs (Table 4.2). Detailed discussion of these results is provided in Carey and Paige (2016). On average, the SU site had the largest  $Q_{peak}$  and C values. Moreover, this site exhibited the lowest variability across sites for both parameters. CU and CU-2 on average exhibited similar runoff response with ANOVA tests indicating no significant difference. CU exhibited slightly higher values for both  $Q_{peak}$  and C and both sites had significantly higher variability in runoff parameters compared to SU. SL had a higher infiltration capacity resulting in substantially smaller  $Q_{peak}$  and C values and LU had the largest potential to infiltrate water indicated by the absence of runoff during all simulation runs. It is important to note that all sites, excluding LU and SU, had an anomalous plot with a runoff response significantly different from the remaining plots, accounting for the majority of the observed variability. With the exception of the SU site, none of the plots produced significant runoff at the lowest applied rainfall intensity, suggesting that subsurface flow may be the more dominant process in this watershed. This was noted by Perlinski *et al.* (2016) who monitored natural rainfall-runoff processes at the same sites.

**Table 4.2: Peak runoff rates ( $Q_{\text{peak}}$ ) and the ratio of runoff to rainfall (C) for the wet simulator runs. All LU plots are lumped together because no runoff was measured at this site. The mean and the coefficient of variation (CV) are computed for each variable. Letters within a row indicate statistical significance ( $P \leq 0.05$ )**

Ecological Site	Plot	$Q_{\text{peak}}$ (mm hr <sup>-1</sup> )	C (mm mm <sup>-1</sup> )
CU	1	76.4b	0.38ab
	2 <sup>†</sup>	32.4b	0.14ab
	3	66.8b	0.29ab
	4	68.2b	0.30ab
	Mean (CV)	60.9 (32.0)	0.27 (36.3)
SL	1	31.5c	0.10dc
	2	39.5c	0.15dc
	3	30.6c	0.06dc
	4 <sup>†</sup>	18.1c	0.04dc
	Mean (CV)	29.9 (29.5)	0.09 (56.9)
SU	1	98.5a	0.44a
	2	82.7a	0.39a
	3	83.8a	0.38a
	4	86.5a	0.38a
	Mean (CV)	87.9 (8.3)	0.40 (6.7)
CU-2	1	82.5b	0.36bc
	2	54.3b	0.24bc
	3 <sup>†</sup>	6.7b	0.01bc
	4	56.4b	0.24bc
	Mean (CV)	50.0 (63.2)	0.21 (67.7)
LU	All Plots	0.0d	0.00d

<sup>†</sup>Indicates an anomalous plot compared to the overall site response

### *Infiltration*

Time-lapse tomograms for the infiltration and redistribution phases from the lower lines of plot 4 and plot 2 of the LU and CU-2 sites, respectively, are shown in Figure 4.8A. These

represent the typical infiltration responses observed during these experiments. The WF is outlined and the -20% and -30%  $\Delta\rho$  iso-contours are identified to show internal dynamics. Blue regions represent infiltrating water (negative  $\Delta\rho$ ) while yellow and orange regions represent inversion artifacts (Clément *et al.*, 2009; Carey *et al.*, 2016).

Depth to WF vs. square root of time is well approximated by a linear fit (Figure 4.8B). For CU-2, the WF propagated rapidly through the subsurface ( $m = 0.23 \text{ m min}^{-1/2}$ ) with no significant difference in the depth-time relationship between the two phases (Figure 4.8B). Piston-like flow is indicated by the significant spreading between the three contours and near-surface drying at later times. WFRF is  $0.028 \text{ m}^2 \text{ min}^{-1}$ , AR is 1.1 and the average and minimum  $\Delta\rho$  at the end of simulation is -35% and -63%, respectively. The relationship between cumulative infiltration depth and area of the WF is shown in Figure 4.8C and was used to compute a NWFA of 66.6 m.

For the LU site the rate of WF propagation is less ( $m = 0.12 \text{ m min}^{-1/2}$ ) and there is a clear difference between the infiltration and redistribution processes (Figure 4.8B).. The infiltration plume does not move in a piston-like fashion, indicated by the broadly similar patterns of the three contours in each tomogram (Figure 4.8A). Instead, water is concentrated within a small area. Depth-time relationship for the redistribution phase as well as the low WFRF ( $0.004 \text{ m}^2 \text{ min}^{-1}$ ) indicate that water does not advance much deeper once the rain stops. Additionally, no evidence of drying at the near-surface is present. This concentration of flow results in a lower average (-43%) and minimum (-78%)  $\Delta\rho$  compared to CU-2. AR is 1.5 indicating more lateral spreading and the NWFA of 22.1 m suggests that infiltration at this site represents a much smaller area in the subsurface.

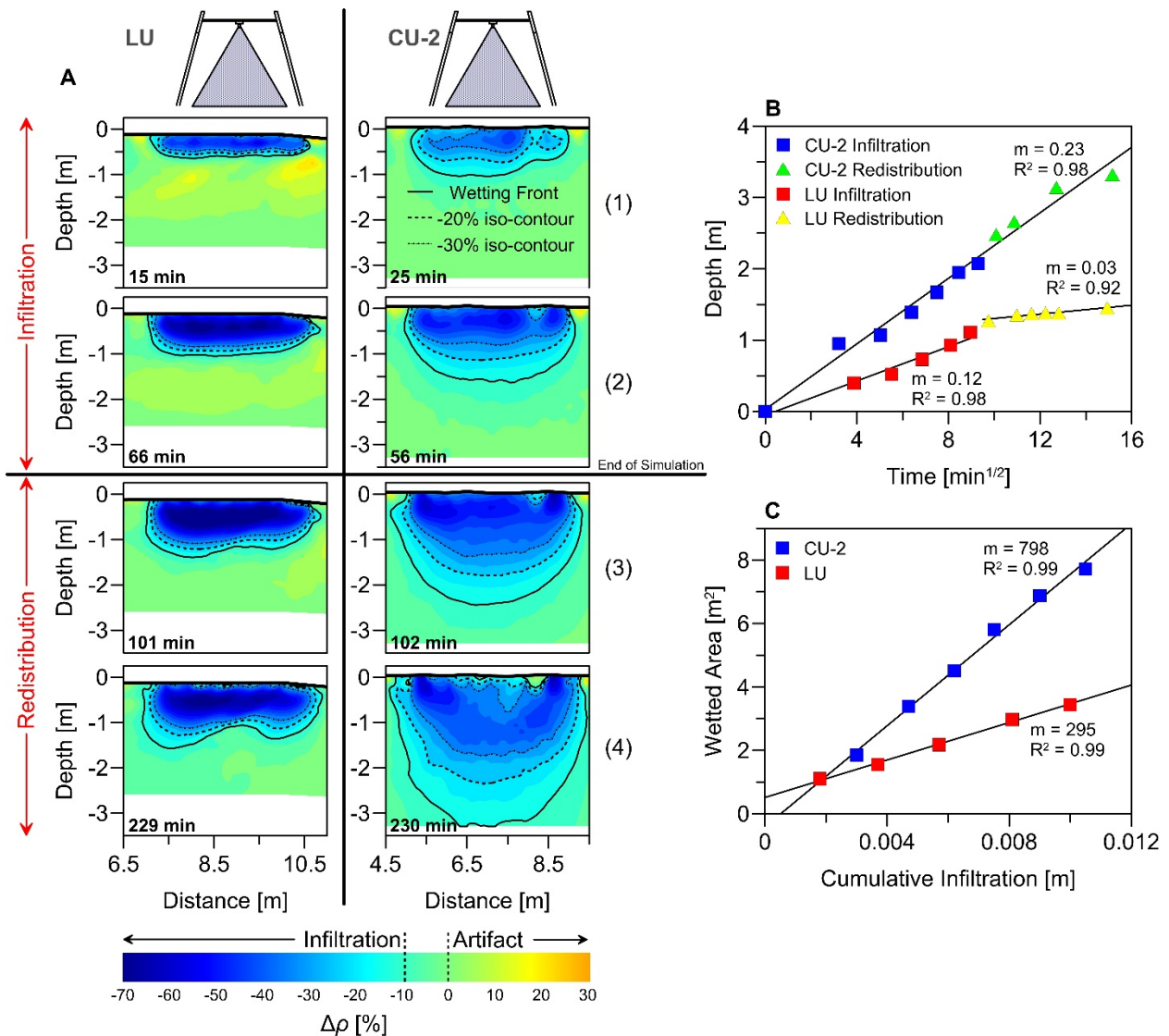


**Figure 4.8: (A)** Example time-lapse tomograms from the lower resistivity lines at LU plot 4 and CU-2 plot 2. The WF, -20% and -30%  $\Delta\rho$  contours are identified. The infiltration phase is described by tomograms 1 and 2 and the redistribution phase by tomograms 3 and 4. **(B)** Depth to the WF versus the square root of time for the redistribution and infiltration phases. The slope of the line provides information regarding WF velocity. **(C)** Relationship between area of the WF derived from the time-lapse tomograms and cumulative infiltration.

As the timing between the upper and lower lines is complex and varied, only the infiltration parameters calculated using the lower lines (with the exception of the  $\Delta NWFA$  and  $\Delta WFRF$  parameters) are presented and discussed (Table 4.3). Large artifacts were present in the inversions

for CU plots 1 and 3 and SU plot 4 and the WF could not be accurately delimited. These plots are omitted from the final results. The upper line for plot 1 at the SU site experienced virtually no infiltration and therefore the  $\Delta$ NWFA and  $\Delta$ WFRF parameters are omitted. As mentioned previously, only a lower line was installed for the plots at CU-2 and therefore  $\Delta$ NWFA and  $\Delta$ WFRF were not calculated.

**Table 4.3: Infiltration parameters for the lower resistivity lines for 17 of the 20 plots. Letters within a row indicate statistical significance ( $P \leq 0.05$ ). Rows without letters indicate no statistical difference amongst sites.**

		Anisotropy		<b>Site</b>	<b>Plot</b>	<b>Ratio</b> (-) <sup>†</sup>	<b>Avg <math>\Delta\rho</math></b> (%) <sup>†</sup>	<b>Min <math>\Delta\rho</math></b> (%) <sup>†</sup>	<b>NWFA</b> (m) <sup>†</sup>	<b>NWFD</b> (-) <sup>†</sup>	<b>WFRF</b> (m <sup>2</sup> s <sup>-1</sup> )	<b><math>\Delta</math>NWFA</b> (m)*	<b><math>\Delta</math>WFRF</b> (m <sup>2</sup> s <sup>-1</sup> )*
LU	1	1.3	-34	-62	41.8a	9.2a	0.044	6.6	0.040				
LU	2	1.2	-25	-50	45.5a	10.3a	0.011	14.3	0.019				
LU	3	1.6	-36	-64	29.2a	7.9a	0.027	-2.6	0.007				
LU	4	1.5	-43	-78	22.1a	6.2a	0.004	2.4	-0.001				
CU-2	1	1.9	-22	-36	73.6b	21.1b	0.035	--	--				
CU-2	2	1.1	-32	-63	66.6b	17.9b	0.028	--	--				
CU-2	3	0.9	-24	-41	51.6b	17.5b	0.033	--	--				
CU-2	4	1.4	-35	-43	81.1b	25.0b	0.031	--	--				
CU	2	1.0	-34	-65	48.4b	15.2b	0.048	23.0	0.039				
CU	4	1.4	-33	-69	79.1b	23.3b	0.012	16.4	-0.001				
SL	1	1.0	-26	-46	31.0a	11.3a	0.022	6.8	0.023				
SL	2	2.1	-24	-49	25.6a	8.9a	0.057	-5.1	0.053				
SL	3	1.5	-30	-59	37.7a	11.1a	0.052	6.6	0.021				
SL	4	1.5	-29	-52	40.7a	13.4a	0.060	13.4	0.045				
SU	1	7.0	-18	-65	33.3	15.9	-0.012	--	--				
SU	2	2.2	-31	-60	81.4b	22.4b	0.015	20.8	0.028				
SU	3	2.1	-31	-63	52.1b	15.7b	0.027	-2.8	0.028				

<sup>†</sup>Parameters calculated using the last ERT tomogram collected during the rainfall application period.

\*Parameters calculated by subtracting the value for the upper line from the lower line.

For the majority of the infiltration parameters, weighted analysis of variance (WANOVA) did not indicate statistically significant differences between the sites. The overall lack of degrees of freedom, especially for the CU and SU sites, greatly reduced the statistical power and therefore the ability to differentiate between site responses. Moreover, there is typically a large spread in the

values within a given site. High spatial variability is common in rangeland hydrology studies (Branson *et al.*, 1972) and contributed to our difficulty in identifying differences. WANOVA did indicate significant differences ( $P \leq 0.05$ ) in both the NWFA and the NWFD, with CU, CU-2 and SU exhibiting larger values for both parameters compared to the SL and LU sites (Table 4.3). SU plot 1 was identified as an outlier for many of the infiltration parameters (the reasons for which are discussed later). This plot was omitted from all WANOVA tests and statistical analyses.

The CU-2 and CU sites had on average the lowest ARs, with CU-2 plot 1 accounting for much of the variability in this parameter. SU had the largest average AR. Not surprisingly, there is a strong positive linear relationship ( $R^2 = 0.65$ ) between the average and minimum  $\Delta\rho$ . SL and CU-2 sites had the lowest average and minimum  $\Delta\rho$  while LU has the largest average  $\Delta\rho$  and the second largest minimum  $\Delta\rho$ . Small WFRF were computed for both the LU and SU sites with significantly larger values computed for SL. In general, the  $\Delta$ NWFA and  $\Delta$ WFRF parameters exhibited a large degree of variability across sites.

Depth to WF vs. the square root of time for all plots is shown in Figure 4.9A. Analysis of covariance (ANCOVA) was used to test if the slopes of these regressions were statistically significant and the results are outlined in Figure 4.9B. A total of six statistically significant groups ( $P \leq 0.05$ ) were identified ranging in slope from 0.156 to 0.468  $m \text{ min}^{-1/2}$ .  $R^2$  values are quite good for all groups ( $> 0.9$ ). If there was no significant difference in the relationship for the two phases, one relationship was used in Figure 4.9A. If differences were significant only the infiltration period was used and a separate relationship was developed for the redistribution phase (Table 4.4). As expected, the slopes of these regressions are much smaller for the redistribution phases, ranging from 0.032 to 0.109  $m \text{ min}^{-1/2}$ .

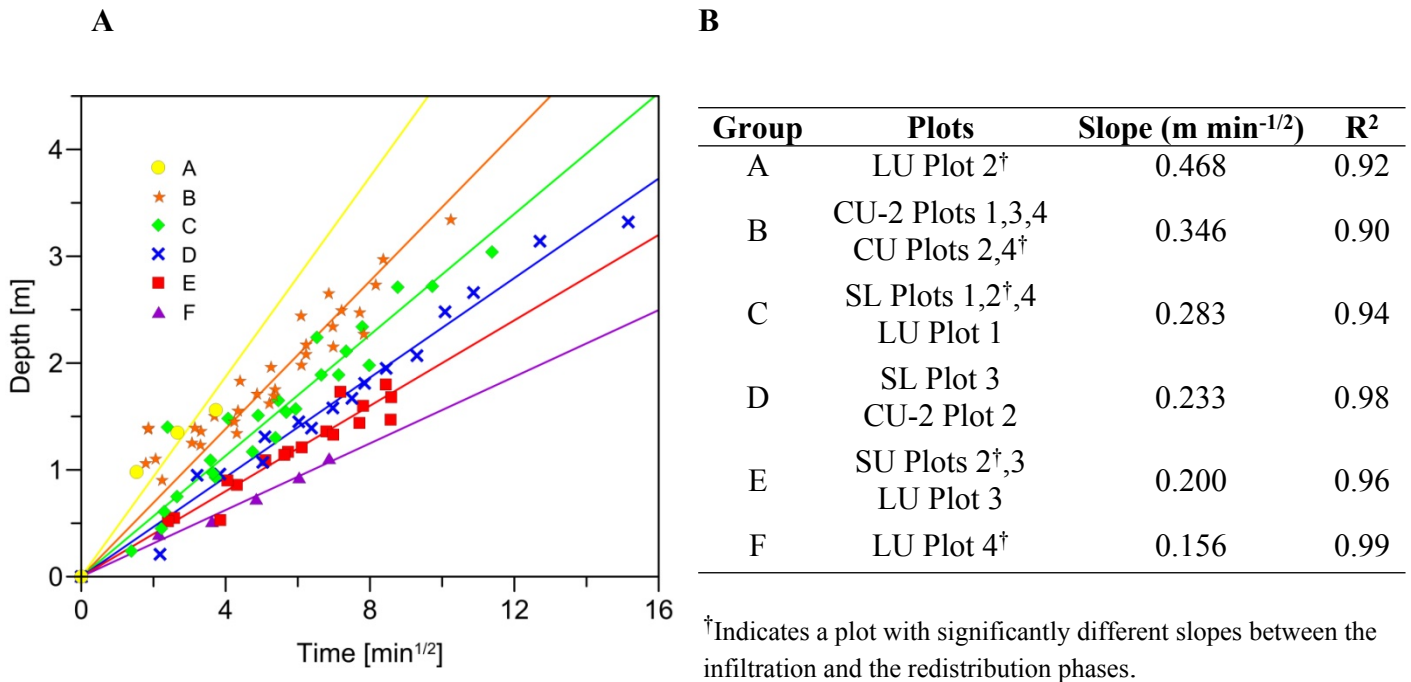


**Figure 4.9:** (A) Relationship between depth to the WF and the square root of time for the infiltration phase. Sites are organized into six groups based on ANCOVA analysis. (B) Slopes and coefficient of determinations ( $R^2$ ) for all groups. The slopes of the lines are all statistically significant at the  $P \leq 0.05$  level.

**Table 4.4: Slope and coefficient of determination ( $R^2$ ) values for the redistribution phase for the plots identified in Figure 4.9B**

Site	Plot	Slope	$R^2$
SL	2	0.109	0.84
CU	4	0.039	0.95
LU	2	0.093	0.99
LU	4	0.032	0.92
SU	2	0.038	0.83

## *Geophysics*

ERT, seismic and GPR profiles are shown in Figure 4.10. Each geophysical method responds to different petrophysical properties, therefore joint interpretation yields a more reliable subsurface image than any single method (Hirsch *et al.*, 2008). It is important to note two key inconsistencies within the dataset. The first is that a GPR profile is not available for the LU site. Dense sagebrush cover at this location impeded GPR data collection. Second, logistical complications in the field at the SL site prevented the acquisition of ERT and GPR datasets in the same location as the seismic survey. The seismic survey follows the established geophysical line while the GPR and ERT datasets were collected using a perpendicular line extending downslope. While these inconsistencies prevent the full joint interpretation of the geophysical methods at these two sites, useful information about subsurface structure can still be inferred.

The 0.4 DOI contour for the resistivity profiles (Figure 4.10A) shows a similar trend for all sites with maximum depth of sensitivity occurring in the middle of the profile and decreasing towards the edges of the tomogram. For the SU site, low sensitivity at shallow depths is shown at approximately  $x = 17$  m due to a large vertical contrast in resistivity in which values increase from  $10^{2.3}$  to  $>10^4$  ohm-m in just 2 m. Large contrasts such as this have been shown by Nyquist *et al.* (2007) to yield areas that appear to be poorly constrained in the final inversion. On average, the velocity models provide information to depths of 5-6 m, while many of the sites have areas of the profile extending much deeper. Velocities do not exceed  $2000\text{ m s}^{-1}$  for the CU, CU-2 and SL sites while the LU and SU models reach velocities as high as  $4000\text{ m s}^{-1}$ . GPR profiles show good radar signal to depths of 4-5 m with the exception of CU-2. In general, the GPR profiles provide the most detail about the subsurface heterogeneity.

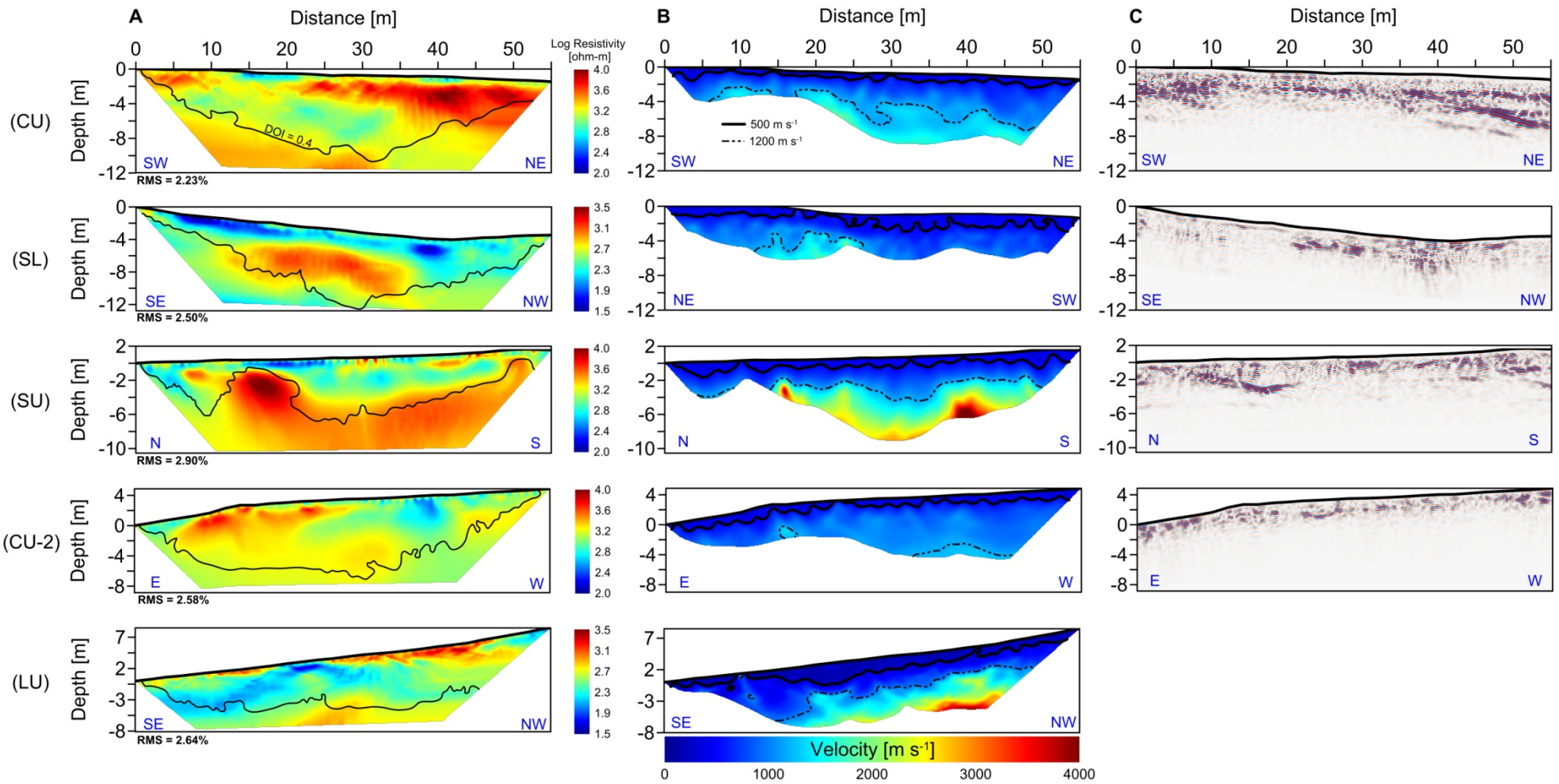


**Figure 4.10:** (A) Resistivity tomograms plotted in log scale with the 0.4 DOI contour delimited by a black line. Individual resistivity scales are used for each tomogram in order to highlight unique features. Line orientation is indicated by the blue letters and root mean square (RMS) error is shown as an indicator of inversion quality. (B) Velocity models derived from seismic surveys. The 500 and 1200 m s<sup>-1</sup> are shown as rough estimates of the lower velocity soil/grus material and the faster velocity fractured bedrock material, respectively. All models share a common scale. (C) Radar profiles from the GPR surveys.

### *CU Site*

A high resistivity feature dipping to the NE is prevalent throughout the tomogram with the exception of 12-22 m where local saturation has reduced the resistivity (Figure 4.10A). This feature is consistent with the  $1200 \text{ m s}^{-1}$  contour in the velocity model (Figure 4.10B) and the dipping reflections seen in the GPR (Figure 4.10C). Through observational pits this region has been identified as saprolite. On the NE side, areas of resistivity higher than the surrounding material ( $>10^{3.85} \text{ ohm-m}$ ) are interpreted as granite correstones intermixed within the saprolite, either too small in diameter or not contrasting enough to be delimited by seismic refraction. For much of the profile a thin layer of low resistivity can be seen at the near surface. This is outlined well by the  $500 \text{ m s}^{-1}$  velocity contour and the lack of reflections in the GPR profile. We interpret this boundary as the well developed soil layer with thickness comparable to field measurements. Fractured bedrock is indicated by velocities  $>1200 \text{ m s}^{-1}$ . This boundary was verified via hand auger on the SW side of the line. In the GPR, this boundary is well represented on the NE side however attenuation of the signal elsewhere in the profile prevents continuous identification of this boundary. Resistivities decrease in the fractured bedrock area potentially due to water within the fractures.

### *SU Site*

This site has the most variation in velocity with depth (Figure 4.10B). High velocities at 15 and 40 m are interpreted as granite with minimal fractures. These regions may also be intrusions of pristine bedrock, however there is insufficient depth of investigation to verify this. High resistivity values ( $> 10^4 \text{ ohm-m}$ ) at 15 m and what appears to be local saturation above (Figure 4.10A), further support the interpretation of this area as impervious granite. Moreover, large reflections at this location can be seen in the GPR results (Figure 4.10C). While broadly

consistent, some differences in the size of this feature can be seen between the three methods. The high velocity region at 40 m is outside the DOI contour of the resistivity tomogram and in an area where the radar signal is attenuated in the GPR. Transition between moderate ( $10^{2.9}$  ohm-m) to high ( $10^{3.3}$  ohm-m) resistivity is in broad agreement with the  $1200 \text{ m s}^{-1}$  velocity contour. Small high resistivity regions at 30 m and from 40-50 m are granite correstones that are well identified in the GPR profile. These correstones have been verified in the field and are extremely prominent in the high resolution resistivity images from the rainfall simulator experiments.

#### *SL Site*

The SL seismic profile (Figure 4.10B) indicates overall low velocities. A small intrusion of fractured bedrock ( $>1200 \text{ m s}^{-1}$ ) with a shallow overlaying layer of soil and grus material can be seen on the NE side. Fractured bedrock is not observed on the SW side and the  $500 \text{ m s}^{-1}$  contour indicates a soil and grus layer twice as thick. As aforementioned, due to complications, the ERT and GPR profiles were acquired along a separate line from the seismic survey. The intersection of these two lines is at 28.5 m on the velocity model and 10.1 m on the ERT and GPR images. A low resistivity layer in the ERT tomogram (Figure 4.10A) approximately 2 m thick, is underlain by a region of higher resistivity (saprolite). Where the signal strength is sufficient the transition between these two layers is outlined in the GPR profile (Figure 4.10C). It is also broadly consistent with the thickness of the  $500 \text{ m s}^{-1}$  at the intersection of these lines. The shallower reflections in the GPR and the particularly low resistivities upslope on the SE side corresponds to a clay layer verified by soil pits. The localized low resistivity region and area of strong reflections at approximately 38 m, is a drainage which contained ponded water at the time of data collection.

### *CU-2 Site*

With the exception of a few small intrusions of fast velocity, the seismic results (Figure 4.10A) indicate that much of the profile is saprolitic material with velocities  $<1200 \text{ m s}^{-1}$ . This subsurface structure is consistent with seismic surveys conducted at this location (Flinchum *et al.*, 2014). A consistently shallow  $500 \text{ m s}^{-1}$  contour is identified. The ERT tomogram provides additional information regarding subsurface heterogeneity. Areas of higher resistivity can be seen from approximately 8.5-24.5 m, interpreted as granite correstones intermixed within the saprolite, and areas of localized saturation can be seen from 0-7.5 m and 35.5-41 m. The GPR profile (Figure 4.10C) shows the most subsurface structure. While some reflections up well with the information in the ERT tomogram there are reflections observed in the GPR that do not correspond with features in the other profiles. This is likely due to the fact that the GPR image provides a higher resolution subsurface image capable of outlining more internal structure.

### *LU Site*

At this site, high velocities at depth on the NW side indicate fresh to slightly weathered granite. The  $500 \text{ m s}^{-1}$  contour is fairly thin at the SE and NW ends and thicker in the middle of the profile. This boundary is not identified by patterns in the ERT tomogram (Figure 4.10A). The saprolite-fractured bedrock boundary is deepest down slope and is shallowest at the NW side of the profile. At approximately 22m there is a sharp transition from the  $500$  to the  $1200 \text{ m s}^{-1}$  contour. Soil samples from this location indicated increasing clay content with depth from about 16% at 0.2 m to 32% at 0.8 m. Moreover, an impervious layer was reached 0.8 m deep. This high clay content region is also identified on the ERT tomogram as a low resistivity ( $10^{1.7} \text{ ohm-m}$ ) area. We interpret this region as weathered bedrock with clay filled fractures. While the velocity model suggest that fractured bedrock is not reached until about 3.6 m, it is likely that the high

clay content is lowering the bulk velocity of this zone and that the 500 m s<sup>-1</sup> contour does not simply represent the soil/grus layer at this location. Near surface areas of high resistivity upslope and downslope overlaying less resistive material are due to lack of clay content, intermixed correstones (indicated by rainfall simulator tomograms) and water use by the dense sagebrush at this site.

## Discussion

The rainfall simulator experiments document and quantify the variability in surface and subsurface hydrologic response across these five ESs. For the surface response, the SU site had the lowest infiltration capacity and consistently produced runoff at each rainfall intensity. In contrast, no runoff was observed at any of the plots at the LU site (Table 2). Sites that from the same ES but in different states (i.e. CU and CU-2) showed no statistical difference in either Q<sub>peak</sub> or C, further supporting the concept that hydrologic response can be characterized at the ES scale. Multiple linear regression analysis by Carey and Paige (2016) showed that much of the variability in Q<sub>peak</sub>, C and steady-state infiltration rates at these sites can be explained by a combination of two ground cover variables: lesser spikemoss (*Selaginella densa* Rydb.) and bare soil. These variables were found to be inversely related to infiltration and beta weights indicated that lesser spikemoss was the most influential. During rainfall events lesser spikemoss can act as a sponge, absorbing moisture and preventing water from infiltrating and reaching surrounding plants (Majorowicz, 1963). This effectively creates impervious patches that promote runoff. Evidence of the effect of moss cover can be observed in the ERT tomograms (Figure 4.10A). Low resistivity regions (<10<sup>2.5</sup> ohm-m) are observed from 12-22 m at CU and from 35.5-41 m at CU-2, roughly corresponding to the locations of plot 2 and plot 3 at these sites, respectively.

These plots have substantially less moss cover than the remaining plots (i.e. CU plot 2 has 68% less moss cover and CU-2 plot 3 has 82% less). It is likely that lack of moss promotes infiltration in these areas leading to localized regions of higher water content clearly outlined in the ERT. Higher infiltration rates and significantly lower C and  $Q_{peak}$  values occur in these areas as indicated by the rainfall simulation results (Table 4.2).

The LU site exhibited a unique hydrologic response as a result of the plant community structure and soil properties (Table 4.1). In contrast to the other sites in which small subshrubs are typically intermixed with various species of graminoids, the LU site is dominated by a dense cover of robust big sagebrush (*Artemisia tridentata* Nutt), creating sagebrush shrub-interspace complexes (Pierson *et al.*, 1994). Lack of coarse fragments? in the loamy soil profile promotes rapid ponding of water in the interspaces. As this water migrates to the sagebrush areas it infiltrates rapidly. Macropores created by the sagebrush root systems results in an extremely high infiltration capacity for this site. Additional rainfall simulation experiments not discussed in this paper, suggest that steady-state infiltration rates for these areas can well exceed 300 mm hr<sup>-1</sup>.

Mapping of the WF progression with time-lapse resistivity proved useful discerning differences in subsurface hydrology. ANCOVA tests identified six groupings of plots based on the slope of the depth to WF vs. square root of time relationships (Figure 4.9B). Group A had the largest slope (0.468 m min<sup>-1/2</sup>) and consisted solely of LU plot 2. This plot had the largest big sagebrush component of any of the simulation plots, comprising over 50% percent of the total vegetation cover. This is compared to an average of 33% for the LU site. Increased density of macropores from the sagebrush root system likely promotes rapid WF movement. This plot is also located upslope, at approximately 46 m on the geophysical line. Field observations at this location have verified small boulders intermixed within the soil profile, which may add to the

increased permeability of the subsurface. These boulders contribute to the higher resistivity values observed in this area in the ERT tomogram (Figure 4.10A). LU plot 2 also exhibited the lowest AR and the largest average and minimum  $\Delta\rho$  values out of all four plots at the LU site (Table 4.3), further supporting rapid vertical movement at this location. It is important to note that during the redistribution phase (i.e. simulator is off) the slope of the depth-time relationship for this plot is significantly lower.

The remaining plots at the LU site have slower rates of WF migration. Plot 1 has a moderate slope of  $0.283 \text{ m min}^{-1/2}$  (group C). This plot is also located upslope in the coarser material but has lower big sagebrush cover (38%) compared to plot 2. The downslope plots (3 and 4) have significantly slower WF movement. These plots are situated directly over the low resistivity region observed in the ERT tomogram (Figure 4.10A). As previously mentioned, the subsurface in this area consists of an impervious layer with high clay content. Time-lapse tomograms show that this layer significantly impedes movement of the WF. Additionally, lack of coarse material in the subsurface and smaller big sagebrush cover for these plots, also contributes to the smaller slopes. This is particularly true for plot 4 which has a slope of just  $0.032 \text{ m min}^{-1/2}$  for the redistribution phase (Table 4.4).

Much like the surface response, the CU and CU-2 sites exhibit similar subsurface hydrologic behavior. With the exception of CU-2 plot 2, all plots at these two sites cluster together in the same group (B) for WF migration, with a large slope of  $0.346 \text{ m min}^{-1/2}$ . These sites also have significantly higher NWFA values than the other sites (Table 4.3). While both CU and CU-2 have a relatively large potential to produce runoff (Table 4.2), the water that does infiltrate moves rapidly through the subsurface. This can be explained by the underlying saprolitic material at these sites. Results from the geophysical lines (Figure 4.10) suggest that the

saprolitic layer at both sites can be quite thick and near to the surface. This is especially the case for the CU-2 site in which the majority of the velocity profile (Figure 4.10B) is classified as slower saprolitic material. The coarse nature of the saprolite leads to high permeability (da Fonesca, 2003), resulting in quick WF movement. High permeability of this layer is also supported by evidence of near surface drying in the time-lapse tomograms similar to the example in Figure 4.8. Only CU plot 4 had a significantly different WF progression during the redistribution phase (Table 4.4). This plot was located at approximately 45 m on the geophysical line in which both the ERT and the GPR results indicate material that is less weathered (i.e. higher resistivity and strong radar reflections). Once the simulator is turned off, the WF moves slowly through this material during redistribution ( $m = 0.039 \text{ m min}^{-1/2}$ ).

The most pronounced effect of the control of subsurface structure on subsurface hydrologic response can be seen at the SU site. All three geophysical methods indicate a large impervious granite feature at approximately 15 m with evidence of a thin layer of saturation above (Figure 4.10). This is the location of plot 1 at the site. Raining over a saturated area with an impervious region below, resulted in the largest runoff response ( $C = 0.44$  and  $Q_{\text{peak}} = 98.5 \text{ mm hr}^{-1}$ ) of all the simulator plots. Water that did infiltrate was influenced by the impervious region and moved laterally resulting in a WF AR of 7.0 (Table 4.3). As previously mentioned, this plot was omitted from all statistical analyses due to the anomalous nature of the subsurface response. SU plots 2 and 3 are in the same group (E) for the slope of the depth-time relationship and are positioned at 28 m and 40 m on the geophysical line, respectively. The slow movement of the WF ( $0.200 \text{ m min}^{-1/2}$ ) at these locations can be attributed to granite correstones, indicated by both the ERT and the GPR. While these regions may appear small on the background ERT tomogram (Figure 4.10A), high resolution tomograms from the simulator experiments indicated

that these correstones are extensive in the near surface. These regions promote saturated areas that when rained over, increase the runoff potential. The correstones themselves also increase runoff due to their impervious nature. These impervious features prevent the vertical movement of water and promote lateral spreading, resulting in high ARs (Table 4.3). In addition, these features reduce the overall volume of infiltrated water leading to large NWFA for these plots.

The SL site had the second highest infiltration capacity after the LU site (Table 4.2). ANOCVA results identified plots 1, 2 and 4 as part of the same WF migration group (C), with a moderate slope of  $0.283 \text{ m min}^{-1/2}$ . A roughly 2 m thick layer of soil/grus was indicated by the ERT and GPR profiles. This was also observed on the SW side of the velocity model. The WF at this site appears to move through this material at moderate speeds without encountering many subsurface obstructions. Dying of the rainfall simulator water provided evidence of preferential infiltration into gopher burrows at this site, which is also contributing to the relatively quick WF movement. Plot 3 was part of group D with a smaller slope of  $0.233 \text{ m min}^{-1/2}$ . Rainfall simulator tomograms for this plot indicated the presence of a shallow clay rich layer that may be obstructing flow.

The general hydrologic function of these five sites as indicated by the rainfall simulator experiments and the background geophysics can be described as follows. Infiltration capacity increases in the following sequence: SU, CU, CU-2, SL and LU. LU has a tremendously high capacity to infiltrate water, yet with the exception of plot 2, this water moves rather slowly through the subsurface. On the opposite side of the spectrum, a combination of moss cover and impervious regions in the subsurface promote large amounts of runoff at the SU site. These impervious regions prevent rapid movement of the wetting front and promote lateral spreading. The CU and CU-2 sites were not statistically different for either surface or subsurface hydrologic

response. While these sites on average exhibited large runoff potential, infiltrated water moves rapidly through the subsurface as a result of coarse saprolitic material. Lastly, the SL site has a very large infiltration capacity and also moves water fairly quickly due to lack of subsurface obstructions and the aid of gopher burrows.

This study highlights the strengths of employing this technique to the study of rangeland hydrology. However, a few key improvements to our experimental design would strengthen our interpretations. Although we have used multiple lines of evidence to ensure that the -10%  $\Delta\rho$  iso-contour is the most reliable estimate of the WF, additional *in situ* measurements or observations are needed to verify the infiltration response when using the “smoothed” inversion method. These measurements would provide greater detail about the true location of the infiltration plume. . In addition, employing 3D ERT may prove more useful in being able to map the entire infiltration plume through time compared to the 2D cross sections. 3D ERT has been shown to reduce unwanted inversion artifacts that may occasionally appear in 2D datasets (Bentley and Gharibi, 2004); however, resolution is lost when using 3D versus 2D arrays for a constant number of electrodes.

## Conclusion

This study coupled time-lapse ERT with variable intensity rainfall simulation to characterize the partitioning of rainfall into surface and subsurface flow components at the ES scale. The controlled nature of the rainfall simulator allowed us to isolate and measure surface runoff, while time-lapse ERT was used to continuously map the subsurface movement of the WF through time. A first-order investigation of the subsurface structure through the use of ERT, seismic and GPR datasets provided a broader context in which to interpret these simulation

experiments. While the optimal resolution of subsurface hydrologic response would be achieved by coupling these experiments with additional *in situ* sensors and observation tools, the technique provides a minimally invasive and spatially extensive approach to quantify these processes and identify differences in main hydrologic function. We documented the significantly different surface and subsurface hydrologic processes exhibited by these ESs across UCCW that are influenced by ES specific soil and vegetation characteristics. Future applications of experiments such as these might be successful for fully mapping variability in hydrology at the ES scale, improving the ES concept for the management of water resources and our ability to understand complex rangeland ecohydrologic processes.

### **Acknowledgements**

This research was supported by the National Science Foundation through the NSF-EPSCoR program (EPS-1208909). The authors thank David Legg and Brady Flinchum for helpful conversations. We thank Andrew Annear, Jeffrey Santos, Michael Rider, Matthew Provart, Elizabeth Traver, Maneh Kotkian and Bea Gordon for field assistance. This is a publication of the Wyoming Center for Environmental Hydrology and Geophysics (WyCEHG).

## References

- Advanced Geosciences. 2009. EarthImager 2D, resistivity and IP inversion software, version 2.4.0. Instruction manual. Advanced Geosciences, Austin, TX, (139 pp.).
- ASTM G57-06, Standard test method for field measurement of soil resistivity using the wenner four-electrode method, ASTM International, West Conshohocken, PA, 2006, [www.astm.org](http://www.astm.org).
- Audebert, M., Clément, R., Touze-Foltz, N., Günther, T., Moreau, S., Duquennoi, C., 2014. Time-lapse ERT interpretation methodology for leachate injection monitoring based on multiple inversions and a clustering strategy (MICS). *J. Appl. Geophys.* 111, 320-333.
- Batlle-Aguilar, Schneider, J.S., Pessel,M., Tucholka, P., Coquet, Y., Vachier, P., 2009. Axisymmetrical infiltration in soil imaged by noninvasive electrical resistivimetry. *Soil Sci. Soc. Am. J.* 73, 510-520.
- Befus, K.M., Sheehan, A.F., Leopold, M., Anderson, S.P., Anderson, R.S., 2011. Seismic constraints on critical zone architecture, Boulder Creek Watershed, Front, Range, Colorado. *Vadose Zone J.*, 10, 915-927.
- Bentley, L.R., Gharibi, M., 2004. Two- and three-dimensional electrical resistivity imaging at a heterogeneous remediation site. *Geophys.* 69, 674-680.
- Binley, A., Cassiani, G., Middleton, R., Winship, P., 2002. Vadose zone flow model parameterisation using cross-borehole radar and resistivity imaging. *J. Hydrol.*, 267, 147-159.
- Binley A. and Kemna A. 2005. DC resistivity and induced polarization methods. p. 192-156. In Y. Rubin and S.S. Hubbard (eds.) *Hydrogeophysics*. Water Sci. Technol. Libr., vol. 50.
- Binley, A., Hubbard, S.S., Huisman, J.A., Revil, A., Robinson, D.A., Singha, K., Slater, L.D., 2015. The emergence of hydrogeophysics for improved understanding of subsurface processes over multiple scales. *Water Resour. Res.*, 51, 3837-3866.
- Bourbie, T., Coussy, O., Zinszner, B., 1987. *Acoustics of porous media*, Gulf publishing Co, Houston, Texas.
- Branson, F. A., Gifford, G.F., Renard, K.G., Hadley, R.F., 1981. *Rangeland Hydrology*. Society for Range Management, Range Science Series No.1, Second Edition. 339 pp.
- Carey, A.M., Paige, G.B., 2016. Ecological site-scale hydrologic response in a semi-arid rangeland watershed. *Rangel. Ecol. Manage.*

- Carey, A.M., Paige, G.B., Carr, B.J., Dogan, M., 2016. Forward modeling to investigate inversion artifacts resulting from time-lapse electrical resistivity tomography during rainfall events. Unpublished results.
- Clément, R., Descoîtres, M., Gunther, T., Oxarango, L., 2009. Comparison of three arrays in time-lapse ERT: Simulation of a leachate injection experiment. ArchéoSciences. 33, 275-278.
- Clément, R., Descloitres, M., Günther, T., Oxarango, L., Mora, C., Laurent, J.P., Gourc, J.P., 2010. Improvement of electrical resistivity tomography for leachate injection monitoring. Waste Manage., 30, 452-464.
- Clément, R., Oxarango, L., Descloitres, M., 2011. Contribution of 3-D time-lapse ERT to the study of leachate recirculation in a landfill. Waste Manage., 31, 457-467.
- Constable, S., Parker, R.L., Constable, C.G., 1987. Occam's inversion: A practical algorithm for generating smooth models from electromagnetic sounding data. Geophys., 52, 289-300.
- Daniels, J. J., 2000. Ground penetrating radar fundamentals. Prepared as an Appendix to a report to the US EPA, Region V, Department of Geological Sciences, The Ohio State University.
- Dietrich, S., P.A. Weinzettel, and M. Varni. 2014. Infiltration and drainage analysis in a heterogeneous soil by electrical resistivity tomography. Soil Sci. Soc. Am. J. 78:1153-1167, doi:10.2136/sssaj2014.02.0062.
- Flinchum, B.A., Holbrook, W.S., Grana, D., St. Clair, J., Carr, B., Hayes, J., A combined near-surface geophysical approach to delineate hydrostratigraphic boundaries in a fractured aquifer in the Laramie Range, Wyoming. American Geophysical Union, Fall Meeting 2014, abstract #NS41A-3832.
- French, H., and A. Binley. 2004. Snowmelt infiltration: monitoring temporal and spatial variability using time-lapse electrical resistivity. J. Hydrol. 297:174-186, doi:10.1016/j.jhydrol.2004.04.005.
- Frost, C.D., Frost, B.R., Chamberlain, K.R., Edwards, B.R., 1999. Petrogenesis of the 1.43 Ga Sherman batholith, SE Wyoming, USA : A reduced, rapakivi-type anorogenic granite. J. Petrol. 40, 1771-1802.
- Geogiga Surface Plus (Version 8.0), 2012. Calgary, Alberta, Canada: Geogiga Technology Corporation
- Havstad, K., Peters, D., Allen-diaz, B., Bartolome, J., Bestelmeyer, B., Briske, D., Brown, J., Brunson, M., Herrick, J., Huntsinger, L., Johnson, P., Joyce, L., 2009. The western United States rangelands: A major resource, in: Wedin, W.F., Fales, S.L. (Eds.),

Grassland: quietness and strength for a new American agriculture. Soil Science Society of America, Madison, WI, pp. 75-93.

Hirsch, M., Laurence R.B., Dietrich, P., 2008. A comparison of electrical resistivity, ground penetrating radar and seismic refraction results at a river terrace site. *J. Environ. Eng. Geophys.*, 13, 325-333.

Holbrook, W.S., Riebe, C.S., Elwaseif, M., Hayes, J.L., Basler-Reeder, K., Harry, D.L., Malazian, A., Dosseto, A., Hartsough, P.C., Hopmans, J.W., 2014. Geophysical constraints on deep weathering and water storage potential in the Southern Sierra Critical Zone Observatory. *Earth Sur. Process. Landf.*, 39, 366-380.

Jayawickreme, D.H., Van Dam, R.L., Hyndman, D.W., 2008. Subsurface imaging of vegetation, climate, and root zone moisture interactions. *Geophys. Res. Lett.* 35, L18404.

Knödel, K., Lange, G., Voigt, H.J., 2007. Environmental geology: Handbook of field methods and case studies. Springer, Berlin, Germany.

Loke, M.H. 2001. Electrical imaging surveys for environmental and engineering studies: a practical guide to 2-D and 3-D surveys. p. 62. Available at [www.geoelectrical.com](http://www.geoelectrical.com)

Majorowicz, A.K., 1963. Clubmoss infestation on northeastern Montana rangeland. *Proceedings of the Annual Meeting of the American Society of Range Management*. 16, 72.

McClymont, A.F., Hayashi, M., Bentley, L.R., Liard, J., 2012. Locating and characterising groundwater storage areas within an alpine watershed using time-lapse gravity, GPR and seismic refraction methods. *Hydrol. Process.*, 26, 1792-1804.

Michot, D., Benderitte, Y., Dorigny, A., Nicoullaud, B., King, D., Tabbagh, A., 2003. Spatial and temporal monitoring of soil water content with an irrigated corn crop cover using surface electrical resistivity tomography. *Water Resour. Res.*, 39, 1138.

Mills, H.H., 1990. Thickness and character of regolith on mountain slopes in the vicinity of Mountain Lake, Virginia, as indicated by seismic refraction, and implications for hillslope evolution. *Geomorphology*, 3, 143-157.

Mitchell, J.E., 2000. Rangeland resource trends in the United States: A technical document supporting the 2000 USDA Forest Service RPA Assessment General Technical Report RMRS-GTR-68. Fort Collins, CO; USDA, Forest Service, Rocky Mountain Research Station.

Neal, A., 2004. Ground-penetrating radar and its use in sedimentology: Principles, problems and progress. *Earth-Sci. Rev.*, 66, 261-330.

NRCS (Natural Resources Conservation Service), 2013. Ecological Site Description (ESD) System for rangeland and forestland. Available at:  
<https://esis.sc.egov.usda.gov/Welcome/pgESDWelcome.aspx>.

- Nyquist, J.E., Peake, J.S., Roth, M.J.S., 2007. Comparison of an optimized resistivity array with dipole-dipole soundings in karst terrain. *Geophysics*, 72, F139-F144.
- Oldenburg, D.W., Li, Y., 1999. Estimating depth of investigation in dc resistivity and IP surveys. *Geophysics*, 64, 403-416.
- Paige, G.B., Stone, J.J., Smith, J.R., Kennedy, J.R., 2003. The walnut gulch rainfall simulator: a computer-controlled variable intensity rainfall simulator. *Appl. Eng. Agric.*, 20, 25-31.
- Perlinski, A.T., Paige, G.B., Miller, S.N., Hild, A.L., 2016. Hydrologic response of four ecological sites to natural rainfall events within a semi-arid watershed. Unpublished results.
- Pierson, F.B., Van Vactor, S.S., Blackburn, W.H., Wood, J.C., 1994. Incorporating small scale spatial variability into predictions of hydrologic response on sagebrush rangelands, in: Blackburn, W.H., Schuman, G.E., Pierson, F.B. (Eds.), *Variability in rangeland water erosion processes*. Soil Science Society of America, Madison, WI, pp. 23-34.
- Pierson, F.B., Spaeth, K.E., Weltz, M.A., Carlson, H.D., 2002. Hydrologic response of diverse western rangelands. *J. Range. Manage.* 55, 558-570
- Pilgrim, D.H., Chapman, T.G., Doran, D.G., 1988. Problems of rainfall-runoff modeling in arid and semiarid regions. *Hydrol. Sci. J.* 33, 379-400.
- Polley, H.W., Briske, D.D., Morgan, J. a., Wolter, K., Bailey, D.W., Brown, J.R., 2013. Climate change and North American rangelands: Trends, Projections, and Implications. *Rangel. Ecol. Manage.* 66, 493-511.
- Robert, T., Dassargues, A., Brouyère, S., Kaufmann, O., Hallet, V., Nguyen, F., 2011. Assessing the contribution of electrical resistivity tomography (ERT) and self-potential (SP) methods for a water well drilling program in fractured/karstified limestones. *J. Appl. Geophys.* 75, 42-53.
- Robinson, D.A., Binley, A., Cook, N., Day-Lewis, F.D., Ferré, T.P.A., Grauch, V.J.S., Knight, R., Knoll, M., Lakshmi, V., Miller, R., Nyquist, J., Pellerin, L., Singha, K., Slater, L., 2008. Advancing process-based watershed hydrological research using near-surface geophysics: A vision for, and review of, electrical and magnetic geophysical methods. *Hydrol. Process.*, 22, 3604-3635.
- SAS Institute [computer program], 2013. SAS Software version 9.4. SAS Institute, Cary, NC, USA.
- Samouëlian, A., Cousin, I., Tabbagh, A., Bruand, A., Richard, G., 2005. Electrical resistivity survey in soil science: a review. *Soil Tillage Res.*, 83, 173-193.

- Schwartz, B.F., Schreiber, M.E., Yan, T., 2008. Quantifying field-scale soil moisture using electrical resistivity imaging. *J. Hydrol.* 362, 234-246.
- Salve, R., Tokunaga, T.K., 2000. Flow processes in a rangeland catchment in California. *J. Range. Manage.*, 53, 489-498.
- Seidel, K., Lange, G., 2007. Direct current resistivity methods, in: Knödel, K., Lange, G., Voigt, H.J. (Eds.), *Environmental geology: Handbook of field methods and case studies*. Springer, Berlin, Germany, pp. 205-237.
- Snieder, R., Trampert, J., 1999. Inverse problems in geophysics, in: Wirgin, A., (Ed.), *Wavefield inversion*, Springer Verlan, New York, pp. 119-190.
- Stone, J.J., Paige, G.B., Hawkins, R.H., 2008. Rainfall intensity-dependent infiltration rates on rangeland rainfall simulator plots. *Trans. ASAE (Am. Soc. Agric. Eng.)* 51, 45-53.
- Travelletti, J., Saihac, P., Malet, J.P., Grandjean, G., Ponton, J., 2012. Hydrological response of weathered clay-shale slopes: water infiltration monitoring with time-lapse electrical resistivity tomography. *Hydrol. Process.*, 26, 2106-2119.
- Tzanis, A., 2013. MATGPR, Manual and Technical Reference, Department of Geophysics, University of Athens Panepistimiopoli, Zografou 15784, Greece, [atzanis@geol.uoa.gr](mailto:atzanis@geol.uoa.gr).
- USDA (US Department of Agriculture). 2013. Interagency ecological site description handbook for rangelands. United States Department of Agriculture, Washington, DC, (109 pp.).
- Wilkinson, P.B., Meldrum, P.I., Kuras, O., Chambers, J.E., Holyoake, S.J., Ogilvy, R.D., 2010. High-resolution electrical resistivity tomography monitoring of a tracer test in a confined aquifer. *J. Appl. Geophys.* 70, 268-276.
- Williams, C.J., Pierson, F.B., Spaeth, K.E., Brown, J.R., Al-Hamdan, O.Z., Weltz, M.A., Nearing, M.A., Herrick, J.E., Boll, J., Robichaud, P.R., Goodrich, D.C., Heilman, P., Guertin, D.P., Hernandez, M., Wei, H., Hardegree, S.P., Strand, E.K., Bates, J.D., Metz, L.J., Nichols, M.H., 2016. Incorporating hydrologic data and ecohydrologic relationships into ecological site descriptions. *Rangel. Ecol. Manage.* 69, 4-19.

## **Chapter 5: Conclusions and Recommendations for Future Work**

### **Primary Findings and Significance**

The aim of this research was to couple hydrologic and geophysical observational platforms to describe and quantify the partitioning of rainfall into surface and subsurface flow at the ecological site (ES) scale. This research was sponsored by the Wyoming Center for Environmental Hydrology and Geophysics (WyCEHG). WyCEHG was established in 2012 through the NSF EPSCoR program (EPS-1208909) to make scientific advances that reduce the longstanding uncertainties in understanding the fate and transport of water resources in the western United States. Through these advancements water resource management can be improved and made more robust in order to deal with the evolving needs of the public and potential disturbances such as climate change, land use change, bark beetle infestation and energy extraction. To achieve this, WyCEHG links the fields of watershed hydrology and geophysics (i.e. hydrogeophysics) to develop interdisciplinary approaches to characterize the processes that partition water into streams, soils, rivers and aquifers.

In keeping with WyCEHG's mission and objectives, I conducted field experiments coupling a traditional hydrologic observational platform, rainfall simulation, with well-established geophysical techniques, to study the partitioning of rainfall into surface and subsurface flow. I conducted these experiments on the UCCW, a high elevation rangeland watershed in southeastern Wyoming. Focusing on rangeland environments is critical for understanding western water resources because rangelands represent approximately 80% of the land mass west of the 100<sup>th</sup> meridian. ESs have been well established as the basic land management unit for these landscapes (Brown, 2010) and therefore represent a useful spatial scale to quantify the variability in rangeland hydrologic response.

The first research topic presented in this thesis (Chapter 2) demonstrated the viability of using ESs to characterize surface hydrologic processes in rangeland environments. This work builds on the hypothesis put forth by Stone and Paige (2003): ecological sites in a given condition should exhibit a characteristic hydrologic response that can be quantified. A total of 20 rainfall simulation experiments were conducted on hillslope plots at different ESs. Apparent steady state infiltration rates (SS) were measured throughout the simulation using an approach described by Hawkins (1982) and Dunne *et al.* (1991), in order to characterize the spatial variability of infiltration capacity. Peak runoff rate ( $Q_{peak}$ ) and runoff ratio (C), were also measured. Surface and ground cover characteristics were measured using the line-point intercept method on all sites. The results of this work were very encouraging. ANOVA analysis indicated statistically significant differences in how ESs partitioned rainfall into runoff response. Sites ranged from infiltrating 100% of the applied rainfall during the experiment to converting over 40% of the rainfall into surface runoff. No difference was found between the runoff-infiltration processes of two sites representative of different states of the same ES. This further supports the concept of characterizing hydrology at the ES scale. Moreover, multiple linear regressions showed that parsimonious models consisting of two to three ground cover variables, could explain on average 83% of the variability in the hydrologic parameters of interest. Lesser spikemoss and bare soil were consistently identified as the most influential variables in the regressions. These findings are a significant step forward in the processes of predicting functional feedbacks between ES characteristics and hydrologic processes. The quantitative dataset created from this work can be integrated into evolving tools like ecological site descriptions (ESD) and state-and-transition models (STM) as well as rangeland assessment models such as the Rangeland Hydrology and Erosion Model (RHEM; Nearing *et al.*, 2011), to

improve our ability to understand and manage the complex ecohydrologic processes on rangelands.

In Chapter 3, the influence of changes in volumetric moisture content and the electrode configuration on the development of artifacts during the time-lapse inversion of electrical resistivity tomography (ERT) data was investigated. Artifact development observed in the time-lapse ERT inversions during field experiments at the Coarse Upland (CU) ES was the main motivation for this work. A number of authors have also identified problems with inversion artifacts when using ERT in a time-lapse capacity (Guerin *et al.*, 2004; Jolley *et al.*, 2007; Batlle-Aguilar *et al.*, 2009; Clément *et al.*, 2009a, 2009b; Rings and Hauck, 2009; Clément *et al.*, 2010). Information obtained from the rainfall simulator experiments and characteristics of the subsurface structure were used to forward model the infiltration process to produce synthetic apparent resistivity datasets. Using a dipole-dipole array, we showed that a large reduction in artifact development could be achieved by reducing the resistivity contrast (i.e. increasing the volumetric water content) between subsurface layers. In addition, we identified a modified version of the pole-dipole array as the optimal electrode configuration to image infiltration dynamics based on: (1) the reduction in artifact development and (2) the ability to accurately delineate the general infiltration zone. This is consistent with work by Loke (2001), Dahlin and Zhou (2004) and Clément *et al.* (2010), who also identified the benefits of using the pole-dipole array for both “one-time” and time-lapse applications. While the results of this study are useful for all ERT applications, it is particularly important for researchers and industry professionals using EarthImager 2D® (Advanced Geosciences, 2009) software for the inversion of apparent resistivity data. Due to its low cost and user friendly GUI, EarthImager 2D is increasingly being used to study hydrodynamics in the vadose zone (Nyquist, 2008; Schwartz, 2008; Dimova *et al.*,

2012; Dietrich *et al.*, 2014; Hester *et al.*, 2015). This research provides insights into how to obtain proper subsurface images and ultimately reliable estimates of subsurface flow processes in these scenarios.

The third research topic (Chapter 4) was the most comprehensive. A hydrogeophysics approach was taken to characterize surface hydrologic function at the ES scale. I coupled time-lapse ERT with rainfall simulation to study the real time partitioning of rainfall into surface and subsurface flow components. Runoff was measured continuously using a pre-calibrated flume and building off a method described by Clément *et al.* (2011), I coupled information from the rainfall simulator with resistivity-water content relationships to characterize and monitor the position of the wetting front (WF) through time. Additionally, ERT, seismic refraction and ground penetrating radar datasets were collected to provide information about subsurface structure. Significant differences in both surface and subsurface hydrologic processes were observed across ESs. As discussed in Chapter 2, the variability in surface processes can largely be explained by ground cover parameters. Joint interpretation of the geophysics results outlined features responsible for the variation in WF migration. For example, sites dominated by saprolite material exhibited rapid WF movement even if the potential to produce runoff was high. Subsurface obstructions observed by the geophysics caused the WF to move significantly slower at other sites. Through these experiments I collected datasets relating surface and subsurface hydrologic function to ES characteristics. This work outlines the potential for applying this methodology to the study of rangeland hydrology, to provide a better understanding of the factors influencing the fate and transport of water resources on semi-arid rangelands.

## **Limitations of this Research**

Though the research was very successful and yielded valuable information and significant results, there are areas of this research that require strengthening through further investigations. First and foremost, it is important to acknowledge that this study, through labor and time intensive, produced a limited dataset with which to make extensive inferences about hydrologic response at the ES scale. This problem of lack of data is fairly common in experimental hydrology (Burt and McDonnell, 2015). These rainfall simulator experiments are extensive in their preparation, required time, materials and manpower. It was not uncommon to spend at least 2-3 days to successfully perform a complete set of simulations on one plot. As a result, we were only able to acquire 20 plot scale datasets that coupled variable intensity rainfall simulation with ERT data across five sites (i.e. four plots per site). This lack of degrees of freedom made statistical analysis challenging at every juncture of this study and did not allow for much flexibility. Furthermore, each plot represented a sub-sample of a given ES. While we were able to develop many useful relationships between ES characteristics and hydrologic function, we did not actually perform any ES replications. We cannot say for certain that the response we observed for a given ES will hold at the same ES elsewhere in the watershed. Replication is clearly necessary to strengthen the argument that ESs have a distinct and quantifiable hydrologic response; however, this is made challenging by the fact that 1) ESs have inherently high natural variability and 2) ES mapping and establishment of ESDs is currently in the early stages of development for much of the state of Wyoming.

Additional point scale measurements and investigations to ground truth the geophysics results are lacking in this study. These measurements would be useful for providing *a priori* geological information to help constrain inversions to ensure a reliable solution is reached

(Jackson, 1979). For the ERT and the seismic surveys in this study, some degree of smoothing was imposed in the inversions. Point scale measurements would prove useful in this capacity to aid in the accurate delineation of key subsurface transitions. Arguably the largest lack of ground truthing for the geophysical data is with the time-lapse ERT images of the wetting front. The rate of wetting front migration is a very important parameter in this study and provides information on permeability and flow process in the subsurface. For our research, multiple lines of evidence were used to ensure that the -10% change in resistivity iso-contour was the most reliable estimate of the wetting front (Chapter 4). Noise in the resistivity datasets, smoothing of the final inversions, inversion artifacts, error in the resistivity-water content relationships and the inherent variability in subsurface petrophysical properties between sites, all combine to produce some degree of uncertainty around this claim. To determine the wetting front with the greatest amount of accuracy, excavation of the subsurface is ultimately necessary. A number of studies have outlined the usefulness of this approach (Weiler and Flühler, 2004; Cey and Rudolph, 2009; Haarder *et al.*, 2011). We omitted excavation at our sites to limit the amount of potential disturbance. As previously mentioned these sites are part of a long term study established in July 2009 to study natural-rainfall runoff processes. Excavation studies are not repeatable and any excavation at these sites would significantly alter the vegetation and soil properties, likely changing the hydrologic response.

## **Recommendations for Future Work**

Based on the challenges experienced with this research, a logical follow up would be further testing of the methodology, i.e. the coupling of rainfall simulation with time-lapse ERT measurements. It would be beneficial to do this under more controlled conditions compared to

our field sites in the Upper Crow Creek Watershed (UCCW). I propose that these experiments be conducted at the Laramie Research and Extension Center (LREC). The LREC provides a relatively flat and homogenous landscape and is logically advantageous for rainfall simulation due to the nearby water supply.

While our experiments are fairly robust in analyzing surface hydrologic processes, three specific changes in the experimental approach would improve the ability to characterize the subsurface dynamics. First, resistivity datasets should be acquired using 3D arrays. The potential advantages of tracking the entire infiltration plume through time and eliminating inversion artifacts (Bentley and Gharibi, 2004) outweigh the loss of resolution, both temporally and in terms of the final inversion product. A star array should be used for 3D acquisition (Figure 5.1) based on its improvement over the traditional parallel line approach in both the final inversion product (Clément *et al.*, 2010) and its data acquisition speed (Loke and Barker, 1996).

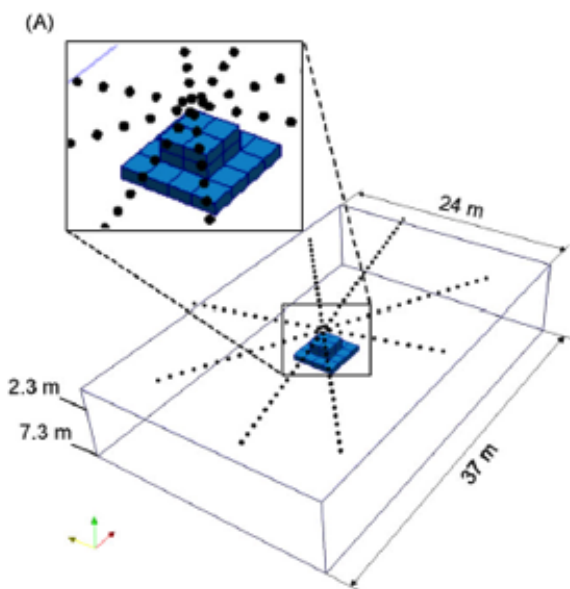


**Figure 5.1: A star electrode array being used to acquire 3D time-lapse ERT datasets during a synthetic infiltration experiment (blue blocks) (after Clément *et al.*, 2011).**

Second, multi-depth soil moisture sensors should be distributed throughout the plot (though difficult to implement in the established long-term runoff plots in the UCCW). This will provide ground truthing of the time-lapse resistivity images. Response in the soil moisture probes can be matched with the percent change in resistivity iso-contours to investigate the effect of smoothing on the inversion product (Clément *et al.*, 2009). Response in the soil moisture probes would also allow more detailed and spatially extensive resistivity-water content relationships to be built in order to transform from resistivity to water content space. This is currently being implemented at the Loamy Upland ES (Parsekian, Kotikian, and Paige personal communication).

Third, performing these experiments at the LREC would allow for plot excavation to visualize the wetting front. This is ultimately the best method to constrain both the ERT and the soil moisture sensor response. It will also provide an opportunity for detailed characterization of the subsurface properties that can then be related to infiltration response. However, as previously mentioned, altering the soil and vegetation properties during excavation would make repeat experiments at the same location impossible.

This research represents the first step in the process of coupling these two observational platforms to quantify the partitioning of rainfall into surface and subsurface flow components. While it has been successful in many aspects, there is a clear path forward for how to improve and advance this method. Making these three adjustments would strengthen the final datasets obtained from this experiment and as a result improve the robustness of the method when applied to natural field conditions.

Another follow up to this work would be to further investigate the inversion techniques available to process time-lapse ERT data during infiltration processes. For example, a multiple inversion clustering strategy (MICS) could be used to reduce the potential of inversion artifacts

and more accurately delineate the infiltration zone (Figure 5.2; Audebert, *et al.*, 2014). MICS and similar approaches (Chambers *et al.*, 2014; Ward *et al.*, 2014) are increasing in popularity and could prove to be a useful techniques to accurately delineate the wetting front. Estimates from these methods can then be compared to our estimates based on the rainfall simulator. There is also the potential to investigate internal dynamics within the wetting front by delineating areas of steady-state flow using an approach outlined by Travelletti *et al.*, 2012. This is particularly advantageous for our experiment because it can be done at every application rate during the simulation to visualize in the subsurface the spatial variability in infiltration capacity.

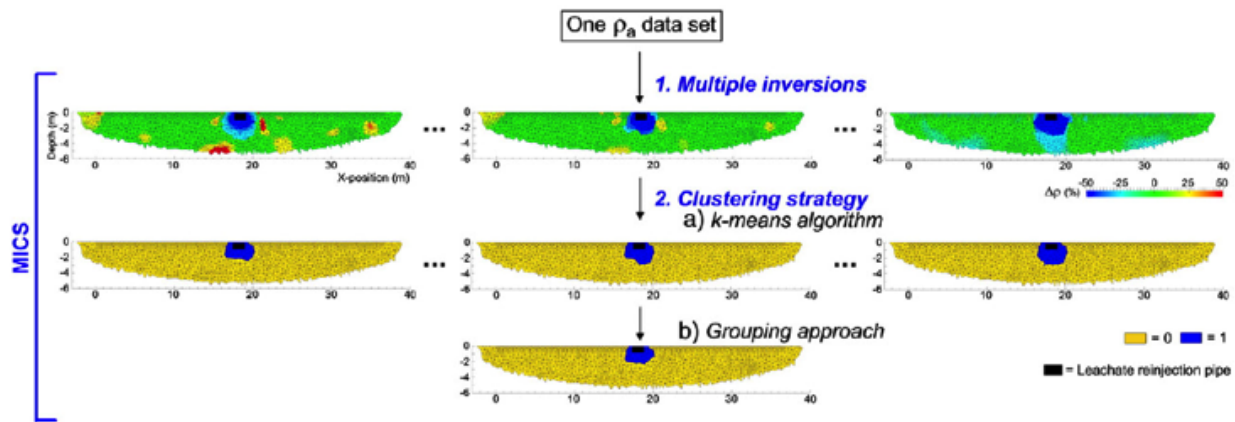


**Figure 5.2: Workflow for the multiple inversions and clustering strategy (MICS) procedure using leachate injection through a pipe as an example. A single apparent resistivity ( $\rho_a$ ) dataset is run through multiple inversions and then a clustering algorithm. Zero areas represent regions that have not been influenced by the infiltration while areas labeled one represent the infiltration plume (after Audebert, *et al.*, 2014).**

The ultimate goal of this work will be to integrate our datasets into distributed hydrologic models. ESs in theory can provide a finer spatial discretization of a watershed compared to the traditional sub-watershed and contributing source area approaches. Burns *et al.*, 2011 showed that calibrating hydrologic models using parameters developed at various spatial scales (i.e. from small to large), could outperform lumped calibration techniques for both runoff and erosion prediction. Using the datasets derived from these types of field experiments, parameter estimates

at the ES scale could be made and modeling results compared to the default or more traditional techniques.

It is my hope that this research and the potential research outlined in the future recommendations section, will improve our ability to understand complex ecohydrologic processes on rangeland environments to effectively manage water resources for current and future generations.

## References

- Advanced Geosciences. 2009. EarthImager 2D, resistivity and IP inversion software, version 2.4.0. Instruction manual. Advanced Geosciences, Austin, TX. 139 p.
- Audebert, M., Clément, R., Touze-Foltz, N., Günther, T., Moreau, S., Duquennoi, C., 2014. Time-lapse ERT interpretation methodology for leachate injection monitoring based on multiple inversions and a clustering strategy (MICS). *J. Appl. Geophys.* 111, 320-333.
- Batlle-Aguilar, Schneider, J.S., Pessel, M., Tucholka, P., Coquet, Y., Vachier, P., 2009. Axisymmetrical infiltration in soil imaged by noninvasive electrical resistivimetry. *Soil Sci. Soc. Am. J.* 73, 510-520.
- Bentley, L.R., Gharibi, M., 2004. Two- and three-dimensional electrical resistivity imaging at a heterogeneous remediation site. *Geophys.* 69, 674-680.
- Burns, I.S., Guertin, D.P., Goodrich, D.C., 2010. Multi-scale calibration of KINEROS-DWEPP, a combined physically-based hydrologic model and process-based soil erosion model. 2<sup>nd</sup> Joint Federal Interagency Conference, Las Vegas. NV.
- Burt, T.P., McDonnell, J.J., 2015. Whither field hydrology? The need for discovery science and outrageous hydrological hypotheses. *Water Resour. Res.* 51, 5919-5928.
- Cey, E.E., Rudolph, D.L., 2009. Field study of macropore flow processes using tension infiltration of a dye tracer in partially saturated soils. *Hydrol. Process.* 23, 1768-1779.
- J.E. Chambers, Wilkinson, P.B., Uhlemann, S., Sorensen, J.P.R., Roberts, C., Newell, A.J., Ward, W.O.C., Binley, A., Williams, P.J., Goody, D.C., Old, G., Bai, L., Derivation of lowland riparian wetland deposit architecture using geophysical image analysis and interface detection. *Water Resour. Res.*, 50, 5886–5905

- Clément, R., Descloitres, M., Günther, T., Ribolzi, O., Legchenko, A., 2009. Influence of shallow infiltration on time-lapse ERT: Experience of advanced interpretation. *C.R. Geosciences* 341, 886-898.
- Clément, R., Descloitres, M., Günther, T., Oxarango, L., Mora, C., Laurent, J.P., Gourc, J.P., 2010. Improvement of electrical resistivity tomography for leachate injection monitoring. *Waste Manage.* 30, 452-464.
- Dahlin, T., Zhou, B., 2004. A numerical comparison of 2D resistivity imaging with 10 electrode arrays. *Geophys. Prospect.* 52, 379-398.
- Dietrich, S., Weinzettel, P.A., Varni, M., 2014. Infiltration and drainage analysis in a heterogeneous soil by electrical resistivity tomography. *Soil Sci. Soc. Am. J.* 78, 1153-1167.
- Dimova, N.T., Swarzenski, P.W., Dulaiova, H., Glenn, C.R., 2012. Utilizing multichannel electrical resistivity methods to examine the dynamics of the fresh water-seawater interface in two Hawaiian groundwater systems. *J. Geophys. Res.* 117, C02012.
- Dunne, T., Zhang, W., Aubry, B. F., 1991. Effects of rainfall, vegetation, and microtopography on infiltration and runoff. *Water Resour. Res.* 27, 2271-2285.
- Guerin, R., Munoz, M.L., Aran, C., Laperrelle, C., Hidra, M., Drouart, E., Grellier, S., 2004. Leachate recirculation: moisture content assessment by means of a geophysical technique. *Waste Manage.* 24, 785–794.
- Haarder, E.B., Looms, M.C., Jensen, K.H., Nielsen, L., 2011. Visualizing unsaturated flow phenomena using high-resolution ground penetrating radar. *Vadose Zone J.*, 10, 84-97.
- Hawkins, R.H., 1982. Interpretations of source area variability in rainfall-runoff relations, in: Singh V.P., (Ed), *Rainfall-runoff relationships*. Water Resources Publications, Littleton, CO, pp. 303-324.
- Hester, E.T., Greer, B.M., Burbey, T.J., Zipper, C.E., 2015. Using electrical resistivity imaging to understand surface coal mine hydrogeology. American Geophysical Union, Fall Meeting 2015,
- Jackson, D.D., 1979. The use of a priori data to resolve non-uniqueness in linear inversion. *Geophys. J.R. Astrom. Soc.*, 57, 137-157.
- Jolly, J., Barker, R., Beaven, R.P., Herbert, A.W., 2007. Time-lapse electrical imaging to study fluid movement within a landfill. In: Eleventh International Waste Management and landfill Symposium, Calgliari, Italy.

- Loke M.H., Barker, R.D., 1996. Rapid least-squares inversion of apparent resistivity pseudosections by a quasi-Newton method. *Geophys. Prospect.*, 44, 131-152.
- Loke, M.H. 2001. Electrical imaging surveys for environmental and engineering studies: a practical guide to 2-D and 3-D surveys. p. 62. Available at [www.geoelectrical.com](http://www.geoelectrical.com).
- Nearing, M.A., Wei, H., Stone, J.J., Pierson, F.B., Spaeth, K.E., Weltz, M.A., Flanagan, D.C., Hernandez, M., 2011. A rangeland hydrology and erosion model. *Trans. ASABE (Am. Soc. Agric. Bio. Eng.)* 54, 901-908.
- Nyquist, J.E., Freyer, P.A., Toran, L., 2008. Stream bottom resistivity tomography to map ground water discharge. *Ground Water*. 46, 561-569.
- Rawls, W.J., Brakensiek, D.L., Miller, N., 1983. Green-Ampt infiltration parameters from soils data. *J. Hydraul. Eng.* 109, 62-70.
- Stone, J.J., Paige, G.B., 2003. Variable rainfall intensity rainfall simulator experiments on semi-arid rangelands, in: Renard, K.G., McElroy, S., Gburek, W., Canfield, E., Scott, R.L., (Eds.), *Proceedings of the 1<sup>st</sup> Interagency Conference on Research in the Watersheds*. USDA Agricultural Research Service, Washington, D.C, pp 83-88.
- Travelletti, J., Saihac, P., Malet, J.P., Grandjean, G., Ponton, J., 2012. Hydrological response of weathered clay-shale slopes: water infiltration monitoring with time-lapse electrical resistivity tomography. *Hydrol. Process.*, 26, 2106-2119.
- Ward, W.O.C., Wilkinson, B., Chambers, J.E., Oxby, L.S., Bai, L., 2014. Distribution-based fuzzy clustering of electrical resistivity tomography images for interface detection. *Geophys. J. Int.*, 197, 310-321.
- Weiler, M., Flühler, H., 2004. Inferring flow types from dye patterns in macroporous soils. *Geoderma*, 120, 137-153.
- Zhdanov, M.S., 1993. Tutorial: Regularization in inversion theory. CWP-136. Colorado School of Mines, 47 pp.

## Appendix A: Instrument Calibrations

A trapezoidal flume was built to route and measure surface runoff during the rainfall simulator experiments (Figure A.1). A staff gauge connected to a potentiometer was driven by an Arduino Uno to measure the depth of water in the flume at any given time. Calibration curves were developed to convert the depth of water to volumetric outflow (discharge).



**Figure A.1:** A picture of the flume used during simulator experiments.

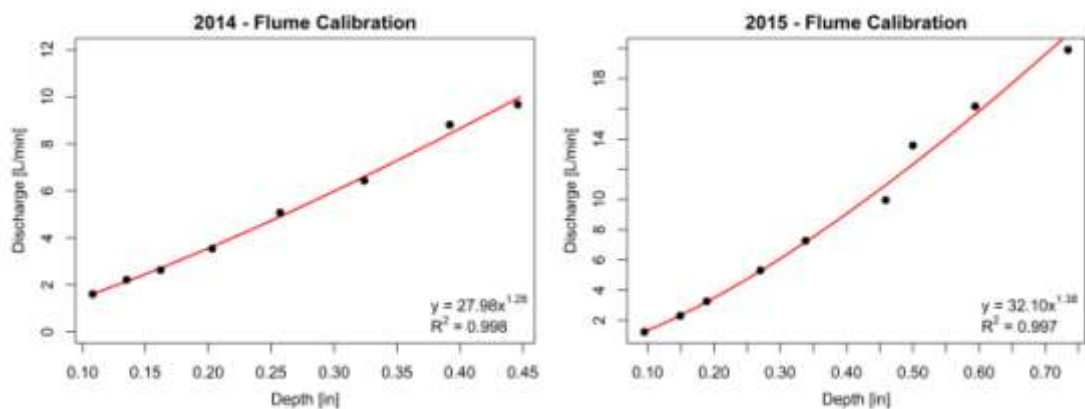


**Figure A.2:** Calibration curves created for the trapezoidal flumes. Two Separate calibrations were performed for the 2014 and 2015 field season.  $R^2$  values were 0.99 for both years indicating that that the relationship between depth and discharge is well approximated by a power function.

In addition to calibrating the flume, the WGRS was calibrated prior to each field season. A level, 2 x 6.1 m plot was used and 15 Tru-Chek rain gauges were evenly distributed across and down the length of the plot. Gauges were arranged in three rows, every 1.53 m down the length of the plot between the four simulator nozzles. The simulator setup (i.e. height, outflow pressure, etc) was identical to the setup discussed in Chapter 1. A minimum of three runs in which the target rainfall intensity was applied for a duration of 15 minutes were used to calibrate five different rainfall intensities. Basic statistics were computed for the set of runs to determine the average and the variability for each calibrated intensity (Table A.1). In general, target intensities were very similar between the two years, with 2015 exhibiting less variability between calibration runs and less spatial variability in applied rainfall.

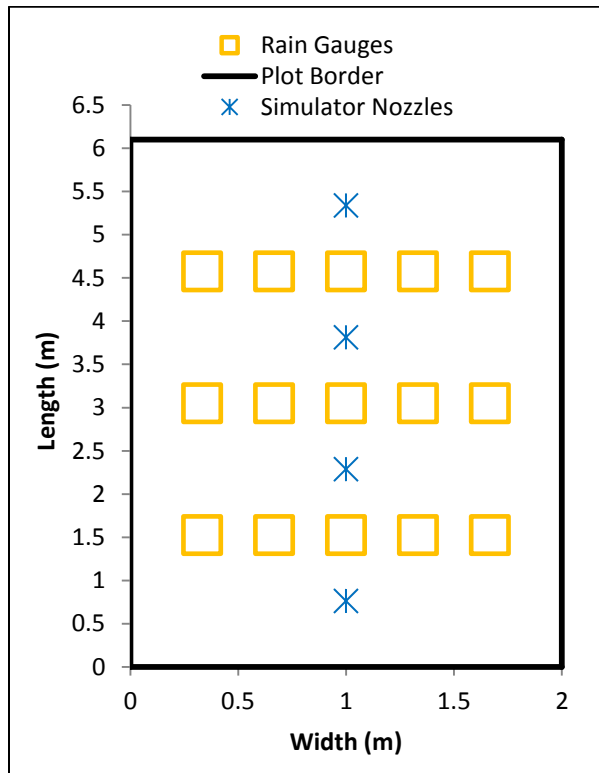


**Figure A.3: Diagram of the plot setup used for simulator calibration.**

**Table A.1: WGRS calibration results. Averages across all runs are shown with the associated standard deviation (Stdev) and coefficient of variation (CV). The Christiansen coefficient of uniformity (CU; Christiansen, 1942) is also shown as a measure of the degree of spatial variability in applied rainfall.**

Intensity ID	Year	Applied Rainfall Intensity			
		Average [mm hr <sup>-1</sup> ]	Stdev [mm hr <sup>-1</sup> ]	CV [%]	CU [%]
Intensity 1	2014	49	5.60	11.33	91.02
Intensity 2		77	8.76	11.43	91.21
Intensity 3		112	13.06	11.62	90.83
Intensity 4		157	17.69	11.25	90.67
Intensity 5		180	22.38	12.43	90.08
Intensity 1	2015	53	3.21	6.11	95.00
Intensity 2		81	5.30	6.55	95.27
Intensity 3		115	7.17	6.22	94.58
Intensity 4		153	10.45	6.82	94.88
Intensity 5		181	12.80	7.09	95.18

## Appendix B: Additional Resistivity Information

Figure B.1 shows the location of the 20 rainfall simulation plots, their associated resistivity lines for time-lapse ERT and the site geophysical lines. Background resistivity tomograms taken prior to the application of any rainfall are shown in Figures B.2 - B.6. Each site has its own resistivity scale to highlight certain resistivity contrasts. These high-resolution tomograms provide additional information about the subsurface structure for each ES.

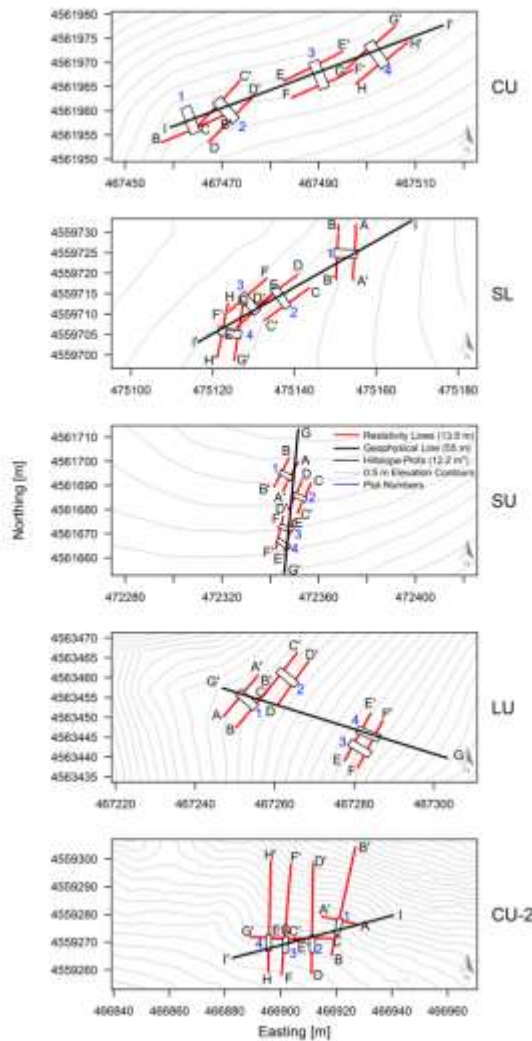


**Figure B.1: Location of the resistivity and geophysical lines for the five study sites. Location of hillslope plots are also shown.**

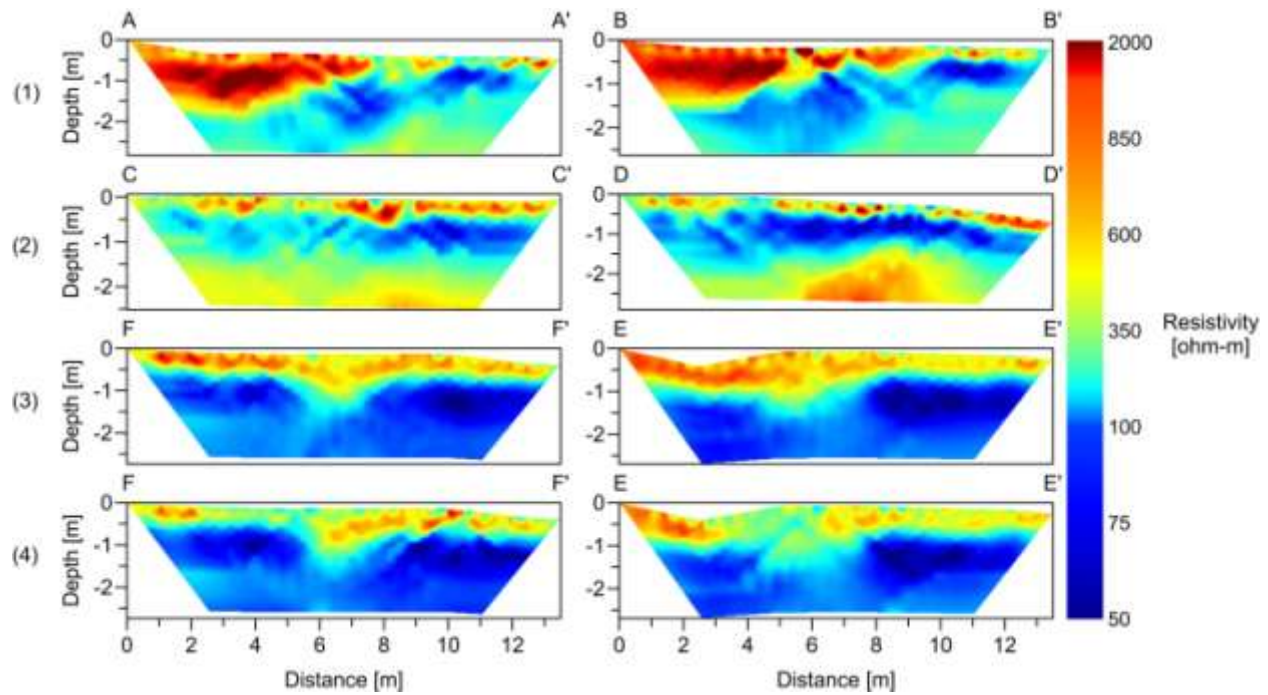


**Figure B.2: Background resistivity tomograms for the Loamy Upland ES.** Letters at the top of the profiles and numbers on the left correspond to letters and plot numbers in Figure B.1.

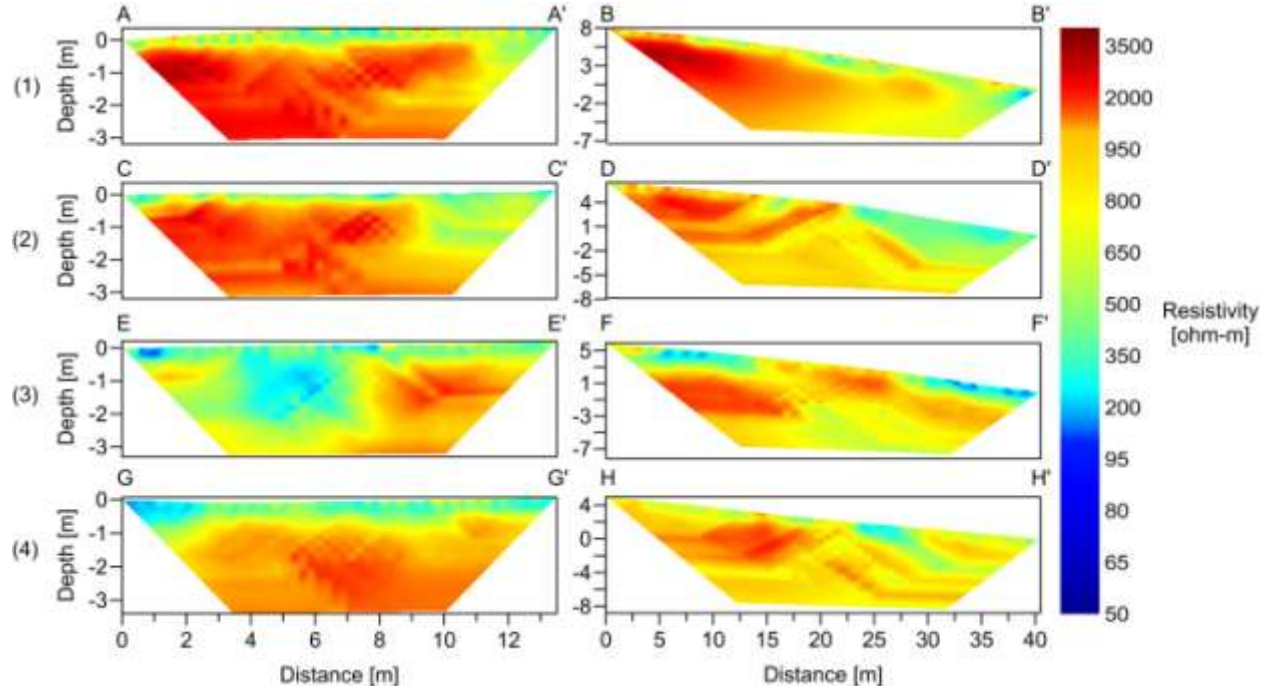


**Figure B.3: Background resistivity tomograms for the Coarse Upland-2 ES.** Letters at the top of the profiles and numbers on the left correspond to letters and plot numbers in Figure B.1.

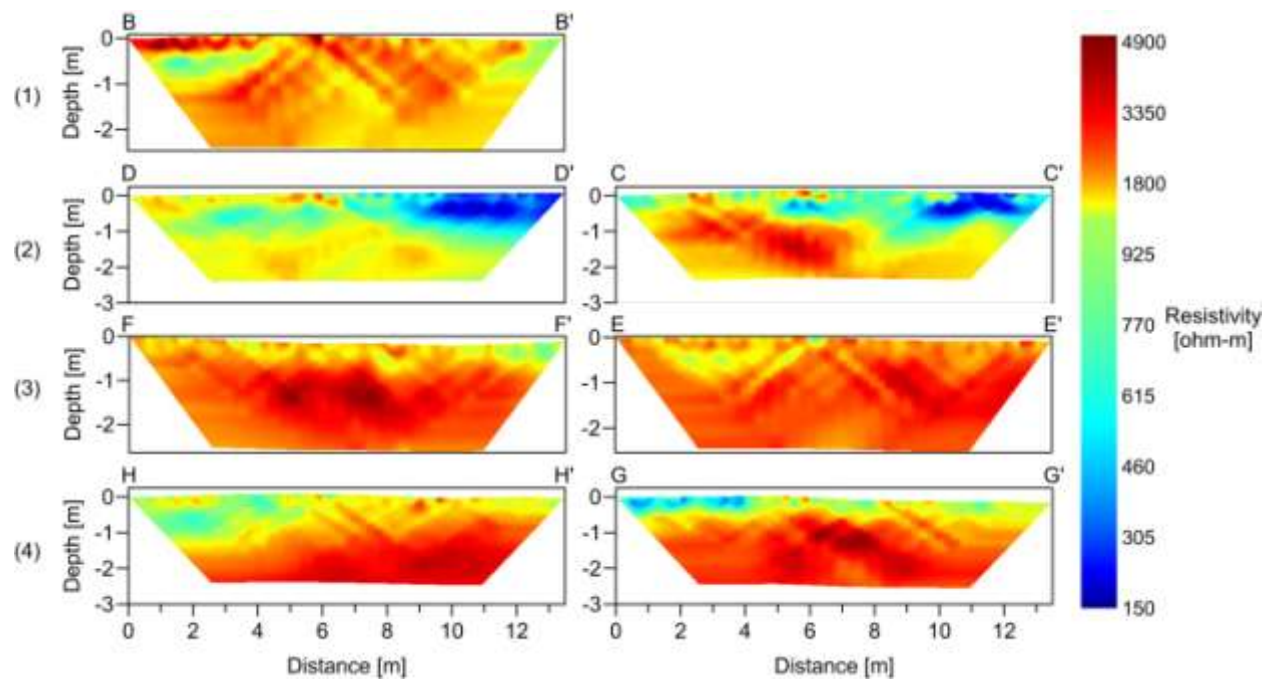


**Figure B.4: Background resistivity tomograms for the Coarse Upland ES.** Letters at the top of the profiles and numbers on the left correspond to letters and plot numbers in Figure B.1. Only one resistivity line was used for plot 1.

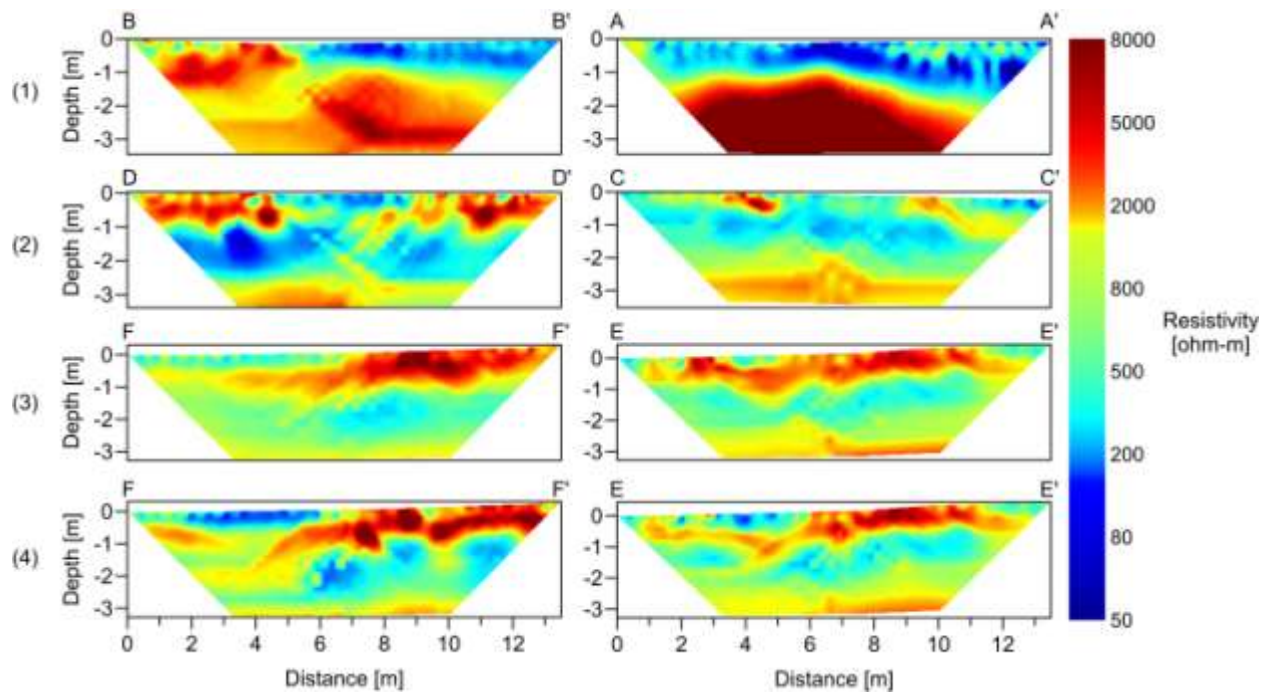


**Figure B.5:** Background resistivity tomograms for the Shallow Upland ES. Letters at the top of the profiles and numbers on the left correspond to letters and plot numbers in Figure B.1.

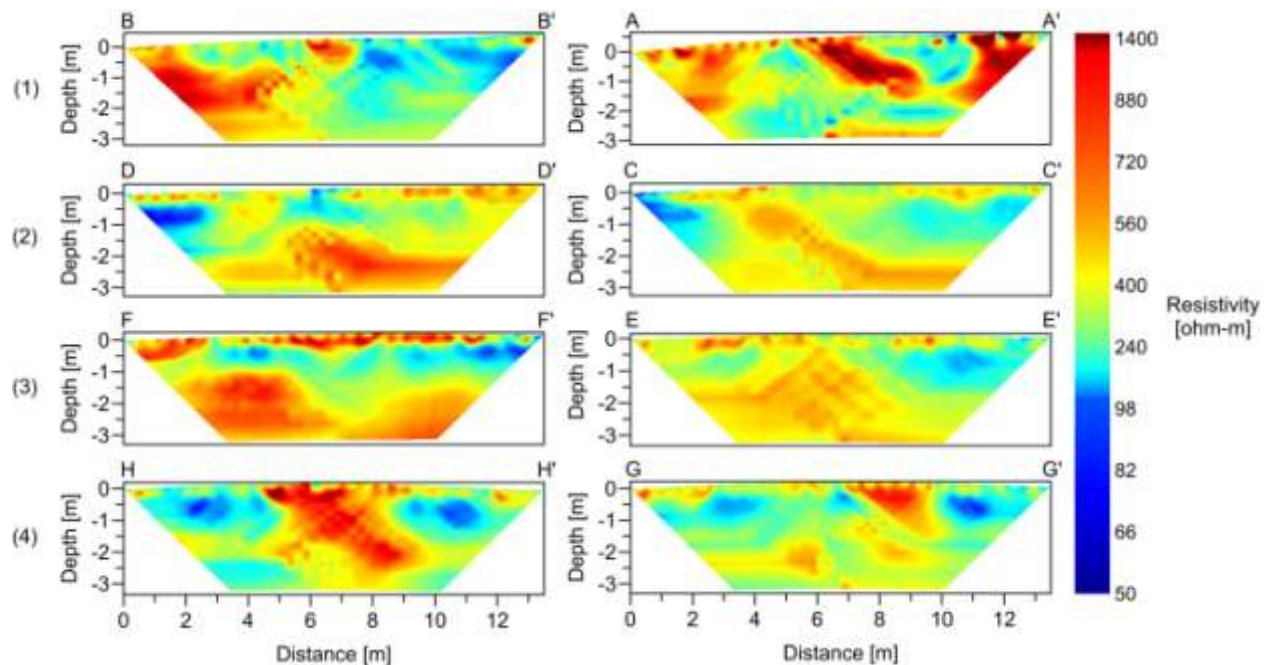


**Figure B.6:** Background resistivity tomograms for the Shallow Loamy ES. Letters at the top of the profiles and numbers on the left correspond to letters and plot numbers in Figure B.1

**Table B.1: RMS and L2 statistics for the inversions of the background tomograms. Percentage of collected data used in the inversion is also indicated.**

Site	Plot	Line ID	RMS (%)	L2	Data Used (%)
LU	1	A - A'	2.58	0.74	96.5
	1	B - B'	2.96	0.97	95.2
	2	C - C'	2.58	0.91	90.5
	2	D - D'	2.79	0.86	98.2
	3	E - E'	2.00	0.44	97.0
	3	F - F'	1.91	0.40	100.0
	4	E - E'	2.20	0.54	92.2
	4	F - F'	2.34	0.61	98.7
SL	1	B - B'	2.87	0.91	100.0
	1	A - A'	2.93	0.95	93.8
	2	D - D'	2.06	0.47	96.4
	2	C - C'	2.23	0.56	97.7
	3	F - F'	3.15	1.10	88.5
	3	E - E'	2.06	0.47	96.9
	4	H - H'	2.44	0.66	99.0
	4	G - G'	2.33	0.60	93.6
CU-2	1	A - A'	2.65	0.78	100.0
	1	B - B'	2.32	0.60	95.3
	2	C - C'	2.45	0.67	97.7
	2	D - D'	2.68	0.80	99.0
	3	E - E'	2.16	0.52	98.7
	3	F - F'	2.45	0.67	99.3
	4	G - G'	1.58	0.28	100.0
	4	H - H'	2.30	0.59	98.8
SU	1	A - A'	3.38	1.27	94.4
	1	B - B'	2.60	0.75	96.7
	2	C - C'	2.46	0.67	96.2
	2	D - D'	3.45	1.32	87.9
	3	E - E'	2.93	0.96	92.3
	3	F - F'	2.98	0.99	94.9
	4	E - E'	2.49	0.69	95.9
	4	F - F'	3.27	1.18	90.3
CU	1	B - B'	1.99	0.44	97.4
	2	C - C'	1.96	0.43	100.0
	2	D - D'	2.24	0.56	99.1
	3	E - E'	1.86	0.39	98.7
	3	F - F'	2.32	0.60	94.8
	4	G - G'	1.96	0.43	98.3
	4	H - H'	1.38	0.21	100.0

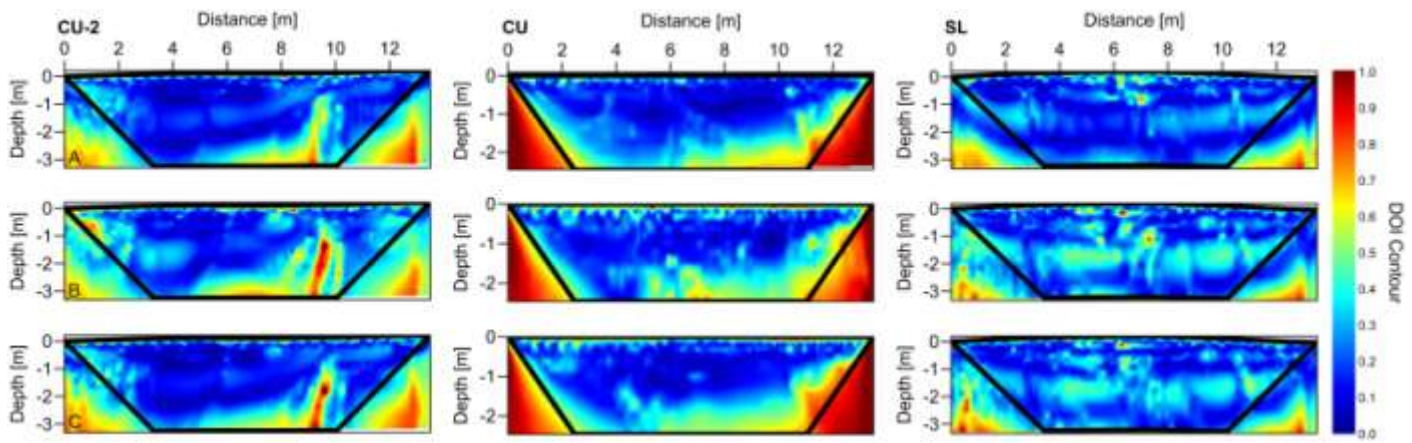


**Figure B.7:** Example DOI contour maps for the CU-2, CU and SL sites during three different stages of the rainfall simulation experiment: (A) prior to beginning of simulation, (B) during simulation and (C) post simulation. The default blanking (aspect ratio equal to 1) in the EarthImager software is indicated by the black trapezoid.